

APPLICATION OF BAYESIAN MODEL SELECTION IN
FLUORESCENCE CORRELATION SPECTROSCOPY (FCS)
TO WNT3EGFP SECRETION AND DIFFUSION IN
ZEBRAFISH EMBRYOS

SUN GUANGYU
(B.Sc. SOOCHOW UNIVERSITY)

A THESIS SUBMITTED
FOR THE DEGREE OF DOCTOR OF PHILOSOPHY
DEPARTMENT OF CHEMISTRY
NATIONAL UNIVERSITY OF SINGAPORE

2014

Declaration

I hereby declare that this thesis is my original work and it has been written by me in its entirety, under the supervision of Associate Professor Dr. Thorsten Wohland, (in the Biophysical Fluorescence Laboratory), Chemistry Department, National University of Singapore, between Aug 2010 and Aug 2014.

I have duly acknowledged all the sources of information which have been used in the thesis.

This thesis has also not been submitted for any degree in any university previously.

The content of the thesis has been partly published in:

- 1) Guo SM, He J, Monnier N, **Sun GY**, Wohland T, Bathe M: Bayesian Approach to the Analysis of Fluorescence Correlation Spectroscopy Data II: Application to Simulated and In Vitro Data. *Analytical Chemistry* 2012, 84(9):3880-3888.

SUN Guangyu



22. 8. 2014

Name

Signature

Date

Acknowledgements

I would like to express my gratitude to all those who helped me during the writing of this thesis.

My deepest gratitude goes first and foremost to my supervisor Associate Professor Dr. Thorsten Wohland for giving me the opportunity to pursue my Ph.D. in his laboratory and for his constant encouragement, great patience, valuable guidance and support in the course of this work. His passion for scientific research deeply inspired and will always inspire me.

I would like to express my heartfelt gratitude to Associate Professor Vladimir Korzh and his group member Dr. Cathleen Teh from Institute of Molecular and Cell Biology (IMCB) for providing me the chance to work on the interesting zebrafish. I have learned a great deal about zebrafish development from the numerous discussions with them. Without them this cross-disciplinary project would not have been successful.

I am also grateful to Associate Professor Mark Bathe and his group member Syuan-Ming Guo from Massachusetts Institute of Technology (MIT) for providing me the opportunity to work on the Bayesian model selection project.

My sincere thanks also go to all the past and present members of TW lab for their discussions, guidance, patience and friendship. In particular, Dr. Foo Yong Hwee and Dr. Nirmalya Bag for the guidance in FCS; Dr. Ma Xiaoxiao for the cell culture; Dr. Shi Xianke and Dr. Wang Xi for the zebrafish embryo manipulation and measurements; Dr. Jagadish Sankaran and Dr. Radek Machan for the discussion in Bayesian analysis; Dr. Anand Pratap Singh, Ms. Huang Shuangru, Ms. Angela Koh, Ms. Sibel Yavas, Mr. Andreas Karampatzakis, Ms. Ng Xue Wen, Ms. Catherine Teo Shi Hua, Mr. Fan Kaijie Herbert, Ms. Lim Shi Ying for their kind help and support.

Last but not least, I would like to thank my parents, my mother Jin Xiujuan and my father Sun Mingzhen, my brother Sun Guangzhi and his family, for their unconditional love and care.

List of Publications

Guo SM, He J, Monnier N, **Sun GY**, Wohland T, Bathe M: Bayesian Approach to the Analysis of Fluorescence Correlation Spectroscopy Data II: Application to Simulated and In Vitro Data. *Analytical Chemistry* 2012, 84(9):3880-3888.

Sun GY, Guo SM, Teh C, Korzh V, Bathe M, Wohland T: Bayesian Model Selection Applied to the Analysis of FCS Data of Fluorescent Proteins in vitro and in vivo. *Analytical Chemistry* 2015: *Under Revision*.

Teh C*, **Sun GY***, Shen HY, Korzh V, Wohland T: Secreted Wnt3 Influences Brain Patterning in Zebrafish Transgenics. *In preparation*. *Equal contribution

Eshaghi M, **Sun GY**, Jauch R, Lim CL, Chee CY, Wohland T, Chen LS: Rational Design of Monomeric and Dimeric Enhanced GFP-based Fluorescent Proteins and Molecular Probes. *In preparation*.

Table of Contents

Declaration.....	i
Acknowledgements	ii
List of Publications	iii
Table of Contents	iv
Summary.....	vii
List of Tables	ix
List of Figures.....	x
List of Symbols and Abbreviations	xii
Chapter 1 Introduction.....	1
1.1. Wnt.....	1
1.1.1. Wnt family	2
1.1.2. Wnt secretion	4
1.1.3. Wnt Traffic.....	5
1.1.4. Wnt Signaling and Function	9
1.1.5. Wnt3 in Zebrafish	11
1.2. Fluorescence Correlation Spectroscopy	13
1.2.1. Introduction of FCS	13
1.2.2. Data Fitting in FCS	17
Chapter 2 Materials and Methods.....	24
2.1. Fluorescence Correlation Spectroscopy (FCS)	24
2.1.1. Theory	24
2.1.2. Theoretical ACF models	26
2.1.3. Parameters.....	31
2.1.4. Instrument setup.....	33
2.1.5. Calibration.....	35
2.1.5.1. Samples.....	35
2.1.5.2. Background determination	36
2.1.5.3. Excitation intensity	37
2.1.5.4. Experiments	39

2.2.	Sample preparation.....	39
2.2.1.	Preparation of solution sample.....	39
2.2.2.	Preparation of cell sample.....	40
2.2.2.1.	Cell culture	40
2.2.2.2.	Plasmids.....	40
2.2.2.3.	Transfection by electroporation.....	42
2.2.3.	Preparation of zebrafish embryos	42
2.2.3.1.	Transgenic zebrafish lines	42
2.2.3.2.	DNA expression vectors	44
2.2.3.3.	Fish maintenance and embryo mounting.....	44
2.2.3.4.	Drug treatment.....	45
2.2.3.5.	Microscopy and imaging analysis	45
Chapter 3 Bayesian Approach to the Analysis of FCS Data.....		47
3.1.	Introduction	47
3.2.	Bayesian model selection	48
3.2.1.	Model probability.....	48
3.2.2.	Bayesian inference	49
3.2.3.	Bayesian model probability	50
3.2.4.	Noise estimation.....	51
3.2.4.1.	Noise estimation from multiple ACFs.....	51
3.2.4.2.	Noise estimation from a single photon-count trace	52
3.3.	Results	53
3.3.1.	Distinguishing fast photo dynamic processes	54
3.3.2.	Distinguishing the two diffusion components	57
3.4.	Conclusion.....	58
Chapter 4 Bayesian Approach to the Analysis of FCS Data of Fluorescent Proteins		59
4.1.	Introduction	59
4.2.	Results	60
4.2.1.	Organic dyes	60
4.2.1.1.	Excitation intensity	60
4.2.1.2.	Acquisition times.....	65
4.2.2.	Fluorescent proteins <i>in vitro</i>	67

4.2.2.1.	Excitation intensity	67
4.2.2.2.	Acquisition time	71
4.2.3.	Fluorescent proteins <i>in vivo</i>	72
4.2.3.1.	Excitation intensity	74
4.2.3.2.	Acquisition time	76
4.2.3.3.	Influence of temperature on data fitting	77
4.2.3.3.	Model selection for membrane measurement.....	79
4.2.3.4.	Model selection for measurements in zebrafish	83
4.3.	Discussion	85
4.3.1.	Model selection under various conditions	85
4.3.2.	Anomalous diffusion.....	88
4.3.3.	Characteristic parameters inferred from the determined models.....	89
4.4.	Conclusion.....	91
Chapter 5 Wnt3EGFP Intercellular Trafficking Study in Zebrafish Brain Development by Fluorescence Techniques		92
5.1.	Introduction	92
5.2.	Results and Discussions	93
5.2.1.	Wnt3EGFP expression in the cerebellum	93
5.2.2.	Wnt3EGFP membrane dynamics and distribution	95
5.2.3.	Wnt3EGFP extracellular and intercellular diffusion	99
5.2.3.1.	Wnt3EGFP in the brain ventricle	99
5.2.3.2.	Wnt3EGFP extracellular and intercellular mobility.....	101
5.2.4.	C59 blocks Wnt3EGFP secretion	104
5.3.	Conclusion.....	108
Chapter 6 Conclusion and Outlook.....		109
6.1.	Conclusion.....	109
6.2.	Outlook.....	111
6.2.1.	Bayesian model selection.....	111
6.2.2.	Zebrafish Wnt3EGFP.....	112
Bibliography		120
Appendices.....		133

Summary

Fluorescence Correlation Spectroscopy (FCS) is a powerful technique to address molecular dynamics with single molecule sensitivity. The introduction of fluorescent proteins has broadened their application in the life sciences. However, the FCS data fitting of fluorescent proteins remains problematic. In this study, a Bayesian model selection approach has been applied to evaluate FCS data of fluorescent proteins *in vitro* and *in vivo* to address the issues of competing fitting models. While model selection is excitation intensity dependent, we show that under fixed, low intensity excitation conditions, models can be unambiguously identified. This approach has also been extended to the model determination of EGFP labeled proteins in living zebrafish embryos.

FCS has then been employed to investigate *in vivo* EGFP tagged Wnt3 (Wnt3EGFP) secretion and diffusion patterns during zebrafish neural development. Wnt3, a member of the Wnt family, is a secreted lipid modified signaling protein. It is evolutionarily conserved in vertebrates and plays important roles in animal development and disease. The zebrafish Wnt3, like that in mice, chickens and humans, is expressed in developing neural tissues. This protein was shown to activate the canonical Wnt pathway and has been implicated in cell fate determination and proliferation. To understand Wnt3 signaling in more detail, it is necessary to study its behavior in cellular compartments as well as the intercellular space. It has been found that Wnt3EGFP is on the plasma membrane and inside cells. Moreover, it can be secreted and transported to the brain ventricle. The results indicate that small amounts of secreted Wnt3EGFP freely diffuse from the producing cells and may traverse a significant distance in intercellular space before reaching its target cells. Its mobility

under various cellular environments has been determined. Its distribution on the membrane remains relatively constant independent of developmental stages, brain regions and level of expression, indicating that the plasma membrane may act as a first checkpoint for Wnt3EGFP release. When its secretion is blocked by a Porcupine inhibitor, Wnt3EGFP is accumulated in the cell and its membrane mobility increases.

List of Tables

Table 2.1 List of laser wavelength, filters and calibration dyes	36
Table 2.2 Typical values of fitting parameters for calibration using Atto488.....	36
Table 2.3a Background measurement at different laser power in 1x PBS	37
Table 2.3b Background measurement at different laser power in cells.....	37
Table 2.4 Laser power - excitation intensity.....	38
Table 2.5 Pinhole set - ω_0	38
Table 2.6 Experimental conditions	39
Table 4.1 Parameters inferred for PMT-EGFP on the membrane and in the cytoplasm	82
Table 4.2 Parameters inferred from anomalous diffusion fitting.....	89
Table 4.3 Characteristic parameters inferred from the determined models of organic dyes and fluorescent proteins in 1x PBS.....	90
Table 4.4 Characteristic parameters inferred from the determined models of fluorescent proteins in CHO cells	90
Table 4.5 Characteristic parameters inferred from the determined models of organic dyes and fluorescent proteins in 1x PBS at 37 °C	90
Table 4.6 Characteristic parameters inferred from the determined models of fluorescent proteins in CHO cells at 37 °C.....	91
Table 5.1 Measurement on membrane for Wnt3EGFP and LynEGFP at different development stages	99
Table 5.2 Protein intracellular, intercellular and extracellular mobility	103
Table 5.3 Measurements on membrane for Wnt3EGFP and LynEGFP under 5 μ M C59 treatment.....	108
Table 6.1 Measurements on membrane for Wnt3EGFP at different treatment conditions.....	117
Table 6.2 Measurements in the brain ventricle for Wnt3EGFP at different treatment conditions.....	117

List of Figures

Figure 1.1 Wnt secretion.....	5
Figure 1.2 Wnt trafficking mechanisms.....	8
Figure 1.3 Wnt signaling pathways	10
Figure 2.1 Overview of FCS data processing	25
Figure 2.2 Characteristics of fluorescence correlation functions.....	31
Figure 2.3 FCS setup.....	35
Figure 2.4 Plasmid map of mCherry.....	41
Figure 2.5 Plasmid map of PMT-EGFP.....	41
Figure 2.6 4kb <i>wnt3</i> promoter drives EGFP reporter expression in a manner similar to endogenous <i>wnt3</i> mRNA transcript	43
Figure 3.1 Blocking transformation and fitting to evaluated models	56
Figure 3.2 Bayesian analysis of Fluorescein with varying excitation intensity.....	57
Figure 3.3 Bayesian analysis of mixtures of Atto565 and Atto565-streptavidin with distinct concentration ratios	58
Figure 4.1 ACFs calculated from PAT traces of organic dyes and their brightness....	62
Figure 4.2 Model probabilities and model selection of organic dyes at different excitation intensities.....	63
Figure 4.3 Fitting parameters inferred from different fitting models using Atto488...	64
Figure 4.4 Model probabilities and model selection and of organic dyes with different acquisition times	66
Figure 4.5 ACFs calculated from PAT traces of fluorescent proteins and their brightness	67
Figure 4.6 Model probabilities and model selection of fluorescent proteins at different excitation intensities.....	69
Figure 4.7 Fitting parameters inferred from different fitting models using EGFP	71
Figure 4.8 Model probabilities and model selection and of fluorescent proteins with different acquisition times.....	72
Figure 4.9 ACFs calculated from PAT traces of fluorescent proteins and their brightness in CHO cytoplasm	74
Figure 4.10 Model probabilities and model selection of fluorescent proteins in CHO cytoplasm at different excitation intensities	75
Figure 4.11 Fitting parameters inferred from different fitting models using EGFP measured in CHO cytoplasm	76
Figure 4.12 Model probabilities and model selection and of fluorescent proteins in CHO cytoplasm with different acquisition times.....	77
Figure 4.13 Model probabilities and model selection at 37 °C	78
Figure 4.14 PMT-EGFP in CHO cells and its model probabilities	80
Figure 4.15 Inferred fitting parameters of PMT-EGFP on CHO membrane with different excitation intensities and pinhole sizes	81

Figure 4.16 Over-expression of PMT-EGFP in CHO cytoplasm	82
Figure 4.17 Confocal images of zebrafish brain expressing EGFP label proteins	84
Figure 4.18 Model probabilities of EGFP labeled proteins measured in zebrafish embryos.....	85
Figure 4.19 Fitting parameters inferred for measurement with different acquisition times under low excitation intensity	87
Figure 5.1 Wnt3EGFP and EGFP ^{F1} expressions in the cerebellum.....	95
Figure 5.2 Wnt3EGFP and LynEGFP membrane dynamics in the cerebellum investigated by FCS	98
Figure 5.3 Secretion of Wnt3EGFP, LynEGFP and secEGFP to the brain ventricle	101
Figure 5.4 Wnt3EGFP extracellular and intercellular dynamics	103
Figure 5.5 C59 treatment on Wnt3EGFP and LynEGFP.....	105
Figure 5.6 C59 treatment influences Wnt3EGFP but not LynEGFP.....	107
Figure 6.1 Dose dependent response of Wnt inhibitors.....	115
Figure 6.2 Effect of different doses of C59 and IWR1 on Wnt3EGFP secretion, membrane mobility and fraction.....	116

List of Symbols and Abbreviations

α	anomaly factor
β	Background
β	Model parameters
η	Brightness
p	Probability
σ	Standard deviation
τ	Lag time
τ_D	Diffusion time
τ_{trip}	Triplet state relaxation time
ω_0	Lateral distance from the center of the laser focus to where the intensity has decay to $1/e^2$
ω_z	Axial distance from the center of the laser focus to where the intensity has decay to $1/e^2$
χ^2	Chi square, used to describe goodness-of-fit
ACF	Autocorrelation function
APD	Avalanche photodiode
BV	Brain ventricle
C	Concentration
C	Covariance matrix
C59	Wnt-C59
CCF	Cross-correlation function
ce	Cerebellum
<i>cps</i>	Counts per particle per second or η

CHO	Chinese hamster ovary
D	Diffusion coefficient
DM	Dorsal midline
EGFP	Enhanced green fluorescence protein
EI	Excitation intensity
EYFP	Enhanced yellow fluorescence protein
FCCS	Fluorescence cross-correlation spectroscopy
FCS	Fluorescence correlation spectroscopy
FP	Fluorescent proteins
FRET	Fluorescence resonance energy transfer
FRAP	Fluorescence recovery after photobleaching
F_{trip}	Fraction of the particles that have entered the triplet state
Fz	Frizzled
$G(0)$	Amplitude of the correlation function
$G(\tau)$	Correlation function
G_{∞}	Convergence value of $G(\tau)$ for infinite time
GPI	Glycosylphosphatidylinositol
hpf	Hours post fertilization
HSPG	Heparan Sulfate Proteoglycan
IWR	Inhibitor of Wnt response
K	Geometric ratio of axial to radial distance of the observation volume, where $K = \omega_z/\omega_0$
LP	Laser power
M	Molecular mass
MHB	Midbrain hindbrain boundary
MLE	Maximum likelihood estimation

LS	Lateral side
N	Number of particles
N_{app}	Apparent number of particles
NA	Numerical aperture
N_A	Avogadro constant
$P(A)$	Probability that event A happens or is true
PAT	Photon arrival times
PBS	Phosphate buffer solution
PMT	Plasma membrane targeting
Porc	Porcupine
PSF	Point spread function
PTU	0.003% 1-phenyl-2-thiourea in 10% Hank's saline
S	Sample covariance matrix
SD	Standard deviation
SEM	Standard error of the mean
SPIM	Single-plane illumination microscopy
t_b	Block time
Wls/Evi	Wntless
WT	Wild type
V_{eff}	Effective volume

Chapter 1

Introduction

1.1. Wnt

Wnt proteins belong to a family of secreted cysteine-rich proteins that are evolutionarily conserved in the metazoan. Wnt signaling controls multiple events during development and adult life of all animals. As a family member of Wnt genes, Wnt3 is known to play an essential role in tissue patterning in human. Loss of function mutations in human lead to tetra-amelia in affected fetuses characterized by craniofacial malformations, defective nervous systems and limbs (Niemann, Zhao et al. 2004). The *wnt3* gene is characterized at the mRNA level in zebrafish. Whole mount in situ hybridization detects Wnt3 expression in the developing neural tube and misexpression studies suggests that Wnt3 activates the downstream signaling pathway (Clements, Ong et al. 2009). Recently, more attention is given to the transport process during Wnt signaling. However controversial results were obtained because most research incorporates immuno-staining or non-quantitative image analysis approaches in their assessment of Wnt transport. Moreover, most studies used *Drosophila* wing disc as the model, little was known in vertebrates. It is necessary to take a close look at Wnt signaling in vertebrates with better resolution. Therefore, to understand zebrafish Wnt3 signaling and function in more detail, it is important to study its behavior in endogenous cellular compartments and intercellular space by using high resolution fluorescent techniques. This section will provide a brief overview of Wnt

proteins structure, function, trafficking models as well as signaling processes with an emphasis on recent Wnt3 study in zebrafish.

1.1.1. Wnt family

Proteins in the Wnt family are secreted, cysteine-rich signaling molecules. They are evolutionarily conserved among vertebrates and invertebrates and are of great significance in animal development and disease. Members of the Wnt family are known to regulate different processes in development, such as tissue patterning, cell proliferation and differentiation, and maintenance of stem cell pluripotency (Logan and Nusse 2004; Reya and Clevers 2005). It has been over thirty years since the discovery of the first family member Wnt1, which is previously known as Int1 (Nusse and Varmus 1982). So far, 19 *wnt* genes have been identified in the human genome (Miller 2002).

Overall, Wnt proteins are about 40 kDa, with a high number of conserved cysteines, which are likely to be responsible for the disulphide bonds and proper folding. In 2003, the Nusse laboratory first successfully purified active mouse Wnt3a, and proved the lipid modification of Wnt proteins (Willert, Brown et al. 2003). One of the modifications for mature Wnt proteins is a palmitate group attached to a conserved N-terminal cysteine, corresponding to C77 in mouse Wnt3a. This modification is also observed in *Drosophila* Wnts, including Wnt1, Wnt5a and Wingless (Wg) (Zhai, Chaturvedi et al. 2004; Galli, Barnes et al. 2007; Kurayoshi, Yamamoto et al. 2007). Another modification is the addition of palmitoleic acid to serine 209 (S209) in mouse Wnt3a (Takada, Satomi et al. 2006), which is also conserved among Wnt proteins. These post-translational lipid modifications are responsible for Wnts hydrophobicity and necessary for their secretion and signaling. However, the exact function of the

two adducts in Wnt secretion and signaling activity may be different from case to case (Franch-Marro, Wendler et al. 2008; Tang, Wu et al. 2012).

The acyltransferase Porcupine (Porc) plays an essential role for lipid modification of Wnts. First identified as a segment polarity gene in *Drosophila*, Porc is a member of membrane-bound O-acyltransferases (MBOATs) (van den Heuvel, Harryman-Samos et al. 1993; Kadowaki, Wilder et al. 1996; Hofmann 2000). It encodes a multi-pass transmembrane protein that resides in the endoplasmic reticulum (ER), where the lipid modification occurs. It has been proven to be essential for the *Drosophila* Wnts function and transportation (Herr and Basler 2012). This Porc gene family is also evolutionarily conserved in mouse and *Xenopus* and is shown to be involved in processing various Wnts (Tanaka, Okabayashi et al. 2000). In the absence of Porc, Wnts accumulate in the ER in *Drosophila* S2 cells and the purified Wnt are less hydrophobic as examined by the standard hydrophobic chromatography techniques (Zhai, Chaturvedi et al. 2004). It has been shown that Porc is required for S209 acylation for mouse Wnt3a and its transportation from the ER to the membrane (Takada, Satomi et al. 2006). Similarly, in chick neural tube, Porc is required for Wnt1 and Wnt3a palmitoylation and regulates their activity (Galli, Barnes et al. 2007). Porc is a highly conserved component of the Wnt pathway and is active only in the Wnt producing cells (Clevers and Nusse 2012).

Besides these lipid modifications, Wnt proteins also undergo glycosylation, which is the attachment of N-linked oligosaccharide chains (Komekado, Yamamoto et al. 2007). However, the role of this translational modification varies for different Wnt proteins. It is shown that it has no major defects on *Drosophila* Wg secretion or signaling (Tang, Wu et al. 2012), but it is necessary for mouse Wnt3a palmitoylation

(Komekado, Yamamoto et al. 2007). The function of Wnt glycosylation needs to be revealed.

1.1.2. Wnt secretion

The Wnt secretion is shown in Fig. 1.1. Briefly, after modifications in the ER, Wnt proteins are transported to the Golgi, where they bind to their transporter, Wntless (Wls/Evi). Then the complex Wls-Wnt is transported to the plasma membrane. Wls is then recycled through clathrin-mediated endocytosis (Belenkaya, Wu et al. 2008; Pan, Baum et al. 2008; Yang, Lorenowicz et al. 2008) and retrieved by the retromer complex (Coudreuse, Roel et al. 2006; Prasad and Clark 2006; Franch-Marro, Wendler et al. 2008). Wls was identified in 2006 as a multipass transmembrane protein and is required for Wnt secretion by regulating its exocytosis (Banziger, Soldini et al. 2006; Bartscherer, Pelte et al. 2006; Goodman, Thombre et al. 2006). Wls is evolutionarily conserved among various vertebrates and invertebrates and specific for Wnt secretion. The only exception is *Drosophila* WntD, since it is not palmitoylated and thus is secreted in an alternative manner (Ching, Hang et al. 2008). After being transported to the membrane, Wnt proteins stick to cell membranes and the extracellular matrix and function either as short-range signaling molecules, performing cell-to-cell communication (Clevers 2006), or as long-range morphogens, in which case, providing positional information to cells by their concentration gradient (Zecca, Basler et al. 1996; Neumann and Cohen 1997).

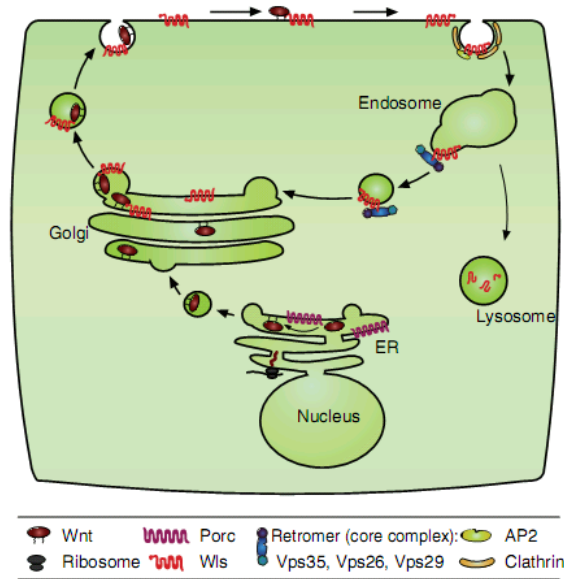


Figure 1.1 Wnt secretion (Port and Basler 2010)

1.1.3. Wnt Traffic

Due to their posttranslational lipid modifications, these membrane attached Wnt proteins need special mechanisms to signal to direct neighbors or perform medium- to long-range paracrine signaling. Several mechanisms have been proposed to achieve this (Yan and Lin 2009; Port and Basler 2010).

First, the Wnts can be carried and transported by a higher-order complex, such as taken by lipoproteins or exosomes (Fig. 1.2A and B). A lipoprotein particle is an assembly that contains a central core of neutral lipids and an outer phospholipid monolayer. Vertebrate lipoprotein particles are scaffolded by apolipoproteins, whereas insects have similar particles named lipophorins (Arrese, Canavoso et al. 2001; van der Horst, van Hoof et al. 2002). Wg has been reported to colocalize with lipophorin in Wg receiving cells in *Drosophila* wing disc. Reducing the lipophorin amount shortens the signaling range. (Pan ákov á Sprong et al. 2005). Wnt3a has been found associated with lipoproteins secreted from cultured mammalian cells, and the mutant with the absence of the palmitate moiety could be secreted in a lipoprotein-

independent way (Neumann, Coudreuse et al. 2009). Recently, the secreted Wg-interaction molecule (Swim), a member of the Lipocalin family, has been identified to bind to Wg to maintain its mobility and signaling (Mulligan, Fuerer et al. 2012). Besides the lipoproteins, exosomes can also carry Wnts. Exosomes are vesicles with a diameter of 40 - 100 nm. They are secreted by different kinds of cells under physiological and pathological conditions. Exosomes could regulate cell-to-cell communication by transporting proteins to target cells, delivering genetic materials and disposing unwanted proteins (Simons and Raposo 2009; Schneider and Simons 2013). It has been reported that Wnts are transported by exosomes to the signaling receiving cells and secreted on exosomes in human cells (Gross, Chaudhary et al. 2012).

Second, Wnt proteins can be transported by the proteins in the extracellular matrix, such as Heparan Sulfate Proteoglycans (HSPGs) and receptor proteins (Fig. 1.2C and D). HSPGs are composed of a protein core with heparan sulfate glycosaminoglycan chains attached. They locate at the cell surface by a glycosylphosphatidylinositol (GPI) linker and in the extracellular matrix. They are known to play an important role in the transportation and function of various signaling proteins (Yan and Lin 2009). In *Drosophila*, the glypicans Dally (division abnormally delayed) and Dlp (Dally-like proteins) are reported to maintain extracellular Wg and participate in establishing Wg gradient formation in a restricted diffusion mechanism (Baeg, Selva et al. 2004; Han, Yan et al. 2005). Moreover, HSPGs could also function as a co-receptor to regulate the Wnt receiving level on the cell surface (Yan, Wu et al. 2009). Besides HSPGs, Wnt related secreted receptors in the extracellular matrix are also able to transport the proteins. In the *Xenopus* embryo, the over-expressed secreted Frizzled-related proteins (sFRPs) are shown to enhance Wnt8 and Wnt11 diffusion by extracellular

interactions and thus expand the signaling range (Mii and Taira 2009). In the mouse optic cup, the disruption of Wnt11 expression and Wnt/ β -catenin signaling activation is observed by sFRPs genetic inactivation (Esteve, Sandonis et al. 2011).

Third, the signaling molecules can also be transported by planar transcytosis (Fig. 1.2E), in which secreted molecules are actively transported through repeated rounds of endocytosis and re-secretion in receiving cells (Bejsovec and Wieschaus 1995). Later, it has been pointed out that the endocytosis happens for both in the Wg producing cells and in the secretion pathway and HSPGs are required in this process (Pfeiffer, Ricardo et al. 2002). The endocytosed Wg can also be recycled to the plasma membrane. It has also been found out that the internalization routes differ for Wg on the apical and basal side of the *Drosophila* wing disc and that HSPGs and Frizzled receptors function differently in this process (Marois, Mahmoud et al. 2006; Rives, Rochlin et al. 2006).

Last, they can be transported by cytonemes grown from signal producing cells to signal receiving cells (Fig. 1.2F). Firstly identified in the *Drosophila* wing disc, these actin-based filopodial extensions were shown to be induced when cultured next to a source of signaling molecules and proposed to be responsible for long range molecule transportation (Ramírez-Weber and Kornberg 1999). Later, cytonemes have been demonstrated to mediate various signaling molecules transport, including fibroblast growth factor (FGF), Decapentaplegic (Dpp) and Hedgehog (Hh) in *Drosophila* (Sato and Kornberg 2002; Hsiung, Ramirez-Weber et al. 2005; Bischoff, Gradilla et al. 2013; Roy, Huang et al. 2014), sonic hedgehog (SHH) in chick embryonic limb bud (Sanders, Llagostera et al. 2013). It has been also pointed out that the response of cytonemes is with specificity to different signaling proteins (Roy, Hsiung et al. 2011).

Recently, Wnt8a is reported to be transported by cytonemes in both live zebrafish embryos and cultured mammalian cells (Stanganello, Hagemann et al. 2015).

Besides these mechanisms, there are other possibilities for Wnt transportation, which have been shown to work for other signaling proteins but have not been tested on Wnt proteins. One of them is forming soluble micelles to shield the lipid part, similar to another lipid modified signaling protein Hedgehog (Goetz, Singh et al. 2006; Vyas, Goswami et al. 2008). It has been pointed out that Palmitoylation is essential for the generation of soluble micelles in vertebrates (Chen, Li et al. 2004). So far, the experimental evidence supports several mechanisms for Wnt transportation. But it is likely that the pathway depends on the tissue type and the developmental stage.

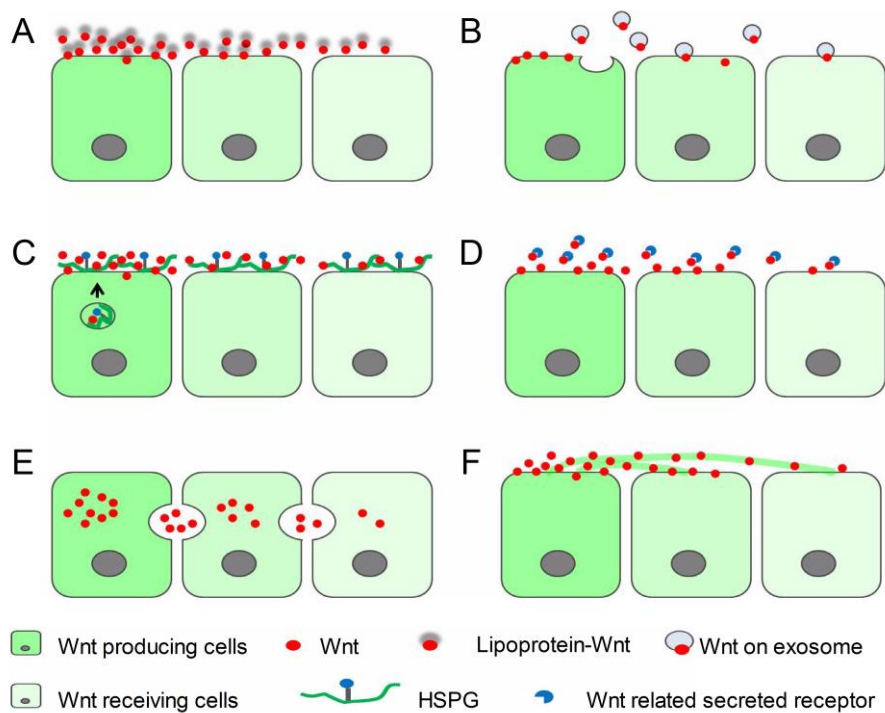


Figure 1.2 Wnt trafficking mechanisms

(A) Wnt proteins bound to lipoproteins; (B) Wnt proteins on the exosome; (C) Lateral diffusion aided by HSPG; (D) Transported by Wnt related secreted receptors; (E) Planar transcytosis; (F) Cytonemes. This figure was drafted based on Figure 1 in Yan and Lin 2009.

Although a lot of effort is being spent on this subject, an efficient and effective method to reveal the transportation in the prospective of dynamics has yet to be explored. Moreover, the studies of Wnt protein trafficking mechanisms have used either cell lines or *Drosophila* wing disc as a model and not much is known of them in vertebrates. Furthermore, due to the technical limitations, most of the research is based on immunostaining or non-quantitative imaging analysis, which leads to controversial results. Even though a novel staining method has been introduced to visualize the extracellular proteins and is widely used to discover the transportation mechanisms (Strigini and Cohen 2000), the molecular transportation dynamics still cannot be revealed by such methodology. Therefore, it is necessary to employ high spatial and temporal resolution fluorescent techniques to investigate zebrafish Wnt trafficking in the prospective of *in vivo* dynamics.

1.1.4. Wnt Signaling and Function

To trigger the intracellular signal transduction, Wnt proteins interact with multiple receptors. One of them is the seven-pass transmembrane protein Frizzled (Fz, Bhanot, Brink et al. 1996). Proteins of the Fz family bind to various Wnts through the cysteine residues domain (CRD) with high affinity (Hsieh, Rattner et al. 1999; Wu and Nusse 2002). Several co-receptors have also been identified including the low-density lipoprotein (LDL) receptor-related protein LRP-5/6 or Arrow family, and the tyrosine kinase receptor Ryk or Ror2 (Kestler and Kuhl 2008).

Once received by the targeting cell, Wnt proteins can trigger two types of signaling pathways: the β -catenin-dependent canonical pathway and the β -catenin-independent non-canonical pathway (Buechling and Boutros 2011). They are shown in Fig. 1.3. In the canonical pathway, Wnt proteins bind to the membrane receptor Frizzled together with LRP5/6 to regulate the β -catenin levels in the cytoplasm and nucleus. Nuclear β -

catenin regulates transcription of the Wnt target genes by interacting with transcription factors such as LEF/TCF. This kind of signaling pathway is generally related to cell proliferation, fate specification and differentiation (Logan and Nusse 2004). In the non-canonical pathway, β -catenin-mediated transcription is not involved. It includes planar cell polarity (PCP) pathways and the Wnt/ Ca^{2+} pathway and generally relates to the cell migration and organ morphogenesis. Some Wnt proteins are known to be active only the canonical signaling, such as Wnt1, 3, 3a, 8a and 8b, whereas some are known to activate mostly the non-canonical signaling, such as Wnt5a, 7a, 7b and 11 (Buechling and Boutros 2011). However, the ability for a Wnt member to activate the two pathways is not exclusive, but depends on the tissue type. It has been pointed out that the Frizzled receptor expression amount may influence the option (Mikels and Nusse 2006).

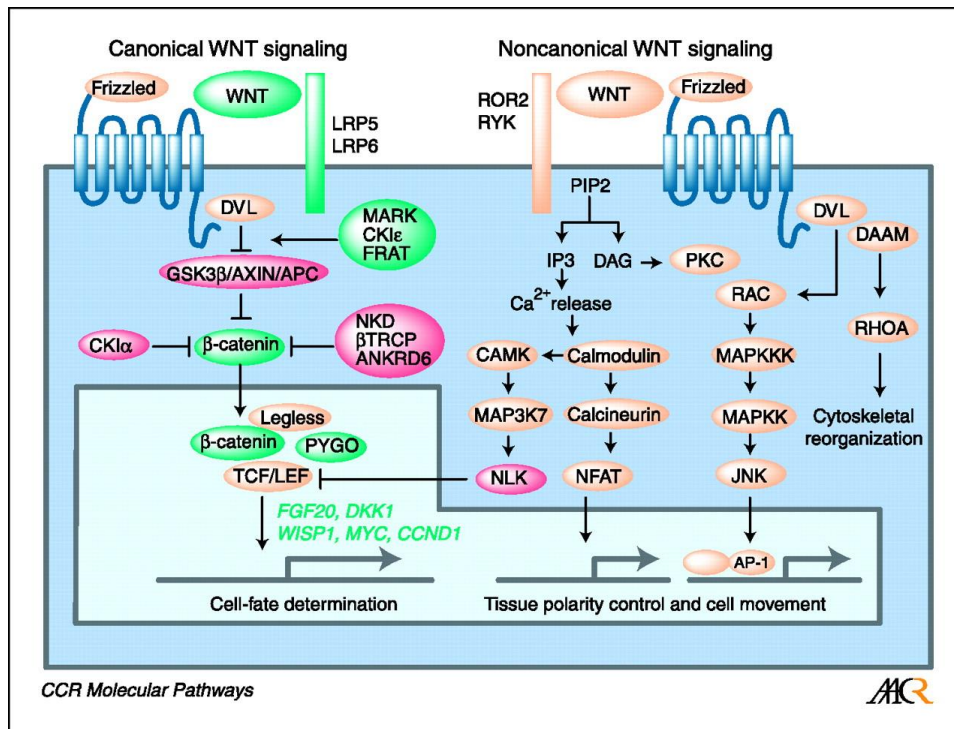


Figure 1.3 Wnt signaling pathways

On the left is the β -catenin-dependent canonical pathway and on the right is the β -catenin-independent non-canonical pathway. (Katoh 2007)

1.1.5. Wnt3 in Zebrafish

As a vertebrate model, zebrafish is evolutionarily close to humans and easy to be manipulated with standard genetic and molecular tools. Therefore, proteins of interest can be expressed in designated organs or development stages and thus makes it possible to investigate proteins functions and dynamics in living sample. A number of components of the Wnt signaling were characterized in zebrafish early on (Molven, Njølstad et al. 1991; Krauss, Korzh et al. 1992; Blader, Strähle et al. 1996). In the case of disease related study, it can further serve as a drug discovery platform (Lieschke and Currie 2007). In addition, zebrafish is easy to grow and reproduce. Their embryos are fertilized and developed externally. Moreover, zebrafish embryos and early larva are optically transparent, which makes it suitable for fluorescence based imaging techniques.

Wnt3, a member of the Wnt family, is present in bird, frog, and fish (Garriock, Warkman et al. 2007). It is of great importance in development as absence of Wnt3 in mice led to defective primary axis patterning characterized by the absence of a primitive streak, mesoderm and lack of anterior-posterior neural patterning (Liu, Wakamiya et al. 1999). In humans, a homozygous nonsense mutation (Q83X) in the Wnt3 gene was identified as the cause of a human genetic disorder Tetra-amelia (Niemann, Zhao et al. 2004). The regional expression of Wnt3 precedes the formation of neuromeres in the diencephalon in the mouse (Salinas and Salinas and Nusse 1992). Chick Wnt3 has been reported to inhibit Sonic Hedgehog response in neural patterning (Robertson, Braun et al. 2004). The role of Wnt3 post neural patterning especially in the area of neural proliferation is controversial. In non-neural cells, over-expression of Wnt3 is associated with more aggressive non-small cell lung cancer tumors in human (Nakashima, Liu et al. 2012). Wnt3 and Frizzled 7 are also commonly over-expressed

in hepatocellular carcinoma and ectopic expression of Wnt3 and Frizzled 7 in human hepatic progenitors enhanced cell proliferation, invasiveness and anchorage independence growth of transformed cells (Nambotin, Tomimaru et al. 2012). Mutations in the Wnt pathway are associated with medulloblastoma, the most common brain tumor in children. In the developing cerebellum, Wnt signaling increases the proliferation of multipotent neural stem cells and impairs their differentiation (Pei, Brun et al. 2012). However, the role of Wnt3 in neural proliferation and/or differentiation is not clear. Human Wnt3 transcripts are present in both proliferating NTERA-2 cl. D1 (NT2) cells and maintained in retinoic acid differentiated neuronal population (Katoh 2002), where NT2 human embryonic carcinoma cells are similar to early neuroepithelial progenitors. Exposure to retinoic acid induced differentiation of NT2 cells to postmitotic neurons (Coyle, Li et al. 2011). In vertebrates, Wnt3 transcripts are detected in both developing and adult mouse cerebellum. Recent evidence from *in vitro* and *ex vivo* data suggests Wnt3 inhibits proliferation of granule cell progenitors in the cerebellum thereby inhibiting medulloblastoma formation in mice (Anne, Govek et al. 2013). The zebrafish Wnt3 is also expressed in developing neural tissue and was shown to activate the canonical Wnt pathway (Clements, Ong et al. 2009). The *in vivo* role of Wnt3 in neural development in proliferation and differentiation still needs to be assessed.

In summary, Wnt proteins are lipid modified signaling proteins and are crucial in animal development and disease. Family member Wnt3 is shown to play an important role in neural development and proliferation. Although Wnt proteins have been extensively investigated, there is still no efficient way to monitor its behavior in living system. To understand its function and signaling in details, it is of great practical meaning to investigate the system in the prospective of molecular dynamics. The

well-studied and characterized model can further serve as a drug discovery platform. The method, fluorescence correlation spectroscopy (FCS), used in this study will be introduced in the following section; the related results will be presented in Chapter 5; and a conclusion will be provided in Chapter 6.

1.2. Fluorescence Correlation Spectroscopy

The development of fluorescence spectroscopy and imaging techniques makes it convenient to address questions in biology and life science (Ishikawa-Ankerhold, Ankerhold et al. 2012). Especially after the introduction of fluorescent proteins, genetic labeling of proteins has further broadened the investigation field in monitoring protein behavior *in vivo*. Advanced fluorescence techniques, such as fluorescence correlation spectroscopy (FCS), fluorescence recovery after photobleaching (FRAP) and Förster resonance energy transfer (FRET), have further led to a broader range of novel applications in biology. These techniques provide quantitative information on biomolecules and their interactions with high spatial and temporal resolution. One of them, FCS, with single-molecule sensitivity, now is commonly used to study molecular processes *in vitro* and *in vivo*.

1.2.1. Introduction of FCS

FCS was introduced about 40 years ago (Magde, Webb et al. 1972; Elson and Magde 1974). It is a method based on correlation analysis. In FCS fluorescence signal fluctuations over time as fluorophores pass through a small observation volume are transformed by a mathematical procedure known as autocorrelation to derive the parameters that describe dynamics of the underlying physical processes, such as chemical reactions, rotational diffusion, translational diffusion, flow or oligomerization. In the introductory work, Magde et al. employed FCS to determine

diffusion coefficients of pure dyes and chemical kinetics of binding between macromolecule DNA and the drug ethidium bromide (EtBr). After this, FCS was further developed both in theory and in application (Magde, Elson et al. 1974; Magde, Webb et al. 1978; Koppel 1974; Aragón and Pecora 1976; Koppel, Axelrod et al. 1976). However, due to the technical limitations, including large observation volume, intensity variations of excitation laser beam, low quantum yield fluorophores and less efficient detectors, FCS suffered from low signal-to-noise ratio in the beginning. Therefore, its applications were quite limited initially.

It was the combination with confocal illumination that improved the sensitivity of FCS and led to its widespread application (Rigler, Mets et al. 1993; Eigen and Rigler 1994). In such a scheme, a small pinhole was used in the setup to generate a small observation volume and efficiently removed out-of-focus light. This minimized the number of detected molecules and thus the intensity fluctuations caused by molecules moving in and out of the observation volume could be more easily distinguished compared to the average intensity from the molecules remaining in the volume. Therefore, the detection sensitivity was improved. With the use of higher numerical aperture objectives, an even smaller volume was achieved in the femtoliter (fL) range. Such setups provide single molecule level sensitivity and have become the standard in FCS setups nowadays. With nanosecond resolution and relatively short measurement time, FCS has been successfully employed to various kinds of study, including fluorophore blinking dynamics (Widengren, Rigler et al. 1994; Widengren, Mets et al. 1995; Widengren and Schwille 2000; Widengren and Seidel 2000), molecule conformational changes (Kral, Langner et al. 2002), binding equilibria (Daniel, Thompson et al. 2002), protein aggregation (Pitschke, Prior et al. 1998), and even some works in model membranes (Korlach, Schwille et al. 1999; Kahya, Scherfeld et

al. 2003; Burns, Frankel et al. 2005) as well as in cells (Terada, Kinjo et al. 2000; Braun, Peschke et al. 2002; Briddon, Middleton et al. 2004).

Another important aspect that further broadens the application field of FCS is the discovery and application of fluorescent proteins (Shimomura, Johnson et al. 1962; Chalfie, Tu et al. 1994; Ormo, Cubitt et al. 1996). By modern molecular tools, the protein of interest could be genetically tagged with fluorescent protein in a specific design with a defined stoichiometry. Therefore, the protein behavior can be monitored using fluorescence imaging techniques. As first demonstrated in 1994, green fluorescent protein (GFP) was used to tag mRNA localization related protein *exuperantia* (*exu*) (Wang and Hazelrigg 1994). The authors showed that the constructed GFP-Exu could function as endogenous Exu and provide details of the protein subcellular localization during *Drosophila* oogenesis. Later, a considerable amount of research was done employing this methodology in the life science (Miyawaki 2011).

On one hand, FCS has been employed to characterize the photo dynamics of these fluorescent proteins. Widengren et al. demonstrated that enhanced GFP (EGFP) has multiple photophysical and photochemical processes in a time scale from ns to ms (Widengren, Mets et al. 1999). Besides the typical triplet state of a fluorophore, two photon induced isomerization blinking processes have also been revealed and characterized. The protonation - deprotonation blinking process of EGFP has also been investigated (Haupts, Maiti et al. 1998; Widengren, Terry et al. 1999). Later, the same methodology has been employed to characterize its variations, yellow fluorescent protein (YFP) (Schwille, Kummer et al. 2000; Heikal, Hess et al. 2000) and super folder GFP (sfGFP) (Cotlet, Goodwin et al. 2006), as well as dark state issue of red fluorescent proteins (Schenk, Ivanchenko et al. 2004; Hendrix, Flors et al.

2008; Wu, Chen et al. 2009). These works have demonstrated the ability of FCS to address fast dynamic issues of fluorescent proteins.

On the other hand, taking advantage of the genetic labeling and its own single-molecule sensitivity, FCS has also served as a powerful tool for *in vivo* study (Mütze, Ohrt et al. 2011; Ries and Schwille 2012). Quantitative characterization of molecular transportation and interactions on physicochemical condition in living cells is a first step towards understanding biological processes in living animal models. Combining FCS with confocal imaging technique enables investigation of biomolecular behavior and interactions in well-defined locations in cellular systems. FCS therefore is of great help to determine local concentrations and diffusion coefficients of fluorescently labeled molecules on a molecular and subcellular level. The mobility change could be an indication of environment viscosity influence or interaction. Moreover, in the case of binding, the fraction of bound component can also be determined. Until now, FCS has been employed to analyze the dynamics of labeled molecules in the cytoplasm, nuclei and membranes in various types of cells (Ohrt, Muetze et al. 2008; Dross, Spriet et al. 2009; Ries and Schwille 2008; Machan and Hof 2010). Furthermore, works including anomalous diffusion (Wachsmuth, Waldeck et al. 2000), dynamic intracellular processes (Yao, Munson et al. 2006), protein oligomerizations (Takahashi, Okamoto et al. 2007), as well as ligand-receptor binding (Ries, Yu et al. 2009), have been reported.

Recently, more than in cells, FCS also opens up the avenue in studying proteins in living organism in various animal models with high spatial and temporal resolution. Signaling biomolecules are transported to locations where they perform functions. Their transport rate could play an important role in their signaling and function. However, this property cannot be investigated by *in vitro* experiments but only be

meaningful in a native environment. Moreover, FCS provides the opportunity to investigate intra- and intercellular communications. In 2009, Shi et al. reported applications in both *Drosophila* and zebrafish (Shi, Teo et al. 2009). In their work, diffusion coefficients of cytosolic as well as membrane located EGFP labeled proteins were determined. In particular, the blood flow velocities were also measured from autofluorescence of the serum in the dorsal aorta and cardinal vein. In addition, the measurable depth in zebrafish was determined. Later, the same group reported determination of dissociation constants using a variant of FCS (Shi, Foo et al. 2009). In another study on zebrafish reported by Yu et al. determined the mobility of EGFP labeled proteins in extracellular space when generating the morphogen gradient (Yu, Burkhardt et al. 2009). A similar approach was adopted in Abu-Arish's work to verify the high mobility of cytoplasmic morphogen Bicoid (Bcd) by FCS in syncytial *D. melanogaster* embryos (Abu-Arish, Porcher et al. 2010). Besides the animal models mentioned above, it has also been employed in *C. elegans* embryos (Petrasek, Hoegge et al. 2008) and mouse embryos (Kaur, Costa et al. 2013) to characterize protein dynamics. These studies have therefore established the possible extension of the FCS application regime to investigate protein mobility in living organism.

1.2.2. Data Fitting in FCS

In FCS, characteristic parameters to describe the process of interest are quantitatively inferred by fitting with a hypothetical model. Therefore, the data interpretation relies on the model selection. It is not an issue when dealing with known simple processes, such as organic dyes in solution. However, the case becomes more complex for unknown processes and especially for the measurements on living systems (Wachsmuth, Waldeck et al. 2000; Schwille 2001). To achieve reliable results, it is necessary to improve the data quality by increasing the signal-to-noise ratio. Koppel

pointed out that the signal-to-noise ratio depends on the photon count rate per molecule, total acquisition time as well as the correlator channel minimum width (Koppel 1974). Later, Qian et al extended Koppel's work and assumed a two-dimensional Gaussian sample profile and low concentration. Under these assumption, the signal-to-noise ratio is proportional to the square root of the number of particles (Qian and Elson 1990). Further, analysis considering different excitation profiles was performed (Kask, Gunther et al. 1997). Another possible way to estimate the data quality is to calculate standard deviations of multiple temporal autocorrelation functions (ACFs) (Starchev, Ricka et al. 2001; Wohland, Rigler et al. 2001). Even though this improves the reliability of data evaluation, it is time-consuming and not feasible for a non-stationary system.

The noise of the measured autocorrelation function comes from two sources. One is the fluctuations due to the imperfect measurements of the fluorescent light intensity in the photon-counting process (Qian and Elson 1990). Another is the stochastic nature of the observed fundamental processes, i.e., diffusion, chemical reaction, or photo-decomposition (Koppel 1974). Of the two, the first one is uncorrelated and the second one is correlated. Fluorescence fluctuations are recorded by either a photomultiplier tube (PMT) or avalanche photodiode (APD) (Magde, Elson et al. 1974). ACFs are then computed from measured photon counts by a hardware correlator. The ACFs have characteristic noise features, which depend both on the measurement system and on the computation manner of the correlation function. It has been pointed out that multitaу correlators result in correlated, inhomogeneous noise that decays with increasing lag time. Moreover, ignoring noise correlations in the analysis of ACFs may result in over-fitting and thus improper interpretation of FCS data (Schäzel and Peters 1991).

A general method to determine the best fitting model is to use maximum likelihood estimation (MLE) to fit one or more models to measured ACFs, and employ reduced χ^2 values to select the best fitting model (Meseth, Wohland et al. 1999; Meacci, Ries et al. 2006). However, MLE calculates a point estimate of the model parameters via maximization of the foregoing probability, which is equivalent to minimization of the sum of the squared errors as conventionally performed when calculating the goodness-of-fit measure χ^2 . Therefore, this method tends to favor complex models that over-fit measured data (Posada and Buckley 2004; Sivia and Skilling 2006; Gregory 2005). Besides, it can only support pairwise comparisons and thus cannot rank several competing or possible models at the same time by their relative probabilities.

In the applications with the use of FPs, more concerns are met in model selection. Even though they can provide acceptable fluorescence signal per molecule, most FPs have more than one photodynamic process, which makes the model selection complicated (see 1.2.1). In solution, besides the diffusion component, multiple exponential decay components need to be included in modified autocorrelation functions to describe the blinking processes (Widengren, Mets et al. 1999; Haupts, Maiti et al. 1998). In the case of unclear dynamic processes, several models need to be tested to find out the optimum representations (Chen, Rhoades et al. 2007). This is not uncommon in *in vivo* studies.

In living system, the signal-to-noise ratio is usually not as good as in solution due to the increased background noise caused by the thick tissue. Moreover, the experimental condition is restricted to low excitation intensity and short acquisition time due to the photobleaching and optic saturation (Delon, Usson et al. 2006; Tcherniak, Reznik et al. 2009). The biological heterogeneity also makes it worse

(Milon, Hovius et al. 2003; Hac, Seeger et al. 2005). Therefore, the signal-to-noise ratio can only be improved to a certain level. It has been reported that multicomponent models are needed to fit intracellular measurement from both autofluorescence and micro injected Cy3 and Cy3-labeled dextran in the cell (Brock, Hink et al. 1998). In Gennerich and Schild's work, they derived a modified ACF considering the confined detection volume to fit FCS data measured in small cytosolic compartments (Gennerich and Schild 2000).

Besides the confined detection volume, another issue under debate is the anomalous diffusion in which the mean squared displacement (MSD) of a particle is a non-linear function of time. This could be a result of immobile obstacles, binding to traps or any other kind of spatial heterogeneity (Bouchaud and Georges 1990; Saxton 2007). In FCS, these motions can be characterized by introducing the anomaly degree of the diffusion α in the theoretical model (Feder, Brust-Mascher et al. 1996). The value of α is 1 for free diffusion while it takes some other values smaller or larger than 1 for anomalous diffusion. However, it has also been pointed out that cautions in fitting model selection and theoretical constraints are needed to assess this phenomenon with FCS (Milon, Hovius et al. 2003; Malchus and Weiss 2010). In Schwille's work, both anomalous diffusion and two-species diffusion in two dimensions could be used to describe DiI-C12 diffusion in the plasma membrane. The results led to two different explanations for the underlying process (Schwille, Korlach et al. 1999). The same phenomenon was also observed in monitoring EGFP and EGFP tagged proteins in nuclei (Wachsmuth, Waldeck et al. 2000). In the bacterium *Escherichia coli*, several diffusion models including an exchange model between a diffusing and an immobile state have been evaluated to characterize the Min-proteins dynamics (Meacci, Ries et al. 2006). In *Drosophila* embryos, to determine the morphogen Bcd mobility in nuclei,

different diffusion models including both simple and anomalous diffusion with different assumptions about EGFP photophysics were examined (Abu-Arish, Porcher et al. 2010). However, only the simplest one species model was shown not to be able to adequately fit the data, the others cannot be differentiated from each other. Finally, the authors used the average value to estimate the mobility. It is undoubted that comparing possible models one by one for each measurement is tedious and time consuming. Therefore, it is of great interest to have an objective and unbiased approach to FCS data model evaluation.

Recently, such an approach based on Bayesian inference, has been reported (He, Guo et al. 2012; Guo, He et al. 2012). The model probabilities are calculated as the conditional probabilities using the Bayes' rule (details in Chapter 3). It has been shown that this Bayesian approach provides a reliability test for simulated FCS data under different levels of noise as well as complex multi-component systems. In this approach, the noise and the noise correlation are estimated from either multiple ACFs or single intensity traces for the following model probabilities calculation. The capability of this approach in the analysis of stimulated data under various conditions has been demonstrated. In experimental FCS measurements, it resolves the triplet state of Fluorescein at appropriate excitation intensity. Moreover, it detects two diffusing component in mixtures of Atto565 and Atto565-labeled streptavidin with distinct ratios. The results demonstrate the capability of the Bayesian approach in experimental systems. Therefore, it is of great practical meaning to apply this method to determine the appropriate fitting models for FCS measurement using typical FPs both *in vitro* and *in vivo*.

In summary, FCS is an ultrasensitive fluorescence technique, developed to measure molecular dynamics at the single molecule level. It can provide both quantitative and

qualitative information not only *in vitro* but also *in vivo*. In view of the robustness of this approach, it is worthwhile to extend FCS technique in monitoring protein behavior during zebrafish development. On the other hand, FCS data fitting for fluorescent proteins remains an issue and needs to be explored. The current work deals with these issues in detail. The thesis contains six chapters and is structured into the following sections:

Chapter 2 introduces the basic principles and instrumentation of FCS. The autocorrelation and its theoretical models will be introduced. The experimental materials and methods will also be covered.

Chapter 3 introduces the principles of Bayesian model selection approach. The model probability calculation, the principle of Bayesian inference, the Bayesian model selection as well as the noise estimation procedures will be explained. Its capability in evaluating the experimental data will also be demonstrated.

Chapter 4 investigates the fitting model selection for widely used fluorescent proteins, EGFP, EYFP and mCherry, both *in vitro* and *in vivo*. The influence on model selection from excitation intensity, acquisition time and experiment temperature will be discussed. The appropriate fitting model for fluorescent proteins in solution and in cytoplasm, nucleus as well as on membrane will be determined. This methodology will be further employed in the determination of fitting models for EGFP labeled proteins in zebrafish embryos.

Chapter 5 applies FCS to analyze transgenic zebrafish lines expressing recombinant Wnt3EGFP fusion protein. The protein dynamics in different cell compartments in zebrafish cerebellum will be characterized. The transportation mechanism of Wnt3EGFP will be explored. The *in vivo* role of Wnt3 in neural patterning and growth will be addressed.

Finally, Chapter 6 concludes and presents an outlook for future research.

Chapter 2

Materials and Methods

2.1. Fluorescence Correlation Spectroscopy (FCS)

2.1.1. Theory

FCS extracts information from fluorescence signal fluctuations in a small observation volume. Fluorescence fluctuations are generated by fluorophores moving in and out of the observation volume, such as diffusion and flow, or the processes which change the fluorescence property of the fluorophore during its residence time, such as blinking and chemical reactions. The size and shape of the observation volume depend on the illumination and detection setup. In confocal microscope, the observation volume is created by focusing a laser to a diffraction limited volume. Its size is on the order of femtolitres (fL).

FCS data processing is demonstrated in Fig. 2.1. First, the fluorescence intensity trace is recorded as fluorophores pass through the observation volume (Fig. 2.1A and B). The fluorescence signal is then analyzed by its temporal autocorrelation, in which the intensity is correlated with its time-shifted replica at different lag times τ (Fig.2.1C). At τ_0 ($\tau = 0$), the replica is identical to the original trace and thus results in the highest correlation value. With increasing τ , the replicas are less and less similar to the original one and thereby the correlation values decrease. Eventually, the intensity trace is transformed into a decay curve (Fig. 2.1D). The shape of the correlation curve provides information of the underlying processes. The width of the curve represents the average residence time of the fluorophore in the observation volume and thereby

shows mobility of the fluorophore. The amplitude of the curve reflects the number of particles in the observation volume and can be used to calculate the local concentration. In practice, such information can be extracted from the experimental autocorrelation curve by fitting with theoretical models (Fig. 2.1E).

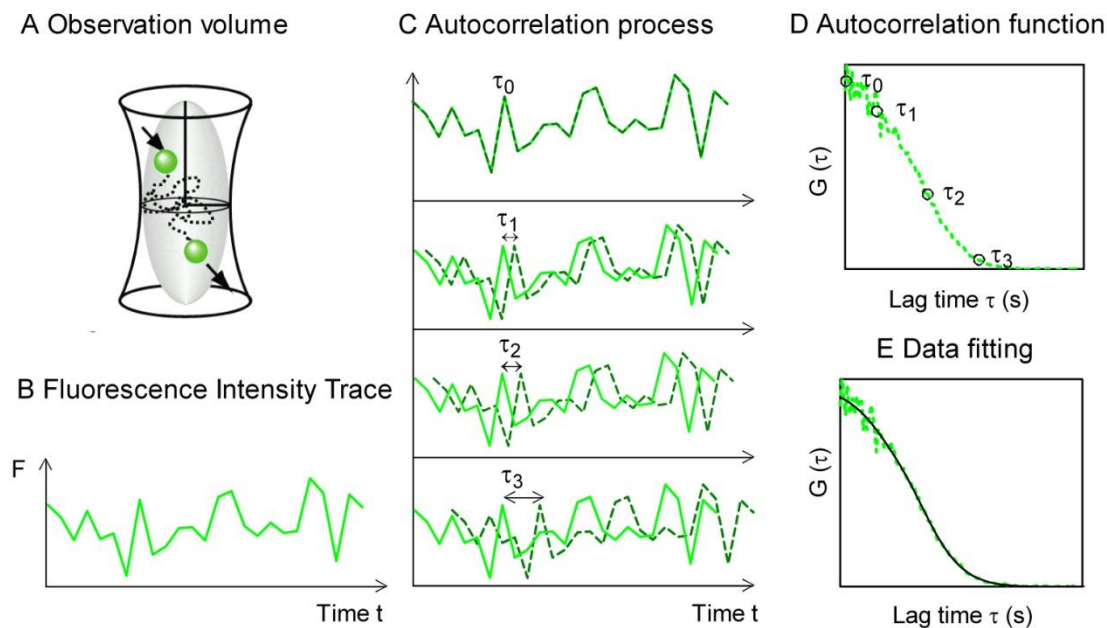


Figure 2.1 Overview of FCS data processing

(A) Observation volume of around 0.5 fL; (B) Fluorescence intensity time trace; (C) Autocorrelation process: the original intensity trace (light solid line) is correlated with its time-shifted replica (dark dashed line) at different lag time τ ; (D) Autocorrelation function; (E) Data fitting with theoretical model (black line).

The fluorescence fluctuation at time t is given by:

$$\delta F(t) = F(t) - \langle F(t) \rangle \quad (2.1)$$

where $F(t)$ is the fluorescence intensity at time t ; $\langle \rangle$ denotes time average. $F(t)$ is calculated by:

$$\langle F(t) \rangle = \frac{1}{T} \int_0^T F(t) dt \quad (2.2)$$

The normalized autocorrelation function (ACF) can be written as:

$$G(\tau) = \frac{\langle F(t)F(t + \tau) \rangle}{\langle F(t) \rangle^2} \quad (2.3)$$

where τ is the lag time. Substituting Eq. 2.1 into Eq. 2.3:

$$G(\tau) = \frac{\langle F(t)F(t + \tau) \rangle}{\langle F(t) \rangle^2} = \frac{\langle (\delta F(t) + \langle F \rangle)(\delta F(t + \tau) + \langle F \rangle) \rangle}{\langle (\delta F(t) + \langle F \rangle) \rangle^2}$$

$$= \frac{\langle \delta F(t)\delta F(t + \tau) + \langle F \rangle^2 \rangle}{\langle F \rangle^2} = \frac{\langle \delta F(t)\delta F(t + \tau) \rangle}{\langle F(t) \rangle^2} + 1 \quad (2.4)$$

2.1.2. Theoretical ACF models

The fluorescence intensity $F(t)$ and its fluctuation $\delta F(t)$ can be written as:

$$F(t) = \eta \langle C \rangle \int MDE(\vec{r}) d\vec{r} \quad (2.5)$$

$$\delta F(t) = \eta \int MDE(\vec{r}) \delta C(\vec{r}, t) d\vec{r} \quad (2.6)$$

where η is brightness; $\langle C \rangle$ is the average concentration; $MDE(\vec{r})$ is the molecular detection efficiency; $\delta C(\vec{r}, t)$ is the concentration fluctuation of the fluorescent particle at positions \vec{r} and time t . η is determined by the absorption coefficient and the molecular quantum yield of the fluorophore and the detection efficiency of the instrument. Therefore, it depends on the excitation intensity. A higher η provides better signal-to-noise ratio (Koppel 1974). In practice, this can be achieved by increasing excitation intensity or by using fluorophores with high quantum yield. η is defined as photon count per particle per second (cps) and can be calculated by dividing the average fluorescence $F(t)$ by the average number of fluorophores (see Section 2.1.4). $MDE(\vec{r})$ describes the spatial distribution of the effective observation volume. It is a product of the spatial intensity profile of the exciting laser beam and the fluorescence detection probability. Assuming a three-dimensional (3D) Gaussian profile, it can be written as:

$$MDE(\vec{r}) = I_0 \exp\left[\frac{-2(x^2 + y^2)}{\omega_0^2}\right] \exp\left(\frac{-2z^2}{\omega_z^2}\right) \quad (2.7)$$

where ω_0 and ω_z are the radial and axial distances of the excitation beam profile where the excitation intensity reaches $1/e^2$ of its value at the center of the observation volume respectively.

Substituting these expressions into the normalized autocorrelation function Eq. 2.4 yields:

$$G(\tau) = \frac{\eta^2 \iint MDE(\vec{r})MDE(\vec{r}') \langle \delta C(\vec{r}, t) \delta C(\vec{r}', t + \tau) \rangle d\vec{r} d\vec{r}'}{(\eta \langle C \rangle \int MDE(\vec{r}) d\vec{r})^2} + 1 \quad (2.8)$$

The calculation of the integration has been demonstrated in details elsewhere (Aragón and Pecora 1976). Different diffusion modes and any other dynamical processes such as fluorophore blinking contribute to $\langle \delta C(\vec{r}, t) \delta C(\vec{r}', t + \tau) \rangle$ differently. Therefore, the theoretical models are different after integration (Fig. 2.2A). For single component (1p) 3D Brownian diffusion through a Gaussian laser profile, the theoretical ACF is given by:

$$G_{3D,1p}(\tau) = \frac{1}{N} \left(1 + \frac{\tau}{\tau_D}\right)^{-1} \left[1 + \frac{1}{K^2} \left(\frac{\tau}{\tau_D}\right)\right]^{-1/2} + G(\infty) \quad (2.9)$$

with

$$N = \langle C \rangle \pi^{3/2} \omega_0^2 \omega_z = \langle C \rangle V_{eff} \quad (2.10)$$

$$\tau_D = \frac{\omega_0^2}{4D} \quad (2.11)$$

$$K = \frac{\omega_z}{\omega_0} \quad (2.12)$$

where N is the average number of molecules in the observation volume; τ_D is the diffusion time, i.e., the time fluorophores take to pass through the observation volume; G_∞ is the convergence value of the ACF for long lag times with the expected value of 1; V_{eff} is the effective observation volume; D is the diffusion coefficient of the fluorophore; K describes the shape of the observation volume.

For the previously mentioned (see Section 1.2.2) 3D anomalous diffusion (Schwille, Korlach et al. 1999):

$$G_{3D,Ano}(\tau) = \frac{1}{N} \left[1 + \left(\frac{\tau}{\tau_D} \right)^\alpha \right]^{-1} \left[1 + \frac{1}{K^2} \left(\frac{\tau}{\tau_D} \right)^\alpha \right]^{-1/2} + G_\infty \quad (2.13)$$

where α is the anomaly degree of the diffusion. The value of α is 1 for free diffusion while it takes values smaller than 1 for hindered diffusion and larger than 1 for direct transport or super-diffusion (Feder, Brust-Mascher et al. 1996).

For membrane measurements, 2D or planar free diffusion models (Elson and Magde 1974) are used:

$$G_{2D,1p}(\tau) = \frac{1}{N} \left(1 + \frac{\tau}{\tau_D} \right)^{-1} + G_\infty \quad (2.14)$$

For multiple diffusion components in 2D and 3D (Thompson 1991; Kinjo and Rigler 1995):

$$G_{3D,2p}(\tau) = \frac{1}{N} \left(\begin{array}{l} (1 - F_2) \left(1 + \frac{\tau}{\tau_{D1}} \right)^{-1} \left[1 + \frac{1}{K^2} \left(\frac{\tau}{\tau_{D1}} \right)^\alpha \right]^{-1/2} \\ + F_2 \left(1 + \frac{\tau}{\tau_{D2}} \right)^{-1} \left[1 + \frac{1}{K^2} \left(\frac{\tau}{\tau_{D2}} \right)^\alpha \right]^{-1/2} \end{array} \right) + G_\infty \quad (2.15)$$

$$G_{2D,2p}(\tau) = \frac{1}{N} \left[(1 - F_2) \left(1 + \frac{\tau}{\tau_{D1}} \right)^{-1} + F_2 \left(1 + \frac{\tau}{\tau_{D2}} \right)^{-1} \right] + G_\infty \quad (2.16)$$

where F_2 is the fraction of the second component. This expression is only valid when the two species have the same molecular brightness. These equations are helpful in detecting interactions and viscosity change. When a fluorescently labeled molecule binds to a bigger unlabeled molecule, a change in the diffusion time should be observed. Similarly, when a fluorescently labeled molecule moving within a membrane, a longer diffusion time should be detected compared with the molecule in the cytoplasm. The fraction of the slow moving component can be determined from this equation. However, in order to differentiate the changes in diffusion times in a

FCS experiment, the diffusion times of the two situations need to differ by at least 1.6 times (Meseth, Wohland et al. 1999).

For even more complex system, three components may need to be included:

$$G_{3D,3p}(\tau) = \frac{1}{N} \left(\begin{array}{l} (1 - F_2 - F_3) \left(1 + \frac{\tau}{\tau_{D1}}\right)^{-1} \left[1 + \frac{1}{K^2} \left(\frac{\tau}{\tau_{D1}}\right)\right]^{-1/2} \\ + F_2 \left(1 + \frac{\tau}{\tau_{D2}}\right)^{-1} \left[1 + \frac{1}{K^2} \left(\frac{\tau}{\tau_{D2}}\right)\right]^{-1/2} \\ + F_3 \left(1 + \frac{\tau}{\tau_{D3}}\right)^{-1} \left[1 + \frac{1}{K^2} \left(\frac{\tau}{\tau_{D3}}\right)\right]^{-1/2} \end{array} \right) + G_{\infty} \quad (2.17)$$

At higher laser intensities, a triplet state of the fluorophore can be populated. This intersystem crossing between singlet and triplet states can cause characteristic fluctuations in the fluorescence signal. Typical triplet states have kinetics occurring on a timescale that is much faster than the diffusion time (Widengren, Mets et al. 1995; Widengren, Mets et al. 1999). Therefore, it results in an additional shoulder at small τ values in the ACF (Fig. 2.2B). Under this circumstance, a function that describes the triplet state kinetic needs to be multiplied with the basic correlation functions:

$$G_{3D,1p1t}(\tau) = \frac{1}{N} \left(1 + \frac{\tau}{\tau_D}\right)^{-1} \left[1 + \frac{1}{K^2} \left(\frac{\tau}{\tau_D}\right)\right]^{-1/2} f_{trip}(\tau) + G(\infty) \quad (2.18)$$

where

$$f_{trip}(\tau) = \left(\frac{F_{trip}}{1 - F_{trip}}\right) \exp\left(-\frac{\tau}{\tau_{trip}}\right) + 1 \quad (2.19)$$

F_{trip} is the fraction of the particles in the triplet state; τ_{trip} is the triplet state relaxation time. For a fluorophore, other fast blinking processes that are a reversible transition between a bright fluorescent state to a dark non-fluorescent state can also be expressed by this triplet state dynamic and accounted in its ACF. These blinking processes can be photo-induced isomerization (Widengren, Mets et al. 1999; Widengren and Schwille 2000; Widengren and Seidel 2000) or constitute an

equilibrium between protonation state and deprotonation states (Haupts, Maiti et al. 1998). Therefore, considering the triplet, the above equations are modified:

$$G_{2D,1p1t}(\tau) = \frac{1}{N} \left(1 + \frac{\tau}{\tau_D}\right)^{-1} f_{trip}(\tau) + G_\infty \quad (2.20)$$

$$G_{3D,2p1t}(\tau) = \frac{1}{N} \left(\begin{array}{l} (1 - F_2) \left(1 + \frac{\tau}{\tau_{D1}}\right)^{-1} \left[1 + \frac{1}{K^2} \left(\frac{\tau}{\tau_{D1}}\right)\right]^{-1/2} \\ + F_2 \left(1 + \frac{\tau}{\tau_{D2}}\right)^{-1} \left[1 + \frac{1}{K^2} \left(\frac{\tau}{\tau_{D2}}\right)\right]^{-1/2} \end{array} \right) f_{trip}(\tau) + G_\infty \quad (2.21)$$

$$G_{2D,2p1t}(\tau) = \frac{1}{N} \left[(1 - F_2) \left(1 + \frac{\tau}{\tau_{D1}}\right)^{-1} + F_2 \left(1 + \frac{\tau}{\tau_{D2}}\right)^{-1} \right] f_{trip}(\tau) + G_\infty \quad (2.22)$$

$$G_{3D,3p1t}(\tau) = \frac{1}{N} \left(\begin{array}{l} (1 - F_2 - F_3) \left(1 + \frac{\tau}{\tau_{D1}}\right)^{-1} \left[1 + \frac{1}{K^2} \left(\frac{\tau}{\tau_{D1}}\right)\right]^{-1/2} \\ + F_2 \left(1 + \frac{\tau}{\tau_{D2}}\right)^{-1} \left[1 + \frac{1}{K^2} \left(\frac{\tau}{\tau_{D2}}\right)\right]^{-1/2} \\ + F_3 \left(1 + \frac{\tau}{\tau_{D3}}\right)^{-1} \left[1 + \frac{1}{K^2} \left(\frac{\tau}{\tau_{D3}}\right)\right]^{-1/2} \end{array} \right) f_{trip}(\tau) + G_\infty \quad (2.23)$$

For fluorophores with multiple blinking processes, the ACF should be revised as below (Widengren, Mets et al. 1999):

$$G_{3D,1p2t}(\tau) = \frac{1}{N} \left(1 + \frac{\tau}{\tau_D}\right)^{-1} \left[1 + \frac{1}{K^2} \left(\frac{\tau}{\tau_D}\right)\right]^{-1/2} f_{trip1}(\tau) f_{trip2}(\tau) + G_\infty \quad (2.24)$$

$$G_{2D,1p2t}(\tau) = \frac{1}{N} \left(1 + \frac{\tau}{\tau_D}\right)^{-1} f_{trip1}(\tau) f_{trip2}(\tau) + G_\infty \quad (2.25)$$

Some theoretical ACFs are shown in Fig. 2.2A and B. The equations listed above are used in this study. A more comprehensive list of ACF models has been reported (Shi and Wohland 2009).

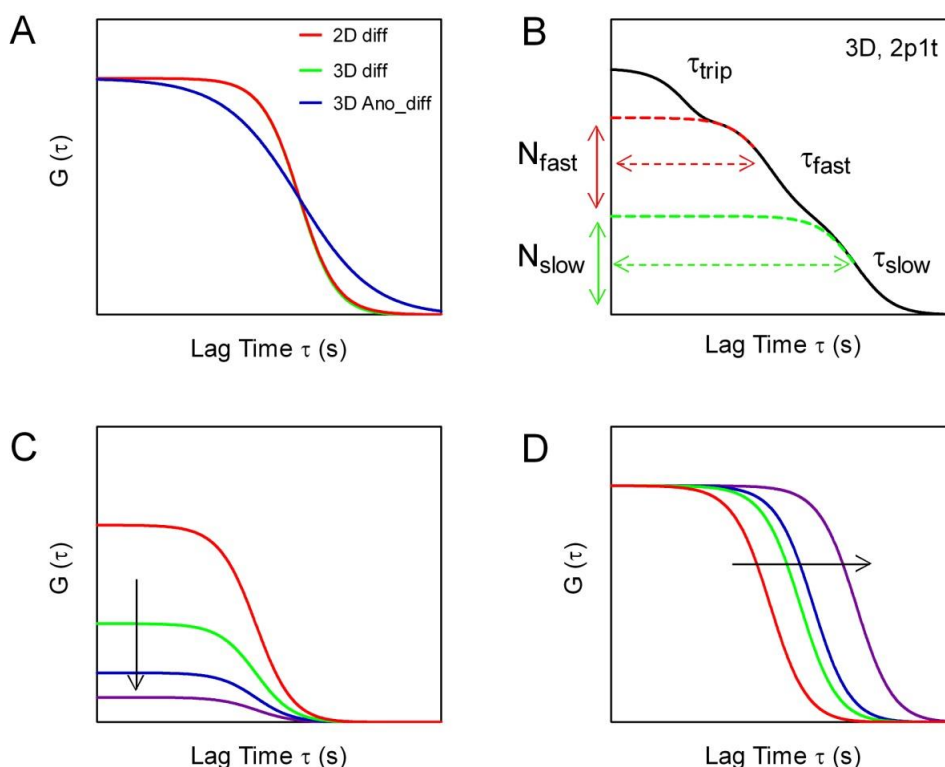


Figure 2.2 Characteristics of fluorescence correlation functions

(A) Shapes of the ACFs with different diffusion processes. (B) A representative fitting using three-dimensional two-component model with triplet state. (C) Changes in an ACF due to changes in concentration; the arrow indicates increasing concentration. (D) Changes in an ACF for different diffusion times; the arrow indicates increasing diffusion time.

2.1.3. Parameters

From Eq. 2.9, the amplitude of the ACF is:

$$G(0) = \frac{1}{N} + G(\infty) \quad (2.26)$$

from where the average number of particles in the observation volume is given by:

$$N = \frac{1}{G(0) - G(\infty)} \quad (2.27)$$

A more concentrated sample will result to lower amplitude (Fig. 2.2C). To distinguish the intensity fluctuations caused by molecules moving in and out of the observation volume compared to the average intensity from the molecules remaining in the volume, the number of particle should be kept at low level. This can be

achieved by creating a small observation volume or using samples with low concentration. In general, FCS can measure samples with about 0.1 - 1000 particles per observation volume, which is equivalent to sub-nanomolar to a low micromolar concentration range in confocal FCS.

The background stemming from detector noise or scattered light from the sample decreases the amplitude of the ACF, which leads to an overestimated N . The N calculated directly from Eq. 2.27 is the apparent number of particle N_{app} . The actual number of particles N can be corrected for the background (β), which can be determined from a blank measurement (Koppel, 1974). Assuming the brightness of a fluorescent protein is η , N is given by:

$$1/N = \frac{\eta^2 N}{(\eta N)^2} \quad (2.28)$$

where

$$\eta = \frac{F_{mean} - \beta}{N} \quad (2.29)$$

It is the brightness after background correction. N_{app} , is then given by:

$$1/N_{app} = \frac{\eta^2 N}{(\eta N + \beta)^2} \quad (2.30)$$

From Eq. 2.29:

$$F_{mean} = \eta N + \beta \quad (2.31)$$

Dividing (2.30) by (2.28) and using (2.31) we obtain

$$N/N_{app} = \frac{\eta^2 N}{(\eta N + \beta)^2} \times \frac{(\eta N)^2}{\eta^2 N} = \frac{(\eta N)^2}{(\eta N + \beta)^2} = \frac{(F_{mean} - \beta)^2}{F_{mean}^2} \quad (2.32)$$

This can be rewritten as,

$$N = \frac{N_{app} \times (F_{mean} - \beta)^2}{F_{mean}^2} \quad (2.33)$$

It is the actual number of particle. With N , the actual brightness can also be corrected using Eq. 2.29.

The size of the observation volume V_{eff} can be estimated from a calibration using a dye with known diffusion coefficient by the following equation:

$$V_{eff} = \pi^{3/2} \omega_0^2 \omega_z = K \pi^{3/2} \omega_0^3 \quad (2.34)$$

where ω_0 can be estimated from Eq. 2.11. Then, the absolute concentration (C_i) of a sample and its diffusion coefficient (D) can be determined by Eq. 2.35 and 2.36:

$$C_i = \frac{N}{N_A V_{eff}} \quad (2.35)$$

$$D = \frac{\tau_{D0} D_0}{\tau_D} \quad (2.36)$$

where τ_{D0} and D_0 are diffusion time and diffusion coefficient of the calibration dye, respectively.

D is the diffusion coefficient of the particles. The hydrodynamic radius of a particle can be estimated by FCS using the Stokes-Einstein relation:

$$D = \frac{kT}{6\pi\eta r} \quad (2.37)$$

where k is Boltzmann's constant; T is the absolute temperature; η is the viscosity of the medium; r is the hydrodynamic radius of the particle. For a spherical particle with radius r and molecular mass M , τ_D is proportional to $\sqrt[3]{M}$. Hence a large particle will diffuse slower (larger τ_D) and will generate fluctuations with wider width (Fig. 2.2D).

2.1.4. Instrument setup

The FCS setup (Fig. 2.3) was described previously in details (Pan, Foo et al. 2007). Briefly, FCS was performed using a customized Olympus FV 300 confocal microscope equipped with four laser lines 488/514 nm Argon, 543 nm and 633 nm (Olympus, Tokyo, Japan). Excitation was provided by lasers with specific wavelength

that is focused into samples by a water-immersion objective (60 \times , NA 1.2; Olympus, Tokyo, Japan). The laser power was measured before the objective. The emitted light, which passed an internal 3x magnification stage in the confocal microscope, passed through a 150 μ m pinhole. A 50/50 beam splitter* (Thorlabs, Newton, NJ) was used to split the emission light into two channels, to eliminate the afterpulsing effect of the detectors in FCS measurements (Zhao, Jin et al. 2003). The light then was focused through band-pass filters onto avalanche-photodiode detectors (SPCM-AQR-14; Pacer, Berkshire, UK). The intensity history was recorded and its autocorrelation curves were computed online using a hardware correlator (Flex02-01D; Correlator.com, Bridgewater, NJ, USA). Curve fitting was performed by a self-written program in Igor Pro 6.0 (WaveMetrics, Lake Oswego, OR). In Bayesian analysis, photon arrival times (PAT) were recorded by the photon history recorder, which transferred the time difference between successive photon events to the host PC hard drive. The recorded data was 16 bit format. Curve fitting and model probabilities calculation were performed by a MATLAB program (The MathWorks, Inc., Natick, MA), which was described previously in detail (He, Guo et al. 2012; Guo, He et al. 2012). The principles of Bayesian analysis will be introduced in Chapter 3. The laser wavelength and corresponding band-pass filters are listed in Table 2.1.

*It was not used in zebrafish measurements.

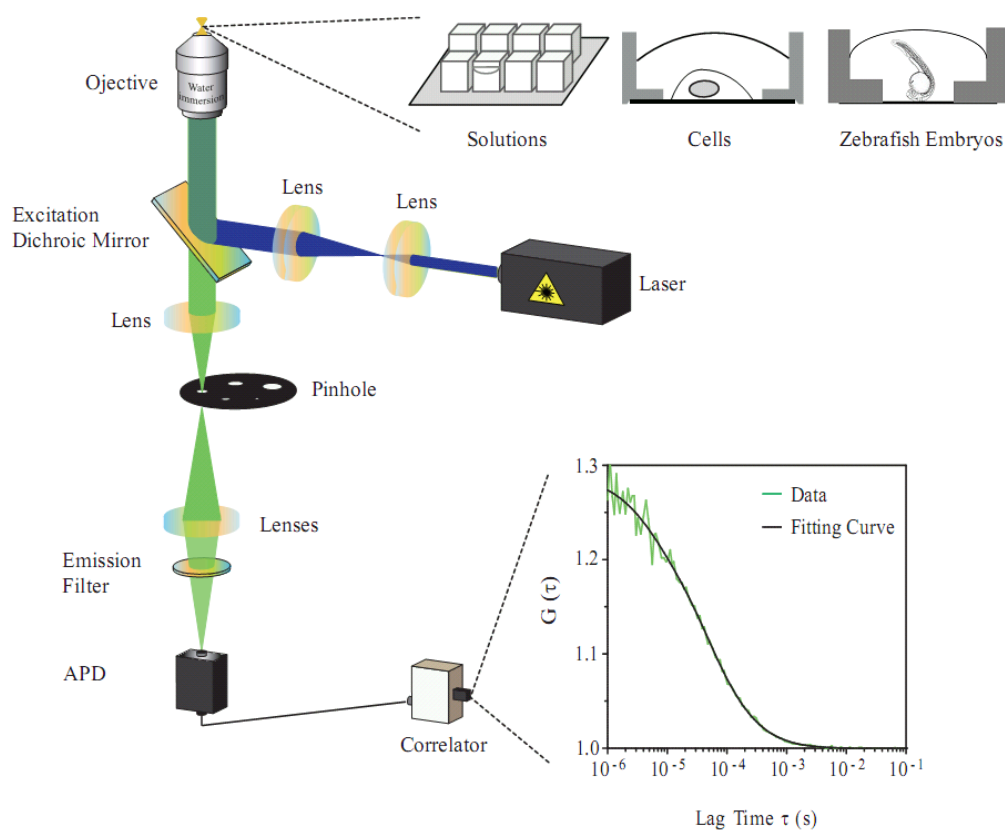


Figure 2.3 FCS setup

2.1.5. Calibration

2.1.5.1. Samples

Calibration measurements were routinely performed before the measurement. The calibration dyes used for each laser line are listed in Table 2.1. 60 μL 5 nM sample solution was used. The laser power before the objective was 25 μW . The estimated observation volume V_{eff} was 6.60×10^{-16} L. FCS data was fitted with Eq. 2.18. Typical results of all fitting parameters are listed in Table 2.2.

Table 2.1 List of laser wavelength, filters and calibration dyes

Laser Wavelength (nm)	Filter	Calibration dye	D ($\mu\text{m}^2\text{s}^{-1}$)
488	513/17-25 ^a	Atto488	400 ^[1]
515	545AF35 ^b	Rhodamine 6G	425 ^[2]
543	593/40-25 ^a	Atto565	259 ^[3]

^[1] Dertinger and Ewers 2008; ^[2] Müller, Loman et al. 2008; ^[3] Pan, Aw et al. 2006.

^a Semrock, Rochester, NY; ^bOmega, Brattleboro, VT.

Table 2.2 Typical values of fitting parameters for calibration using Atto488

Fitting Parameters	Fitting Value
N	2.23 \pm 0.05
τ_D (μs)	45 \pm 1
τ_{trip} (μs)	6 \pm 2
F _{trip} (%)	17 \pm 2
K	5.51 \pm 0.70
G(∞)	0.9999 \pm 0.0001

Data = mean \pm SD

2.1.5.2. Background determination

The background was measured using 300 μL 1x PBS buffer. The laser power was measured before the objective. The measured background consisted of both detector dark counts (220 ± 2 Hz) and the light scattered from the solution. Both the total background and the background from solution were listed in Table 2.3a. The background from solution increases by the laser power. The total background from cells was listed in Table 2.3b.

Table 2.3a Background measurement at different laser power in 1x PBS

Laser Power (μW)	Total Background		Background from Solution	
	Photon Counts per second (Hz)			
Excitation Laser (nm)	488	514	488	514
5	282 \pm 6	239 \pm 3	62 \pm 6	19 \pm 3
10	303 \pm 2	241 \pm 8	83 \pm 2	21 \pm 8
20	337 \pm 14	268 \pm 5	117 \pm 14	48 \pm 5
30	375 \pm 9	282 \pm 9	155 \pm 9	62 \pm 9
40	421 \pm 12	294 \pm 7	201 \pm 12	74 \pm 7
60	485 \pm 7	325 \pm 7	265 \pm 7	105 \pm 7
80	585 \pm 8	352 \pm 10	365 \pm 8	132 \pm 10
100	678 \pm 13	388 \pm 14	458 \pm 13	168 \pm 14
200	1098 \pm 19	550 \pm 6	878 \pm 19	330 \pm 6

Data = mean \pm SD

Table 2.3b Background measurement at different laser power in cells

Laser Power (μW)		Total Background Photon Counts per second (Hz)		
Excitation Laser (nm)		488	514	543
Cytoplasm	5	2735 \pm 277	970 \pm 25	661 \pm 89
	10	3415 \pm 691	1290 \pm 159	863 \pm 317
	20	5175 \pm 540	1575 \pm 73	1099 \pm 133
Nucleus	5	2374 \pm 321	895 \pm 35	871 \pm 19
	10	2290 \pm 138	1192 \pm 51	983 \pm 298
	20	2893 \pm 239	1765 \pm 117	1755 \pm 607

Data = mean \pm SD

2.1.5.3. Excitation intensity

From Eq. 2.11, ω_0 can be calculated using dyes with known diffusion coefficient by:

$$\omega_0 = (4D_0\tau_{D0})^{1/2} \quad (2.38)$$

And the excitation intensity (E.I.) under certain laser power (L.P.) can be calculated by:

$$E.I. = \frac{L.P.}{\pi\omega_0^2} \quad (2.39)$$

The excitation intensities measured in this study is listed in Table 2.4 and the ω_0 with different pinhole set is listed in Table 2.5.

Table 2.4 Laser power - excitation intensity

Laser Power (μW)	Excitation Intensity (kW/cm^2)
5	2
10	4
20	8
30	13
40	17
50	20
60	25
80	34
100	42
200	85

Table 2.5 Pinhole set - ω_0

Pinhole set	Pinhole Size (nm)	τ_D (μs)	ω_0 (μm)
1	60	23.8 ± 1.2	0.20
2	100	28.5 ± 1.2	0.21
3	150	43.0 ± 2.1	0.26
4	200	57.1 ± 1.0	0.30
5	300	80.1 ± 11.1	0.36

Data are mean \pm SD. Laser power for this measurement was 30 μW .

2.1.5.4. Experiments

The experimental conditions are listed in Table 2.6. The laser power was measured before the objective. The measurements were performed at room temperature unless stated otherwise.

Table 2.6 Experimental conditions

Sample	Species	L.P. (μ W)	Acquisition time (s)
Solutions	Atto488, Fluorescein, Rhodamine 6G EGFP, EYFP, mCherry	5, 10, 20, 30, 40, 50, 60, 80, 100, 200	40
Cells	Transfected with EGFP, EYFP, mCherry, PMT-EGFP	5, 10, 20, 30, 60	10
Zebrafish embryos	EGFP labeled proteins	15	15

2.2. Sample preparation

2.2.1. Preparation of solution sample

Atto488, Fluorescein, Rhodamine 6G, Atto565, Atto565-labeled streptavidin (Sigma-Aldrich, Singapore) were dissolved in dimethyl sulfoxide (DMSO) and diluted with 1x PBS (phosphate buffered saline, pH 7.4, Invitrogen, CA, US). The stocks were stored at 4 °C fridge and diluted to 5 nM for calibration and 10 nM for measurement (calculated based on the number of particles extracted from FCS). Fluorescent proteins, EGFP, EYFP, mCherry (BioVision, CA, USA), were diluted in 1x PBS. The stocks were stored at -20 °C fridge and diluted to 10 nM for measurement. All sample solutions were placed on an 8 well chamber slide (Lab-Tek, NY, USA) for

measurement. The chamber was coated with BSA (Albumin from Bovine Serum, Sigma-Aldrich, Singapore) to avoid protein adhesion. BSA (1 g/100 L in 1x PBS buffer) solution was placed in the chamber and then incubated at 4 °C for 24 h.

2.2.2. Preparation of cell sample

2.2.2.1. Cell culture

All experiments are performed on CHO-K1 (Chinese hamster ovary) cells. Measurements are performed in cytoplasm, nucleus and on membrane. CHO-K1 cells were obtained from ATCC (Manassas, VA, US) and cultivated in Dulbecco's modified eagle medium (DMEM, Invitrogen, Singapore), supplemented with 10% fetal bovine serum (FBS, Invitrogen, Singapore) and 1% penicillin and streptomycin (PS, PAA, Austria). The cells were kept at 37 °C in 5% (v/v) CO₂ humidified atmosphere.

2.2.2.2. Plasmids

The pEGFP-C1 vector (Clontech) was a gift from Prof. Kozo Kaibuchi (Nagoya University Graduate School of Medicine, Nagoya, Japan). The pEYFP-C1 vector (Clontech) was a gift from Prof. Anand D Jeyasekharan (Cancer Science Institute of Singapore, Singapore). The plasmid maps of these two vectors can be found from the online vector database (<http://www.addgene.org/vector-database/>). The mCherry vector was a gift from Prof. Karuna Sampath (Department of Biological Science, National University of Singapore, Singapore) and its plasmid map is shown in Fig.

2.4.

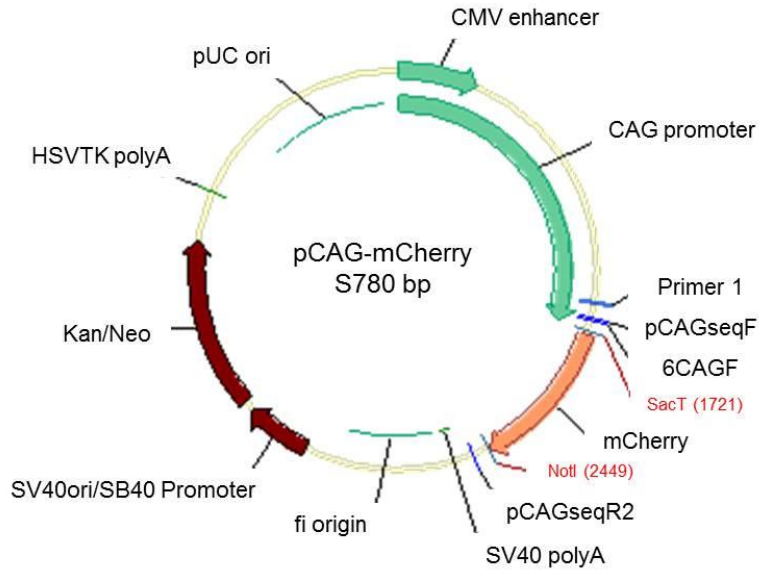


Figure 2.4 Plasmid map of mCherry

The sequence of the Plasma Membrane Targeting sequence (PMT) is:

ATGGGCTGCTTCTTCAGCAAGCGGCGGAAGAGCAAGCGGC
CGGAAGGCCG
 ACAAGGAGAGC

Its plasmid map is shown in Fig. 2.5.

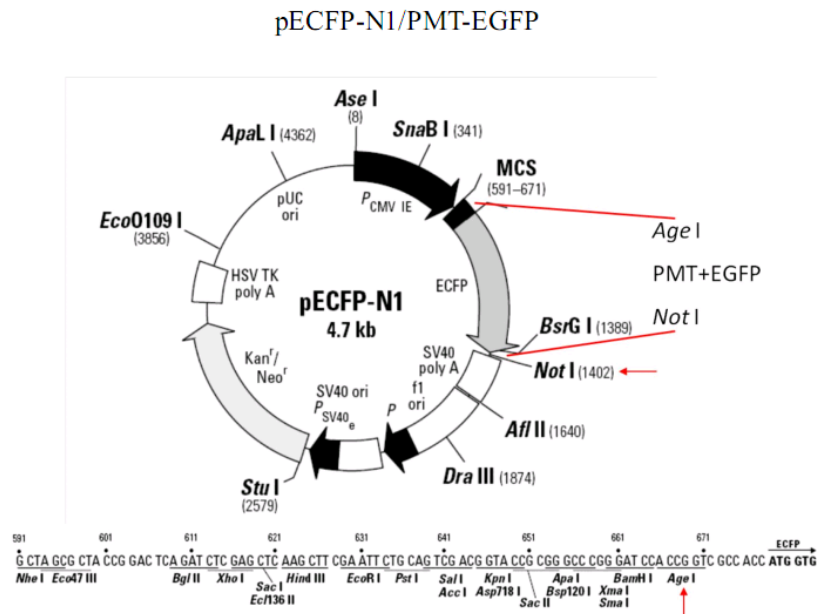


Figure 2.5 Plasmid map of PMT-EGFP

2.2.2.3. Transfection by electroporation

Electroporation was used for transfection of CHO-K1 cells. About 90% confluent cells in a 75 cm² flask were washed once with 1x PBS, trypsinized with 0.25% trypsin-0.03% EDTA solution (Invitrogen, Singapore) for 5 min at 37 °C, and then re-suspended in culture medium. Cells (~1 × 10⁶) were then precipitated by centrifugation and re-suspended in 10 µL R buffer, followed by the addition of 0.25-1 µg of plasmid DNA and electroporated in electrolyte E buffer using the preprogrammed protocol for CHO-K1 cells (Neon-Transfection system, Invitrogen, Korea). The cells were then seeded onto a No. 1.5 cover glass bottom Petri dish (MatTek, USA) and grown in the culture medium for 24–36 h. Before FCS measurements, cells were washed thoroughly with 1x PBS to avoid influence of media on fluorescence and covered with 1 ml phenol red free DMEM (Invitrogen, Singapore) supplemented with 10% FBS in the dish during measurements. To measure the cells in 37 °C condition, an LCI incubator system (LCI Live Cell Instrument, Korea) for various types of chambers was used. Samples were incubated about 15 min before the measurements.

2.2.3. Preparation of zebrafish embryos

2.2.3.1. Transgenic zebrafish lines

Transgenic zebrafish used in this research were obtained from zebrafish facility in Institute of Molecular and Cell Biology (IMCB, A*STAR, Singapore). Stable *wnt3* promoter driven transgenic lines generated for this research are Tg(-4.0*wnt3*:EGFP)^{F1}, briefly called EGFP^{F1}, for spatial temporal tracking of EGFP expression in the brain; Tg(-4.0*wnt3*:EGFP)^{F2}, briefly called EGFP^{F2}, a weaker EGFP reporter line used for FCS analysis. The *wnt3* promoter driven transgenic lines were generated by co-injection of transposase mRNA and 4kbEGFP-miniTol2 or 4kbWnt3EGFP-miniTol2

to generate $Tg(-4.0wnt3:EGFP)^{F1/F2}$ and $Tg(-4.0wnt3:Wnt3EGFP)$ respectively (Kawakami 2007. The 4kb *wnt3* promoter drives EGFP reporter expression (Fig.2.6 B, D, F) in a manner that is similar to endogenous *wnt3* mRNA transcript (Fig.2.6 A, C, E). The construction of transgenic zebrafish lines was done by Cathleen Teh (IMCB, A*STAR, Singapore). Outcome of spatial temporally regulated Wnt3EGFP expression in the brain was studied using $Tg(-4.0wnt3:Wnt3EGFP)^{F2}$, briefly called Wnt3EGFP.

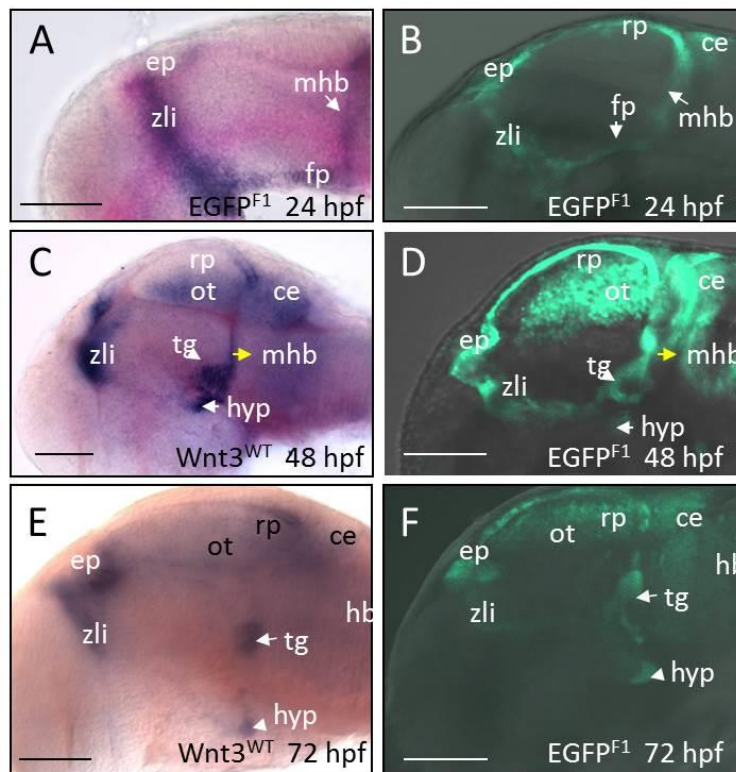


Figure 2.6 4kb *wnt3* promoter drives EGFP reporter expression in a manner similar to endogenous *wnt3* mRNA transcript

Bright field images of zebrafish embryos after whole mount in situ hybridization with antisense dioxygenin labeled EGFP (A) and Wnt3 probes (C and E). Confocal images of EGFP reporter driven by 4kb promoter expressing in brain at different development stages (B, D and F). A 100 μ m scale bar is shown in each figure. N.B.: ce: cerebellum, ep: epithalamus, fp: floor plate, hyp: caudal hypothalamus, ot: optic tectum, rp: roof plate, mhb: midbrain hindbrain boundary, hb: hindbrain, zli: zona limitans intrathalamica, WT: wild type. This work was done by Cathleen Teh (IMCB, A*STAR, Singapore).

Tg(-8.0*cldnB:lynEGFP*), briefly called LynEGFP, was used as a non-functional membrane-tethered negative control (Haas and Gilmour 2006). The embryos with weak LynEGFP expression in the cerebellum were screened for FCS measurement. Tg(memKR15-16) with insertion site mapped to 5'UTR of *eng1b* brain-specific membrane-tethered KillerRed expression in the midbrain hindbrain boundary and cerebellum was used as a membrane marker (Kondrychyn, Teh et al. 2011). Tg(H2A.F/Z:EGFP), briefly called H2A-EGFP, was used to estimate the size of the nuclei in the cerebellum (Pauls, Geldmacher-Voss et al. 2001).

2.2.3.2. DNA expression vectors

secEGFP RNA, EGFP driven by a secretion domain, was a gift from Prof. Karuna Sampath (Department of Biological Science, National University of Singapore, Singapore). It was injected into 1-2 cell stage zebrafish embryos and transient secEGFP in the brain ventricle was detected from 22 hpf.

2.2.3.3. Fish maintenance and embryo mounting

Transgenic adult zebrafish and embryos were obtained from the fish facility of the Institute of Molecular and Cell Biology and staged as described (Kimmel, Ballard et al. 1995) in hours post fertilization (hpf). A pair of zebrafish of interest (Wild Type or Transgenic Line) was crossed (male and female were put together in a single tank) and embryos were collected the next morning. Embryos were kept in egg water (60 µg/ml stock salts solution) in a 28.5 °C incubator for optimal development and PTU (0.003% 1-phenyl-2-thiourea in 10% Hank's saline, Invitrogen) was added after 20 hpf (hours post fertilization) and before 30 hpf to prevent pigmentation. Embryos at the stage of interest (24-48 hpf) were dechorionated and then anaesthetized by Tricaine (ethyl m-aminobenzoate, Sigma). The treated embryos were mounted in 1%

low melting temperature agarose (Invitrogen, Singapore) in a No. 1.5 cover glass bottom Petri dish (MatTek, USA) for subsequent measurements. Different orientations (eg. dorsal view or lateral view) of the embryos can be adjusted with needle.

2.2.3.4. Drug treatment

The impact of Wnt inhibitors on brain patterning were tracked by confocal imaging and FCS analysis. Embryos at 100% epiboly were exposed to 1% DMSO (control); C59 (0.1 μ M; 0.5 μ M; 5 μ M) or IWR1 (0.5 μ M; 5 μ M; 50 μ M). Experiments were carried out in 12-well plates (Falcon BD Biosciences, USA) with 20 embryos and 1.5 ml of respective solutions per well. All working concentrations of Wnt inhibitors are dissolved in 1% DMSO. Embryos were incubated in above stated range of solutions until FCS imaging at 28 hpf.

2.2.3.5. Microscopy and imaging analysis

The *in vivo* fluorescent images were acquired with an upright (Zeiss Axiovert 200M) laser scanning microscope (LSM) Meta 510 (Carl Zeiss) equipped with a 40x numerical aperture (NA) 0.75W Achromat long working distance dipping objective and three laser lines (30 mW, 458/477/488/514 nm Argon, 1 mW 543 nm and 5 mW 633 nm). All imaging was performed at room temperature (24 °C). The photomicrographs were taken with AxioCam HRC digital camera (Carl Zeiss Vision, Germany). A series of z scanning images of the cerebellum was taken by confocal microscope. 3D projections of these confocal images were then reconstructed in Imaris (Bitplane AG, Zurich, Switzerland).

In imaging X-scanning analysis (in Section 5.2.3), fluorescent images were acquired with Olympus FV 300 confocal microscope (Olympus, Tokyo, Japan) equipped with

a water-immersion objective (60 \times , NA 1.2; Olympus, Tokyo, Japan). Excitation was provided by the 488-nm laser line of an Argon ion laser. All imaging was performed at room temperature (24 °C). ImageJ was used to generate intensity profile from the cerebellum boundary cell to the brain ventricle. For membrane located Wnt3EGFP and LynEGFP experiments, data was normalized and aligned to the highest intensity point. For secEGFP experiments, a membrane marker, KillerRed, was used for the alignment and the data was normalized to the average intensity in the brain ventricle. The plot presented in Chapter 5 was the average value from three embryos.

Chapter 3

Bayesian Approach to the Analysis of FCS Data

3.1. Introduction

Model selection is of great importance in FCS, since FCS data is fitted with theoretical models to extract the characteristic parameters describing the underlying processes. Commonly FCS data fitting is achieved by least-squares fits of various possible pre-determined models. Model selection is then based on reduced χ^2 values obtained by each model (Meseth, Wohland et al. 1999; Meacci, Ries et al. 2006). Improved model selection can be achieved by maximum likelihood estimation (MLE, Eggeling, Berger et al. 2001; Enderlein, Gregor et al. 2005). However, this tends to over fit the data (Posada and Buckley 2004; Sivia and Skilling 2006; Gregory 2005). The recently proposed Bayesian approach in FCS data analysis provides a novel way for the data evaluation and model selection (He, Guo et al. 2012; Guo, He et al. 2012). This method is based on Bayesian inference, which is originally developed and applied in the social science (Raftery 1995). It was later applied in data analysis in fluorescence based techniques, such as single-particle tracking (McHale, Berglund et al. 2004; Monnier, Guo et al. 2012), single-molecule fluorescence resonance energy transfer (FRET) (Bronson, Fei et al. 2009) and super-resolution imaging (Cox, Rosten et al. 2012). In FCS data analysis, the Bayesian model selection procedure is able to penalize the model complexity appropriately and prevent over-fitting. Moreover, the noise embedded in the data is also estimated and taken into consideration during the model evaluation process.

In this chapter, the Bayesian approach in the analysis of FCS data will be introduced in the following sections on the model probability calculation, the principle of Bayesian inference, the Bayesian model selection as well as the noise estimation. These Bayesian model selection theories and programming code for the analysis of FCS data are developed and provided by my collaborators Mark Bathe and Syuan-Ming Guo. Last but not least, its capability in evaluating the experimental data will be demonstrated.

3.2. Bayesian model selection

3.2.1. Model probability

Assume a data set with n points, $\mathbf{y} = \{y_1, y_2, \dots, y_n\}$ and $\mathbf{x} = \{x_1, x_2, \dots, x_n\}$. This data set is then fitted to a model $\mathbf{f}(\mathbf{x}, \boldsymbol{\beta}) = [f(x_1, \boldsymbol{\beta}), f(x_2, \boldsymbol{\beta}), \dots, f(x_n, \boldsymbol{\beta})]$, where $\boldsymbol{\beta} = \{\beta_1, \beta_2, \dots, \beta_m\}$ and m is the number of model parameters. Each data point is assumed to have an error, ε_i , which is independent and normally distributed around zero (Seber and Wild 1989). Thereby $y_i = f(x_i, \boldsymbol{\beta}) + \varepsilon_i$. The probability distribution of each data point is then defined as:

$$p(y_i|\boldsymbol{\beta}) = (1/(\sigma_i(2\pi)^{1/2}))\exp\{-([y_i - f(x_i, \boldsymbol{\beta})]^2)/(2\sigma_i^2)\} \quad (3.1)$$

where σ_i is the standard deviation of each data point. For a data set consisting of n independent individual measurements, the total probability is given by:

$$\begin{aligned} P(\mathbf{y}|\boldsymbol{\beta}) &= \prod_{i=1}^n p(y_i|\boldsymbol{\beta}) \\ &= \frac{1}{(2\pi)^{n/2} \prod_{i=1}^n \sigma_i} \exp\left\{-\sum_{i=1}^n \frac{[y_i - f(x_i, \boldsymbol{\beta})]^2}{2\sigma_i^2}\right\} \quad (3.2) \end{aligned}$$

For a FCS data set with temporal autocorrelation functions (ACFs), $\mathbf{y} = \{G(\tau_1), G(\tau_2), \dots, G(\tau_n)\}$ and $\mathbf{x} = \{\tau_1, \tau_2, \dots, \tau_n\}$. When the data set consists of a large number of repeats, the noise is normally distributed and thus this is justified by the central

limit theorem. However, this is not always the case. Considering the correlated noise embedded in FCS data (Koppel 1974; Schäzel and Peters 1991), the general multivariate Gaussian function is used instead and Eq. 3.2 is revised as (Seber and Wild 1989; Sivia and Skilling 2006):

$$P(\mathbf{y}|\boldsymbol{\beta}) = \frac{1}{(2\pi)^{n/2}\sqrt{\det(\mathbf{C})}} \exp\left\{-\frac{1}{2}[\mathbf{y} - \mathbf{f}(\mathbf{x}, \boldsymbol{\beta})]^T \mathbf{C}^{-1}[\mathbf{y} - \mathbf{f}(\mathbf{x}, \boldsymbol{\beta})]\right\} \quad (3.3)$$

where \mathbf{C} is the covariance matrix of the error terms. In the case of independent errors, all off-diagonal terms in \mathbf{C} become zero and this expression reduces to Eq. 3.2. The estimation of this term in the case of correlated noise will be discussed in Section 3.2.4.. In conventional data regression, MLE is employed to calculate a point estimate of the model parameters to maximize this probability:

$$\hat{\boldsymbol{\beta}}_{MLE} = \arg \max_{\boldsymbol{\beta}} [P(\mathbf{y}|\boldsymbol{\beta})] \quad (3.4)$$

where $\hat{\boldsymbol{\beta}}_{MLE}$ is the maximum likelihood estimation of the model parameters for the observed data \mathbf{y} . This process is equivalent to the minimization of the sum of the squared errors, $\chi^2(\mathbf{y}, \boldsymbol{\beta}) = \sum_{i=1}^2 ([y_i - f(x_i, \boldsymbol{\beta})]^2)/(\sigma_i^2)$, which is used in calculating the goodness-of-fit. However, these methods tend to favor complex models and thus result in over-fitting. The reason is that they only pursue the maximum or minimum net results but cannot penalize model complexity adequately (Sivia and Skilling 2006; Gregory 2005). Moreover, the reduced χ^2 can only support pairwise comparisons. Given several possible models to be compared, it will be more efficient to rank them by their relative probabilities instead of comparing two by two.

3.2.2. Bayesian inference

Bayesian inference was introduced in 1700s (Dempster 1968). In statistics, it is used to calculate the conditional probability or posterior probability according to Bayes's theorem (also known as Bayes' rule). Assume $P(A)$ refers to the probability that event

A happens or is true, then $P(A|B)$ refers to the probability that event A happens, given that event B happens. It is the probability of both A and B happening $P(A \cap B)$, as a proportion of the probability that B happens $P(B)$:

$$P(A|B) = \frac{P(A \cap B)}{P(B)} \quad (3.5)$$

which can be rewritten as $P(A \cap B) = P(A|B)P(B)$. Likewise, $P(B \cap A) = P(B|A)P(A)$. Since $P(A \cap B)$ and $P(B \cap A)$ are the same, the two equations can be combined and rewritten as such:

$$P(A|B) = \frac{P(B|A)P(A)}{P(B)} \quad (3.6)$$

This is the conditional probability or the posterior probability. It is the probability of A given B. This equation can be seen in this way: $P(A)$ is the prior probability; $P(B|A)$ is the probability of observing B given A, as a function of B with A fixed, this is the likelihood; $P(B)$ is the marginal likelihood and is the same for all possible hypotheses being considered. In other words, the posterior probability is proportional to the prior multiplied by the likelihood. It should be noted that that $P(A|B)$ and $P(B|A)$ are not the same, unless $P(A) = P(B)$.

3.2.3. Bayesian model probability

Applying Bayesian inference in model probability, the model k probability given the observed data \mathbf{y} , $P(M_k|\mathbf{y})$, is given by the Bayes' theorem (from Eq. 3.6):

$$P(M_k|\mathbf{y}) = \frac{P(\mathbf{y}|M_k)P(M_k)}{P(\mathbf{y})} \propto P(\mathbf{y}|M_k) \quad (3.7)$$

where $P(\mathbf{y}|M_k)$ is the conditional probability of the data, $P(M_k)$ is the prior probability of model k . Without preference for any model, the prior probabilities of all the models are equal to be $1/k$. $P(\mathbf{y})$ is the marginal likelihood of the data observation under all possible models. It is the same for every model probability and in Eq. 3.7, it

functions as a normalization factor. Therefore, only $P(\mathbf{y}|M_k)$ is a variable. It is obtained by integrating over parameter space $P(\mathbf{y}|M_k) = \int_{\beta} P(\mathbf{y}|\beta, M_k)P(\beta|M_k)d\beta$.

It is evaluated analytically using the Laplace approximation:

$$P(\mathbf{y}|M_k) = (2\pi)^{p/2} |\Sigma_{Bayes}|^{1/2} P(\mathbf{y}|\hat{\beta}_{Bayes}, M_k) P(\hat{\beta}_{Bayes}|M_k) \quad (3.8)$$

where $\hat{\beta}_{Bayes}$ is the maximum posterior distribution of parameters $P(\beta|\mathbf{y}, M_k)$, and Σ_{Bayes} is the covariance matrix of β estimated at $\hat{\beta}_{Bayes}$. Once $P(\mathbf{y}|M_k)$ is computed, model probabilities can be calculated using Eq. 3.7.

3.2.4. Noise estimation

The next important process is the proper estimation of the noise and the noise correlation in the ACFs for the calculation of $P(\mathbf{y}|\beta)$. Two approaches to estimate the covariance matrix \mathbf{C} in Eq. 3.3 will be introduced for different types of FCS data.

3.2.4.1. Noise estimation from multiple ACFs

Given multiple independent ACF replica, \mathbf{C} is estimated by calculating the sample covariance matrix \mathbf{S} using all ACF curves. The matrix elements S_{kl} are given by:

$$S_{kl} = \frac{1}{J-1} \sum_{j=1}^J \left(G^{(j)}(\tau_k) - \bar{G}(\tau_k) \right) \left(G^{(j)}(\tau_l) - \bar{G}(\tau_l) \right) \quad (3.9)$$

where J is the total number of ACF curves. $G^{(j)}(\tau)$ is an individual curve j . $\bar{G}(\tau_l)$ is the mean curve of l individual curves. The covariance of $\bar{G}(\tau_l)$ from the average of J individual curves is given by $\mathbf{S}_m = (1/J)\mathbf{S}$. However, this estimation method requires large sample size and all the repeats should be from the same physical process. Moreover, the variation across curves should be from only the intrinsic statistical error due to the finite sample size.

3.2.4.2. Noise estimation from a single photon-count trace

In most applications of FCS either *in vitro* or *in vivo*, it will be more convenient to evaluate model probabilities directly from a single trace compared to large number of repeats. In this case, the raw photon-count trace or photon arrival time (PAT) information is required. Thereby the noise estimation can be calculated from the underlying photon-count products via an alternative approach (Schäzel and Peters 1991; Wohland, Rigler et al. 2001).

Generally for the multitau correlator, assume the sampling time or channel width is $\Delta\tau_i$, acquisition time is T_{aq} , so the ACF for a photon-count trace is calculated as shown below:

$$G(\tau_k) = G(k\Delta\tau_i) = \frac{1}{M} \frac{\sum_{m=1}^M \delta n_m \delta n_{m+k}}{\bar{n}_0 \bar{n}_k} \quad (3.10)$$

with

$$\bar{n}_j = \frac{1}{M} \sum_{m=1}^M n_{m+j} \quad (3.11)$$

where n_m is the photon count at $m\Delta\tau_i$, $\delta n_m = n_m - \bar{n}_0$ and $\delta n_{m+k} = n_{m+k} - \bar{n}_k$. $M = T_{aq}/\Delta\tau_i - k$, is the number of possible products $\delta n_m \delta n_{m+k}$. According to Eq. 3.10, the covariance of $G(\tau_k)$ and $G(\tau_l)$ may be calculated from the underlying photon-count products. However, it has been shown that the photon-count products are correlated by a fourth-order correlation function (Starchev, Ricka et al. 2001; Saffarian and Elson 2003). In this case, a procedure based on block-transformations was introduced to obtain independent samples (Flyvbjerg and Petersen 1989).

Defining $p_m(k) = (\delta n_m \delta n_{m+k})/(\bar{n}_0 \bar{n}_k)$, Eq 3.10 becomes:

$$G(k\Delta\tau_i) = \frac{1}{M} \sum_{m=1}^M p_m(k) \quad (3.12)$$

For each block time t_b , the block-transformed sample $p'_m(k)$ is given by the block-average of all $p_m(k)$ within t_b :

$$p'_m(k) = \frac{1}{v} [p_{(m-1)v+1}(k) + p_{(m-1)v+2}(k) + \dots + p_{mv}(k)] \quad (3.13)$$

where $v = t_b/\Delta\tau_i$ is the number of samples in the block. Since the correlations between the photon-count decay over time, the covariance between transformed samples decreases as t_b increases. $t_{b,min}$ is the minimal averaging time, beyond which the transformed samples of the photon-count products are no longer correlated. Once the minimal t_b is determined, the transformed samples can be calculated according to Eq. 3.13 and then used to calculate the matrix elements S_{kl} in the sample covariance matrix \mathbf{S} of $G(\tau)$:

$$S_{kl} = \frac{1}{M'(M' - 1)} \sum_{m=1}^{M'} (p'_m(k) - \bar{p}'(k))(p'_m(l) - \bar{p}'(l)) \quad (3.14)$$

where M' is the number of transformed samples. It should be noticed that $t_{b,min}$ depends on both the characteristic correlation time of the underlying physical process and its functional form. In practice, $t_{b,min}$ can be determined by finding the minimal time after which S_{kk} becomes invariant to t_b in $S_{kk} - t_b$ plot (Flyvbjerg and Petersen, 1989; Frenkel and Smit, 2002). An example will be shown in Section 3.3.1.

3.3. Results

The capability of this approach in the analysis of stimulated data under various conditions has been demonstrated in details in the recent publications (He, Guo et al. 2012; Guo, He et al. 2012). Hence, in this work, only the experimental work will be shown. The recorded data was provided as photon arrival times (PAT) and thus the noise was estimated based on the second approach introduced in Section 3.2.4.2.

3.3.1. Distinguishing fast photo dynamic processes

When excited by a high laser intensity, a triplet state of the fluorophore can be populated. This photo dynamical process can be detected and characterized by FCS (Widengren, Mets et al. 1999). Here, Fluorescein, which is known to have a high probability of triplet state excitation, was analyzed. The excitation laser intensity varied from 2 to 20 kW/cm². The model probabilities were determined as follows.

After recording the data in terms of photon arrival times (PAT, see Section 2.1.5), the PAT files are read and a blocking transformation is first performed to get the minimum block time $t_{b,min}$. The estimated noise level σ is plotted as a function of block time t_b in Fig. 3.1A. As the block-size t_b increases, σ increases. This is due to the correlated noise in the samples. Assuming the diffusion time of Fluorescein under such experimental conditions is τ_D , which is the time the fluorophore takes to pass through the observation volume. When $t_b \ll \tau_D$, the increase rate is small, since the fluctuations on this time scale is from the uncorrelated photon counting noise. When $t_b \sim \tau_D$, the increase rate of the noise is high, since the noise is correlated. In this time scale, the noise comes from the stochastic nature of the observed fundamental processes, i.e., diffusion, chemical reaction, or photo-decomposition (Koppel 1974). Finally, when $t_b \gg \tau_D$, the transformed photon-count products become independent and the estimated noise level is no longer increased by the increased t_b . It is also shown that the statistical error (error bar in Fig. 3.1A) in the estimated noise increases with increasing t_b . This is due to the reduced sample number at large t_b . The optimal block-time $t_{b,min}$ (fixed point, Fig. 3.1A) is determined as first point at which the estimated noise is independent of increased t_b . After $t_{b,min}$ is determined, the transformed photon-counts data is calculated using Eq. 3.13 and the covariance matrix

was estimated using Eq. 3.14. Then, the model probabilities were calculated using Eq. 3.7 and 3.8.

The fitting is plotted in Fig. 3.1B and the results are plotted as a function of increased excitation intensity in Fig. 3.2. There were 10 PAT traces for each condition. Evaluated models are 3-dimensional (3D) one-component diffusion (1p, Eq. 2.9), one-component diffusion with a triplet state (1p1t, Eq. 2.18), one-component diffusion with two triplet state (1p2t, Eq. 2.24) and two-component diffusion (2p, Eq. 2.15). As the excitation intensity increases, the fraction of Fluorescein in the triplet state increases. At low excitation intensity, the Bayesian approach prefers the 1p model, since the fraction of Fluorescein in the triplet state is low. As the excitation intensity increases, the 1p1t model is eventually preferred. This is not only due to the increased fraction of triplet state which can be easily resolved but also the increased signal-to-noise ratio. The over-fitted 1p2t model and physically implausible 2p model are never preferred.

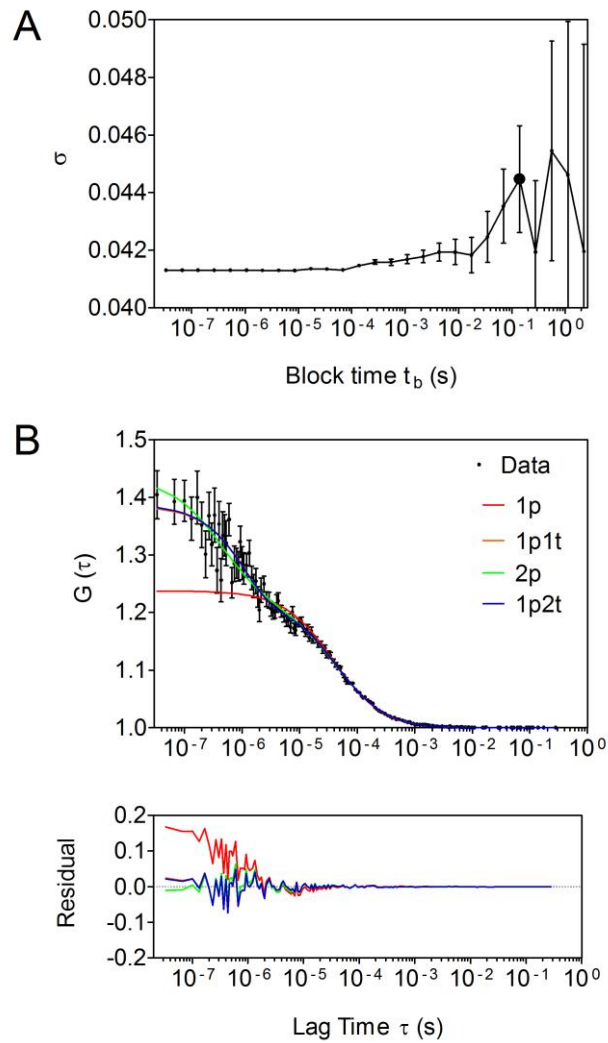


Figure 3.1 Blocking transformation and fitting to evaluated models

(A) Estimated noise level as a function of block-time t_b for 10 nM Fluorescein at 10 kW/cm^2 with acquisition time of 40 s. The fixed point is $t_{b,min}$ of approximately 139 ms. Error bars: SD (B) Fitting of evaluated models to ACF of Fluorescein calculated from photon arrival time (PAT) trace. Evaluated models are 3D one-component diffusion (1p, red), one-component diffusion with a triplet state (1p1t, orange), two-component diffusion (2p, green) and one-component diffusion with two triplet state (1p2t, purple).

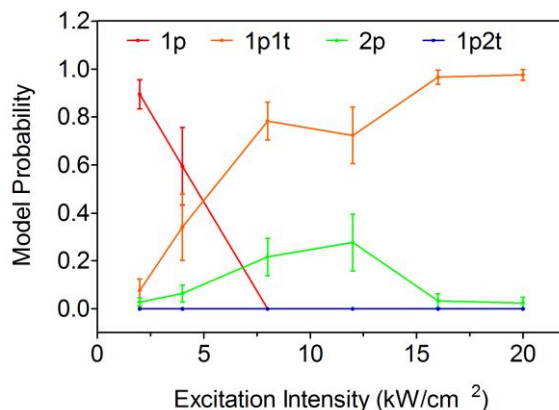


Figure 3.2 Bayesian analysis of Fluorescein with varying excitation intensity

Model probabilities are plotted with increased excitation intensity. Evaluated models are 3D one-component diffusion (1p, red), one-component diffusion with a triplet state (1p1t, orange), two-component diffusion (2p, green) and one-component diffusion with two triplet state (1p2t, purple). Error bars: SEM.

3.3.2. Distinguishing the two diffusion components

FCS is of great help to determine the molecular mobility. The diffusion coefficient can be calculated from the diffusion time extracted from the fit. Therefore, the capability of this procedure to distinguish multiple diffusing species was examined. Measurements were performed using mixtures of Atto565 and Atto565-labeled streptavidin. The mixing concentration ratio is defined as R , $R = [\text{Atto565-streptavidin}] / [\text{Atto565}]$, ranging from 0.025 to 40. There were 8 PATs for each concentration ratio. Evaluated models are 3D one-component diffusion with a triplet state (1p1t, Eq. 2.18), two-component diffusion with a triplet state (2p1t, Eq. 2.21) and three-component diffusion with a triplet state (3p1t, Eq. 2.23). The triplet blinking time was fixed at 4 μs , which is determined from pure Atto565 under the same experimental conditions.

The model probabilities are plotted with the increased R in Fig. 3.3, together with pure Atto565 (first point, on the left) and pure Atto565-streptavidin (last point, on the right). As the concentration of Atto565 decreases, the model probability transitions

from the 1p model to the 2p model. The 2p model was still dominant for the ratios higher than 20. This is due to the residual free Atto565 in the pure Atto565-streptavidin sample, as shown by the evaluation on pure Atto565-streptavidin. The above results demonstrate that this Bayesian model procedure is able to identify the number of components in experimental systems.

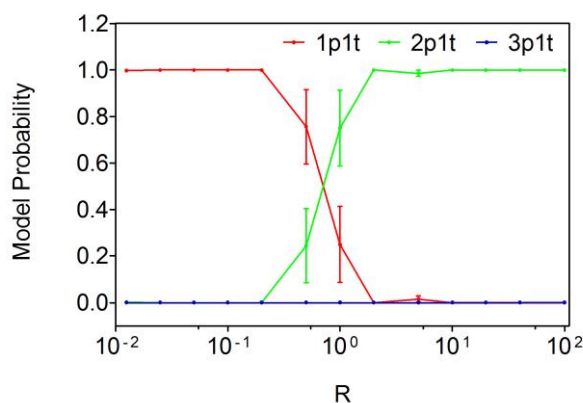


Figure 3.3 Bayesian analysis of mixtures of Atto565 and Atto565-streptavidin with distinct concentration ratios

Model probabilities are plotted with decreased mixing concentration ratio R , $R = [\text{Atto565-streptavidin}] / [\text{Atto565}]$. Each ACF is fitted with models of 3D one-component diffusion with a triplet state (1p1t, red), two-component diffusion with a triplet state (2p1t, green), three-component diffusion with a triplet state (3p1t, blue) with triplet blinking time fixed at 4 μs . Error bars: SEM.

3.4. Conclusion

Bayesian model selection provides an objective evaluation of multiple competing models in FCS. The noise in the data is estimated and considered in this process. Two approaches to the estimation of the correlated noise have been introduced for different types of recorded data. It is able to distinguish fast photo dynamics and multiple diffusing components in the experimental system. Therefore, this approach will be applied in determining the appropriate fitting models for fluorescent proteins both *in vitro* and *in vivo* in the next chapter.

Chapter 4

Bayesian Approach to the Analysis of FCS Data of Fluorescent Proteins

4.1. Introduction

The use of fluorescent proteins in FCS broadens its application in addressing issues in the life sciences. However, the low signal-to-noise ratio caused by the increased background and limited experimental conditions as well as the biological heterogeneity makes model selection ambiguous, especially when the process under study is unclear (Schwille, Korfach et al. 1999; Meacci, Ries et al. 2006; Chen, Rhoades et al. 2007; Abu-Arish, Porcher et al. 2010). It is not uncommon for the researchers to compare several models to find out the best representative. But this process is tedious and time consuming. The capability of Bayesian model selection in evaluating the experimental data has been demonstrated in the previous chapter. Therefore, it is of great practical meaning to apply this method to determine the appropriate fitting models for widely used fluorescent proteins both *in vitro* and *in vivo*.

In this chapter, three organic dyes, Atto488, Fluorescein and Rhodamine 6G, are firstly used to examine its ability in model selection under various experimental conditions, including excitation intensity, acquisition time and experiment

temperature. Afterwards, the same methodology will be employed to determine the appropriate fitting models for widely used fluorescent proteins namely EGFP, EYFP and mCherry in solution under different experimental conditions. This approach will be adopted for fluorescent proteins in CHO cells. The fitting models for measurements in cytoplasm, nucleus and membrane will be determined. Finally, the fitting models for EGFP labeled signaling proteins measured in living zebrafish embryos will be analyzed.

4.2. Results

4.2.1. Organic dyes

Firstly, organic dyes, Atto488, Fluorescein and Rhodamine 6G were used to validate the model selection approach under various experimental conditions. As shown in the previous chapter, the data quality or the signal-to-noise ratio has an influence on the model selection for Fluorescein. It has been pointed out that the signal-to-noise ratio depends both on the fluorophore brightness and on the acquisition time (Koppel 1974). The brightness is measured in fluorescence counts per particle per second (cps) and can be increased by increasing the excitation intensity. Therefore, the effect on model selection by excitation intensity and acquisition time will be examined in this section.

4.2.1.1. Excitation intensity

As can be seen from Fig. 4.1A to C, ACFs become smoother as the excitation intensity increases. The brightness (η) was calculated as the mean fluorescence intensity divided by the average number of particles inferred from fitting (Eq. 2.26). The results are plotted in Fig. 4.1D. With increasing excitation intensity, the brightness increases linearly at low excitation intensity, below 8 kW/cm^2 . Then the increase rate slows down as the fluorophores encounter saturations. In this case, the

detection volume is no longer the assumed Gaussian distribution oval shape but flattened in the center (Hess and Webb 2002; Nagy, Wu et al. 2005). This results in a larger observation volume and thus an overestimated number of particles and decreased brightness increase rate. In such a situation, the apparent diffusion time inferred from fitting is larger (Fig. 4.3A). Saturation occurs when the excitation intensity is so strong that most of the fluorophores in the observation volume are in the excited state or triplet state rather than in the ground state. Therefore, the emission is not proportional to the excitation anymore and thus distorting the observational volume. Another possible reason of the saturation can be a population of fluorophores in non-fluorescent state due to the photo-isomerization (Enderlein, Gregor et al. 2004). Therefore, it depends on the property of the fluorophores. With a high fraction of triplet, the brightness of Fluorescein reaches a plateau then drops, as shown in Fig. 4.1D.

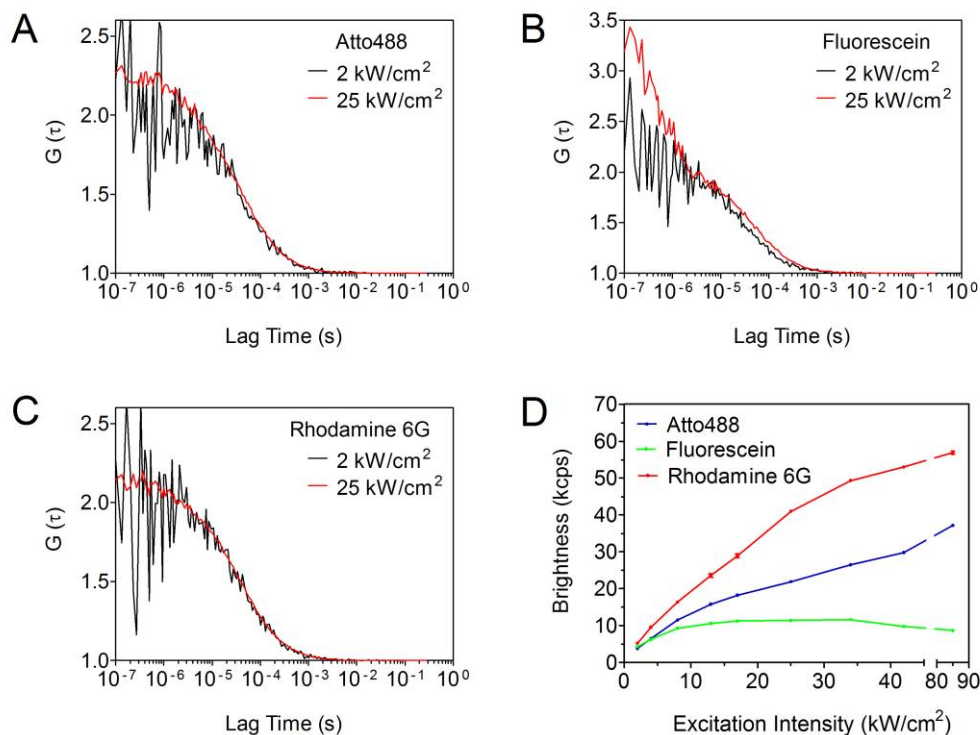


Figure 4.1 ACFs calculated from PAT traces of organic dyes and their brightness

ACFs under low and high excitation intensities of organic dyes: (A) Atto488, (B) Fluorescein, and (C) Rhodamine 6G in 1x PBS and (D) their brightness: Atto488 (blue), Fluorescein (green) and Rhodamine 6G (red). Error bars: SEM.

The influence of excitation intensity on the model selection was then examined using the Bayesian approach. Evaluated models were 3-dimensional (3D) one-component diffusion (1p, Eq. 2.9), one-component diffusion with a triplet state (1p1t, Eq. 2.18), two-component diffusion (2p, Eq. 2.15), two-component diffusion with a triplet state (2p1t, Eq. 2.21) and one-component diffusion with two triplet state (1p2t, Eq. 2.24). The model probabilities are plotted with the increase in the excitation intensity in Fig. 4.2A-C and model selection is shown in Fig. 4.2D. Under low excitation intensity, below 4 kW/cm², 1p was preferred. This is because on one hand the fluorophore has a low triplet fraction at this low excitation intensity and on the other hand the signal-to-noise ratio is not sufficiently high to allow the distinction of the triplet state in the μ s range of the ACF. As the excitation intensity increased, the model selection

transitioned from 1p to 1p1t. This trend was the same for all the three tested dyes. However, from 15 kW/cm², the preferred model started to show a competition between 1p1t and 2p for Atto488 and Rhodamine 6G, whereas 1p1t stayed dominant for Fluorescein.

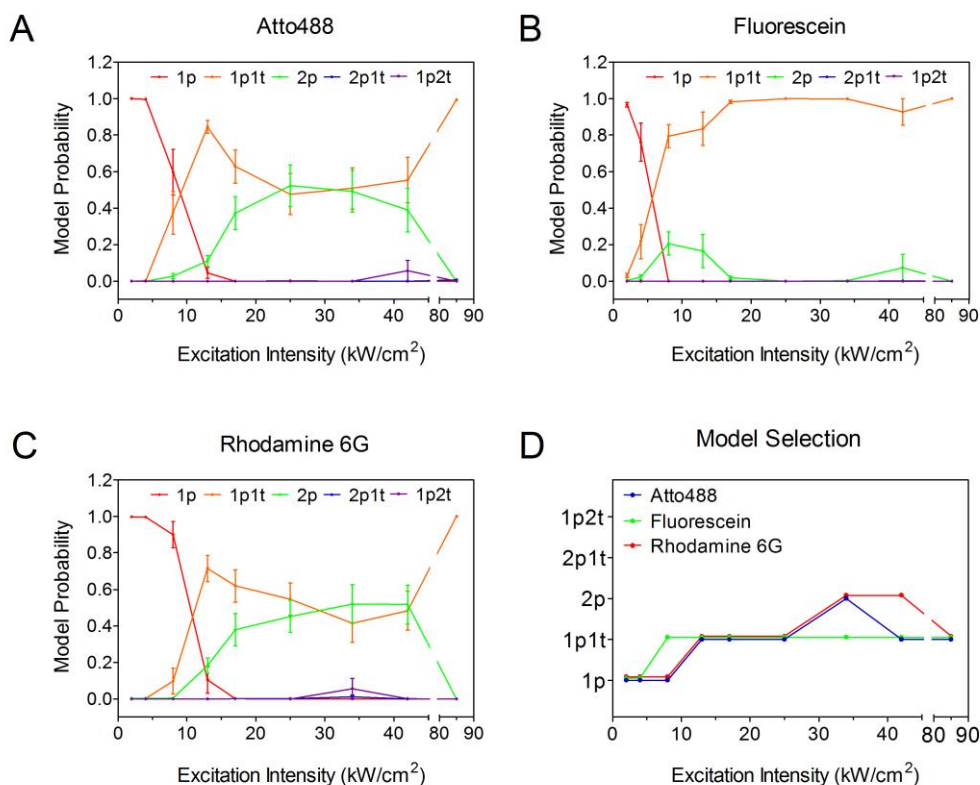


Figure 4.2 Model probabilities and model selection of organic dyes at different excitation intensities

Model probabilities of organic dyes in 1x PBS: (A) Atto488, (B) Fluorescein and (C) Rhodamine 6G and (D) their model selection: Atto488 (blue), Fluorescein (green) and Rhodamine 6G (red). Evaluated models are 3D one-component diffusion (1p, red), one-component diffusion with one triplet (1p1t, orange), two-component diffusion (2p, green), two-component diffusion with one triplet (2p1t, blue), one-component diffusion with two triplet (1p2t, purple). Error bars: SEM.

To figure out what this ‘second component’ is, the fitting parameters - diffusion time (τ_D), triplet time (τ_{trip}) and its fraction (F_{trip}) in 1p1t, and diffusion time of ‘fast moving component’ ($\tau_{D, fast}$) and its fraction ($F_{D, fast}$) in 2p - were inferred and plotted in Fig. 4.3. The results of the three dyes were similar in trend, only differing in values.

Therefore I use Atto488 as an example to illustrate the results. With increasing excitation intensity, the triplet time kept almost constant and the fraction increased as the triplet population increased. It should be noted that the longer triplet relaxation time inferred below 10 kW/cm² is an artifact from the 1p1t model fitting, since the appropriate fitting model is determined to be 1p. It was found that this 2p was unphysical, as its 'fast' moving component has a diffusion time even shorter than the triplet time in 1p1t (Fig. 4.3B). Moreover, the fraction of this 'fast' moving component was higher than the triplet fraction and almost parallel to the triplet fraction, increasing as the excitation intensity increased (Fig. 4.3C). These results indicate that the 2p model is incorrect. It produces similar parameter values to 1p1t but with a nonphysical interpretation of these values.

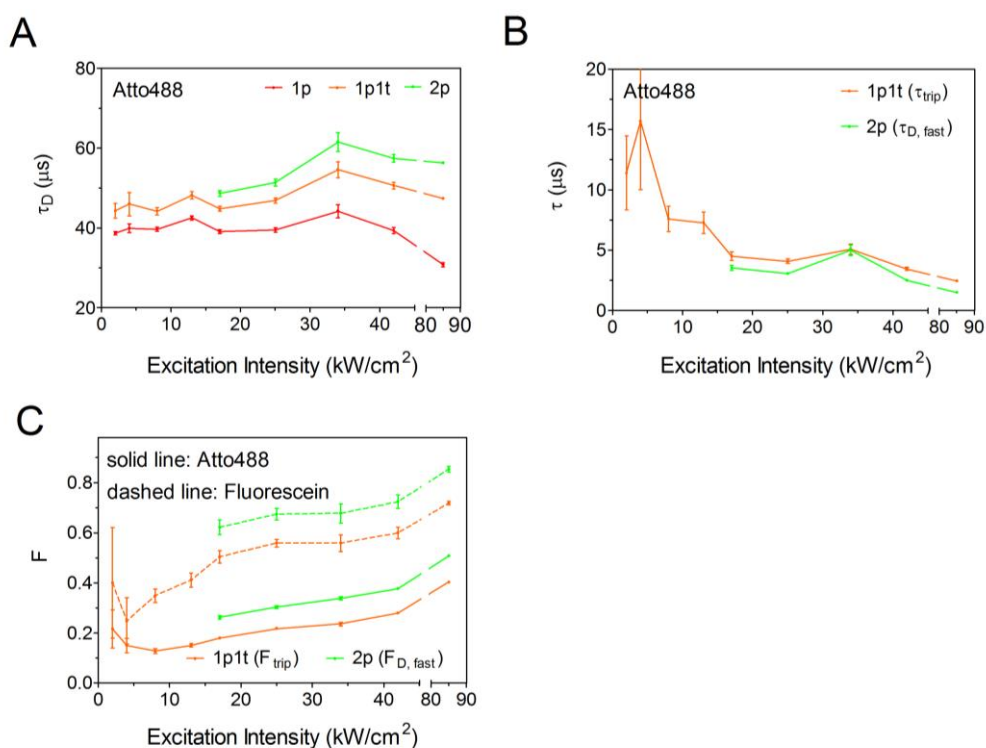


Figure 4.3 Fitting parameters inferred from different fitting models using Atto488

(A) Diffusion time τ_D , (B) 1p1t triplet time (τ_{trip}) and diffusion time of 'fast moving component' in 2p ($\tau_{D,fast}$) and (C) 1p1t triplet fraction (F_{trip}) and 'fast moving component' fraction in 2p ($F_{D,fast}$) were inferred and plotted with increasing excitation intensity. Dashed line: data of Fluorescein for comparison. Evaluated models are 3D one-component diffusion

(1p, red), one-component diffusion with one triplet (1p1t, orange), two-component diffusion (2p, green). Error bars: SEM.

The reason for this is that the assumption of the fitting function is no longer valid under saturation conditions and thus leads to erroneous selection results. The model determined by the calculation process is then only with the maximum model probability but not necessarily physically possible. It has been reported that under such conditions fitting models including 2p and one component anomalous diffusion are better fits with improved residuals (Hess and Webb 2002). Even though the selection is no longer valid, the preference depends on the triplet fraction. With a triplet fraction more than 40% under low excitation intensity, Fluorescein in theory suffered saturation even earlier than the other two fluorophores (Fig. 4.3C, dashed line). However, it is possible that this clear triplet allows the program to distinguish it and thus prefers 1p1t. In accord with this hypothesis, with the increased triplet fraction to more than 25% when the tested excitation intensity was above 42 kW/cm^2 , the model selection of Atto488 was back to 1p1t (Fig. 4.2A and D, Fig. 4.3C, dashed line). The same phenomenon was also observed for Rhodamine 6G (Fig. 4.2C and D). According to Table 2.4, the results are consistent with the reported Rhodamine 6G excitation saturation from $60 \text{ }\mu\text{W}$ in one-photon FCS (Nagy, Wu et al. 2005).

4.2.1.2. Acquisition times

A moderate way to increase the signal-to-noise ratio is via increasing the acquisition time. Moreover, exciting samples with higher intensity to improve the signal-to-noise ratio is not always applicable, especially for fluorophores sensitive to photobleaching. In such cases, increasing the acquisition time will be more helpful. On the other hand, short acquisition times may be necessary for highly dynamic systems. Hence, data with acquisition times of 10, 20, 40, 80 and 120 s under both low excitation intensity,

2 kW/cm², and high excitation intensity (where the competition between 1p1t and 2p happens), 25 kW/cm², were analyzed (Fig. 4.4). Under low excitation intensity, increasing acquisition time barely changes the model selection (Fig. 4.4, circles on solid line), but it improves data quality by increasing the signal-to-noise ratio and thus reduces errors of inferred parameters (Fig. 4.19A). Under high excitation intensity, which potentially saturates the sample, longer measurement times increase the signal-to-noise ratio but lead also to increased probabilities for the incorrect 2p model as expected (Fig. 4.4, squares on dashed line)

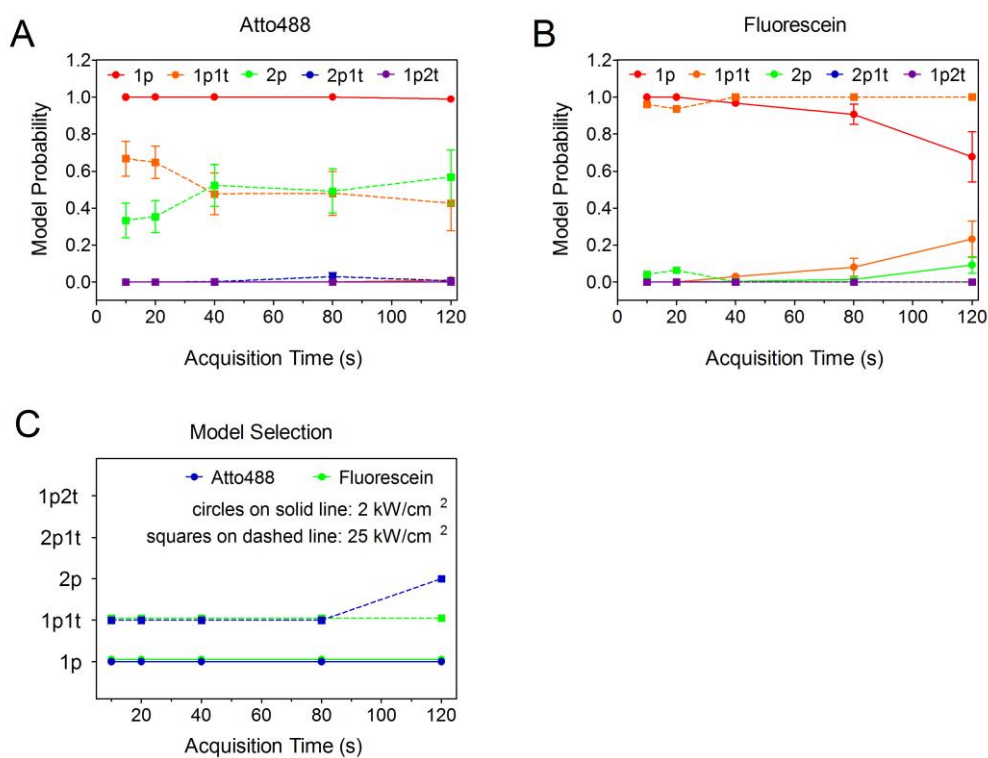


Figure 4.4 Model probabilities and model selection and of organic dyes with different acquisition times

Model probabilities of (A) Atto488 and (B) Fluorescein under low and high excitation intensities with different acquisition times and (C) their model selection: Atto488 (blue) and Fluorescein (green). Evaluated models are 3D one-component diffusion (1p, red), one-component diffusion with one triplet (1p1t, orange), two-component diffusion (2p, green), two-component diffusion with one triplet (2p1t, blue), one-component diffusion with two triplet (1p2t, purple). Error bars: SEM. Circles on solid line: 2 kW/cm²; squares on dashed line: 25 kW/cm².

4.2.2. Fluorescent proteins *in vitro*

With the knowledge above, the Bayesian approach was then applied to widely used fluorescent proteins: EGFP, EYFP and mCherry. The aim in this section is to find out the appropriate fitting model for them in solution under different conditions including excitation intensity and acquisition time.

4.2.2.1. Excitation intensity

Similar to organic dyes, the ACFs become smoother as the excitation intensity increases (Fig. 4.5). It is also shown that the curve is smoother for fluorophores with higher brightness. This can be seen in Fig. 4.5D, where the order of fluorophores in descending brightness is EYFP, EGFP, and mCherry.

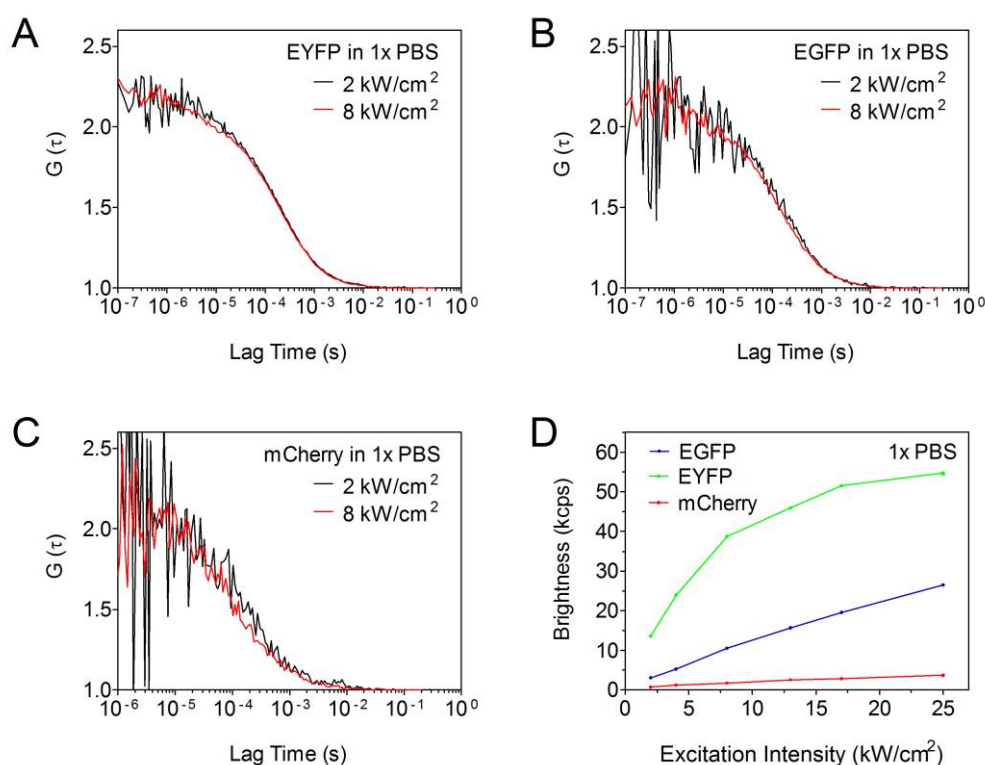


Figure 4.5 ACFs calculated from PAT traces of fluorescent proteins and their brightness

ACFs under low and high excitation intensities of fluorescent proteins: (A) EYFP, (B) EGFP and (C) mCherry in 1x PBS, and (D) their brightness: EGFP (blue), EYFP (green) and mCherry (red). Error bars: SEM.

The evaluated models were the same as for organic dyes. A similar selection is observed, but with the 2p competition dominating at lower excitation intensities than for the organic dyes (Fig. 4.6). The 2p selection was shown at 2 kW/cm² for EYFP and 8 kW/cm² for EGFP. Even though it is selected from 25 kW/cm² for mCherry, the 1p1t dominance for a large range of the excitation intensity should be due to its high fraction of dark state (Fig. 4.6C and D, Fig. 4.7C, dashed line). The monomeric red fluorescent protein (mRFP1) has been shown to be with high fraction dark state (Hillesheim, Chen et al. 2006; Hendrix, Flors et al. 2008). mCherry, the direct evolution of mRFP1, even though shows better photostability, maturation, and tolerance for tagging (Shaner, Campbell et al. 2004; Shaner, Steinbach et al. 2005), is still reported to have about 40% in dark state in one photon FCS (Foo, Naredi-Rainer et al. 2012) and above 70% in a less bright state in two photon FCS (Wu, Chen et al. 2009).

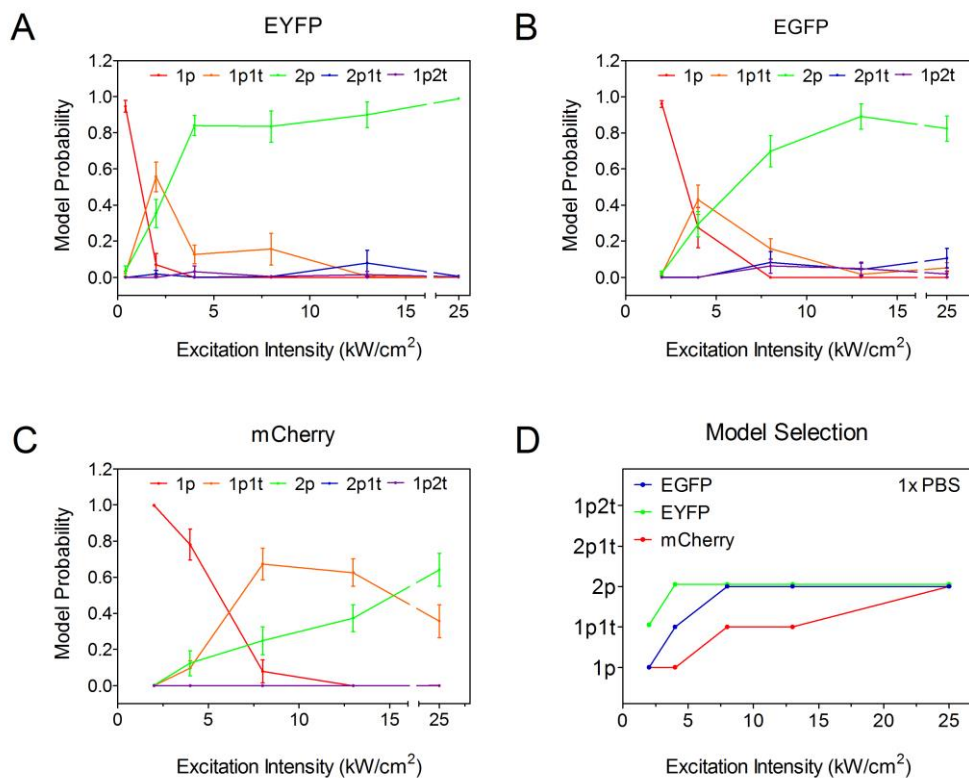


Figure 4.6 Model probabilities and model selection of fluorescent proteins at different excitation intensities

Model probabilities of fluorescent proteins in 1x PBS: (A) EYFP, (B) EGFP and (C) mCherry and (D) their model selection: EGFP (blue), EYFP (green) and mCherry (red). Evaluated models are 3D one-component diffusion (1p, red), one-component diffusion with one triplet (1p1t, orange), two-component diffusion (2p, green), two-component diffusion with one triplet (2p1t, blue), one-component diffusion with two triplet (1p2t, purple). Error bars: SEM.

For all three fluorescent proteins, there exists a fast photophysical process whose relaxation time decreased with increasing excitation intensity and whose fraction remained constant (Fig. 4.7C and D). Therefore, this process is likely to be photo-induced isomerization, in which the isomerization frequency is increased with photon flux (Widengren, Mets et al. 1999; Widengren and Seidel 2000). This blinking process due to isomerization is described by the same equation describing triplet state dynamics in the ACF (see Section 2.1.3). The photo-induced isomerization relaxation frequency is described as τ_{iso} and the fraction of the fluorophores in isomerized dark state is described as F_{iso} . Note that for the fluorescent proteins the diffusion time

decreases with increasing excitation intensity (Fig. 4.7A). This is due to photobleaching as the destruction of the fluorophore reduces the time the molecule is detected and thus reduces the apparent residence time of the molecule in the observation volume. Similar to dyes, the parameter values of 2p are similar to the 1p1t (Fig. 4.7), with the 'fast' moving component corresponding to the isomerization relaxation time and its fraction to the triplet fraction.

It has been reported that there are multiple blinking processes for EGFP and its variant EYFP (Widengren, Mets et al. 1999; Schwille, Kummer et al. 2000; Heikal, Hess et al. 2000). However, it was found that 1p1t is enough to describe the ACFs, and 1p2t was never preferred within the tested excitation intensity, even without 2p in the tested model list. One possible reason is that the excitation intensity is in the lower range compared to the reported study, in which the excitation intensity was beyond 25 kW/cm² (Widengren, Mets et al. 1999). Since the final goal of this study is to determine the appropriate fitting model for the application of fluorescent proteins in biological studies, the excitation intensity is kept in the range below 25 kW/cm². Under the lowest tested excitation intensity, 1p is enough to describe the ACFs for all three fluorescent proteins.

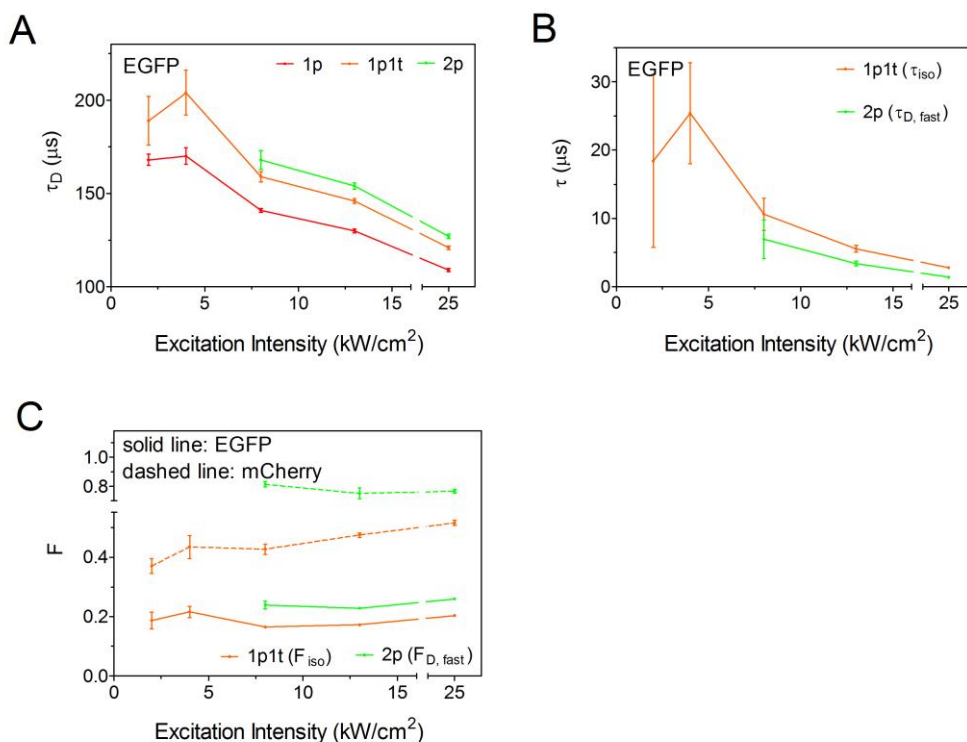


Figure 4.7 Fitting parameters inferred from different fitting models using EGFP

(A) Diffusion time τ_D , (B) 1p1t isomerization relax time (τ_{iso}) and diffusion time of ‘fast moving component’ in 2p ($\tau_{D, fast}$) and (C) 1p1t isomerization fraction (F_{iso}) and ‘fast moving component’ fraction in 2p ($F_{D, fast}$) were inferred and plotted with increasing excitation intensity. Dashed line: data of mCherry for comparison. Evaluated models are 3D one-component diffusion (1p, red), one-component diffusion with one triplet (1p1t, orange), two-component diffusion (2p, green). Error bars: SEM.

4.2.2.2. Acquisition time

Similar to organic dyes, data with acquisition times of 10, 20, 40, 80 and 120 s under both low and high excitation intensities were analyzed. The results are plotted in Fig. 4.8. Under low excitation, longer acquisition time did not change the model selection for EGFP and mCherry (Fig. 4.8, circles on solid line), but only improved data quality (Fig. 4.19B). But in the case of EYFP, a longer acquisition time changed the preferred model to 2p due to saturation. Similarly, under high excitation, longer measurement times increased probabilities for the incorrect 2p model as expected (Fig. 4.8, squares on dashed line). As an exception, mCherry showed a transition from 1p to 1p1t, indicating the improved signal-to-noise ratio. The reason for this is because of its low

brightness (Fig. 4.5D). Therefore, acquisition times as low as 10s can be sufficient for fluorescent proteins with quite a high brightness, but it would be better to take long acquisition times to improve the data quality for fluorescent proteins with low brightness.

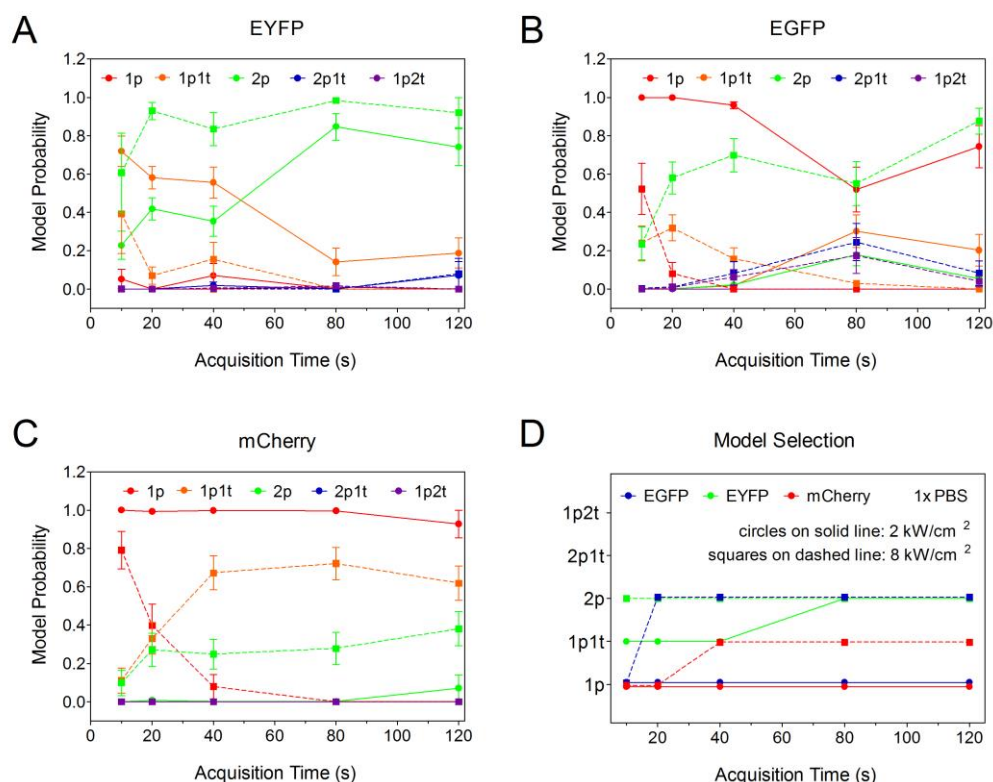


Figure 4.8 Model probabilities and model selection and of fluorescent proteins with different acquisition times

Model probabilities of (A) EYFP, (B) EGFP and (C) mCherry, under low and high excitation intensities with different acquisition times and (D) their model selection: EGFP (blue), EYFP (green) and mCherry (red). Evaluated models are 3D one-component diffusion (1p, red), one-component diffusion with one triplet (1p1t, orange), two-component diffusion (2p, green), two-component diffusion with one triplet (2p1t, blue), one-component diffusion with two triplet (1p2t, purple). Error bars: SEM. Circles on solid line: 2 kW/cm²; squares on dashed line: 25 kW/cm².

4.2.3. Fluorescent proteins *in vivo*

Finally, this approach was applied in the analysis to the fluorescent proteins in commonly used CHO cells. Data analysis in cells generally is more difficult and

ambiguous due to the heterogeneity, such as various organelles in the cell, the membrane fluctuations and different protein expression levels from cell to cell. Furthermore, limitations on experimental conditions, such as low excitation intensity and short acquisition time, render data analysis more challenging. As can be seen from Fig. 4.9, the brightness is lower and the ACFs are noisier than those measured in solution. This is due to the increased background noise from the scattering. Some studies showed different mobility of EGFP in cytoplasm and nucleus (Wachsmuth, Waldeck et al. 2000), whereas other studies showed very close values at different cellular compartments (Chen, Muller et al. 2002). Therefore, measurements were performed both in the cytoplasm and nucleus. However, it was found out that the chosen area has no influence on the model selection (data not shown). The inferred diffusion times of proteins in the cytoplasm and nucleus were close (Table 4.3). Hence, only results from the cytoplasm measurements are shown here.

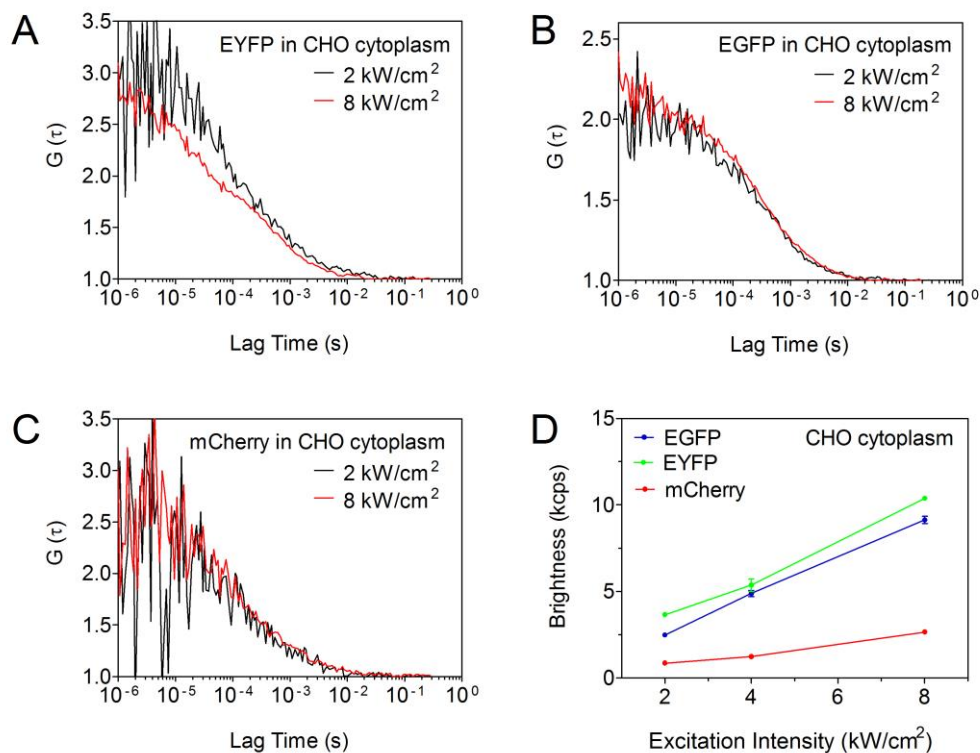


Figure 4.9 ACFs calculated from PAT traces of fluorescent proteins and their brightness in CHO cytoplasm

ACFs under low and high excitation intensities of fluorescent proteins, (A) EYFP, (B) EGFP and (C) mCherry in CHO cytoplasm, and (D) their brightness: EGFP (blue), EYFP (green) and mCherry (red). Error bars: SEM.

4.2.3.1. Excitation intensity

Evaluated models were the same as for measurements in solution. The 1p model was enough to describe the ACFs of the three fluorescent proteins under the lowest tested excitation intensity (Fig. 4.10). Similar to measurements in solution, increasing excitation intensity induces a selection shift to 2p. Due to the environmental change, the isomerization fraction of EYFP increased and thus changed its preference from 2p to 1p1t (Fig 4.10A and D, Fig. 4.11C, dashed line). This is in accord with the Fluorescein results, in which the 1p1t model was kept dominant under high excitation intensity due to its high triplet fraction. However, even though mCherry generally has a high dark state fraction (see Section 4.2.2.1), 2p still dominates the model selection.

This is due to its low brightness, which makes the dark fraction not easy to be distinguished (Fig. 4.9C). The 2p model in cells is still the same as in solution, that is, unphysical and incorrect but only produces similar inferred parameter values to 1p1t (Fig. 4.11).

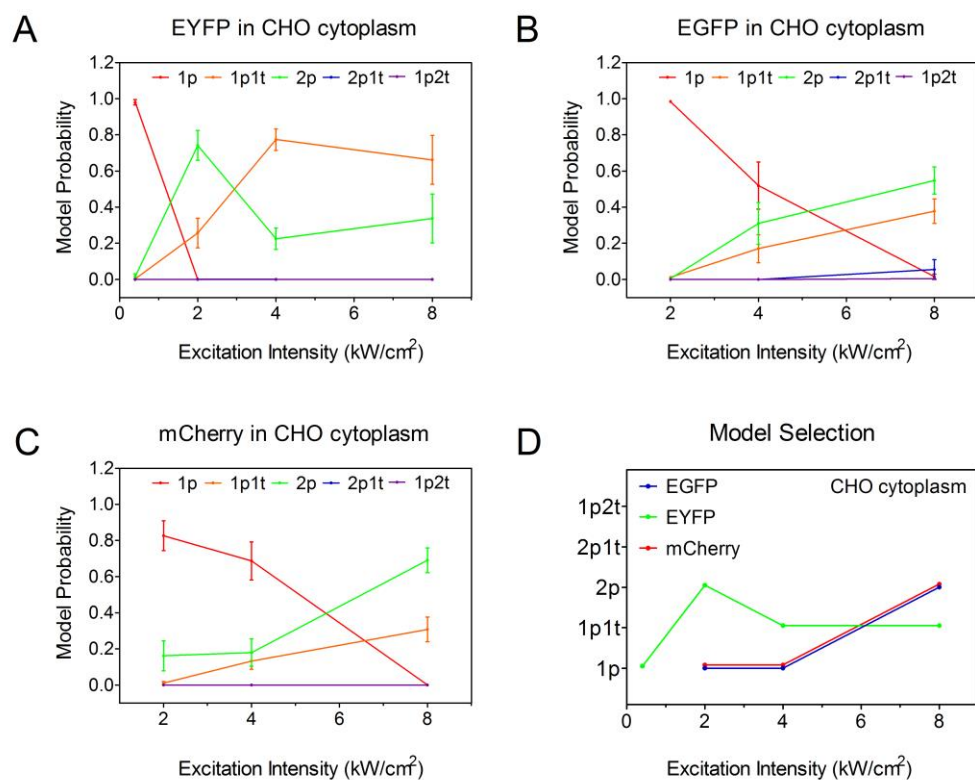


Figure 4.10 Model probabilities and model selection of fluorescent proteins in CHO cytoplasm at different excitation intensities

Model probabilities of fluorescent proteins in CHO cytoplasm: (A) EYFP, (B) EGFP and (C) mCherry and (D) their model selection: EGFP (blue), EYFP (green) and mCherry (red). Evaluated models are 3D one-component diffusion (1p, red), one-component diffusion with one triplet (1p1t, orange), two-component diffusion (2p, green), two-component diffusion with one triplet (2p1t, blue), one-component diffusion with two triplet (1p2t, purple). Error bars: SEM.

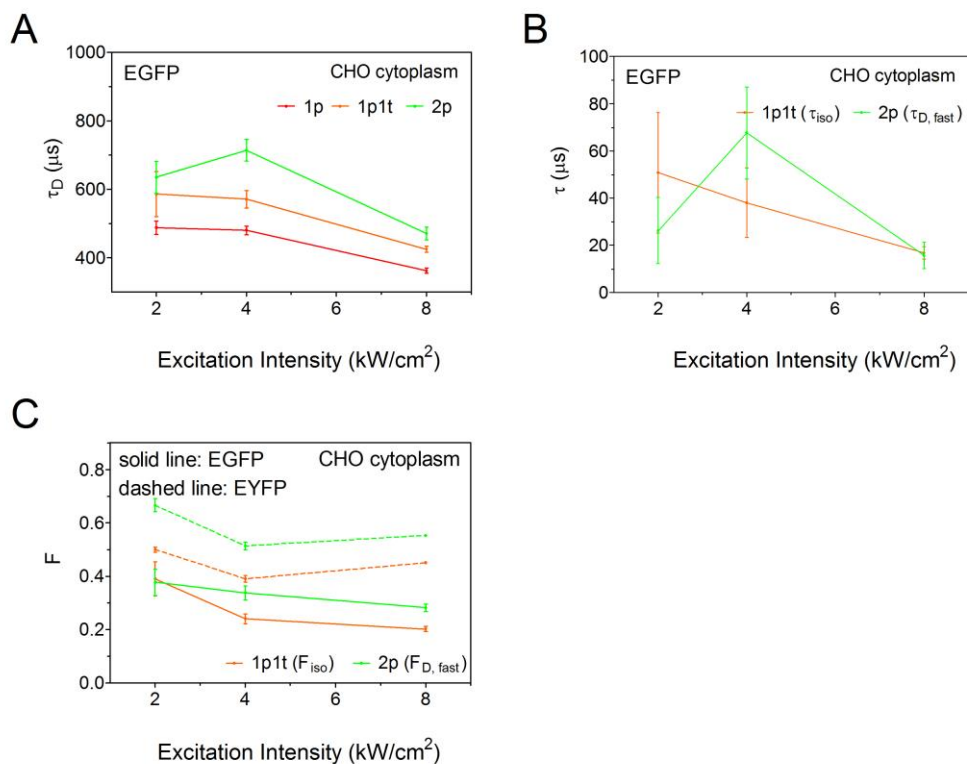


Figure 4.11 Fitting parameters inferred from different fitting models using EGFP measured in CHO cytoplasm

(A) Diffusion time τ_D , (B) 1p1t isomerization relax time (τ_{iso}) and diffusion time of ‘fast moving component’ in 2p ($\tau_{\text{D,fast}}$) and (C) 1p1t isomerization fraction (F_{iso}) and ‘fast moving component’ fraction in 2p ($F_{\text{D,fast}}$) were inferred and plotted with increasing excitation intensity. Dashed line: data of EYFP for comparison. Evaluated models are 3D one-component diffusion (1p, red), one-component diffusion with one triplet (1p1t, orange), two-component diffusion (2p, green). Error bars: SEM.

4.2.3.2. Acquisition time

In cells, the acquisition time cannot be as long as in solution due to photobleaching and phototoxicity, especially at high laser excitation intensities due to the finite and relatively small cellular volume. Therefore, data with acquisition times of 5, 10 and 20 s under both low and high excitation intensities were analyzed (Fig. 4.12). Acquisition time barely changed the model selection for EYFP and mCherry at both excitation intensities. Unlike in solution, even 20 s changed the EGFP model to the implausible 2p model at 2 kW/cm^2 . Thus, it appears that 8 kW/cm^2 is too strong for

the fluorescent proteins in cells, since 2p dominates even with the shortest acquisition time.

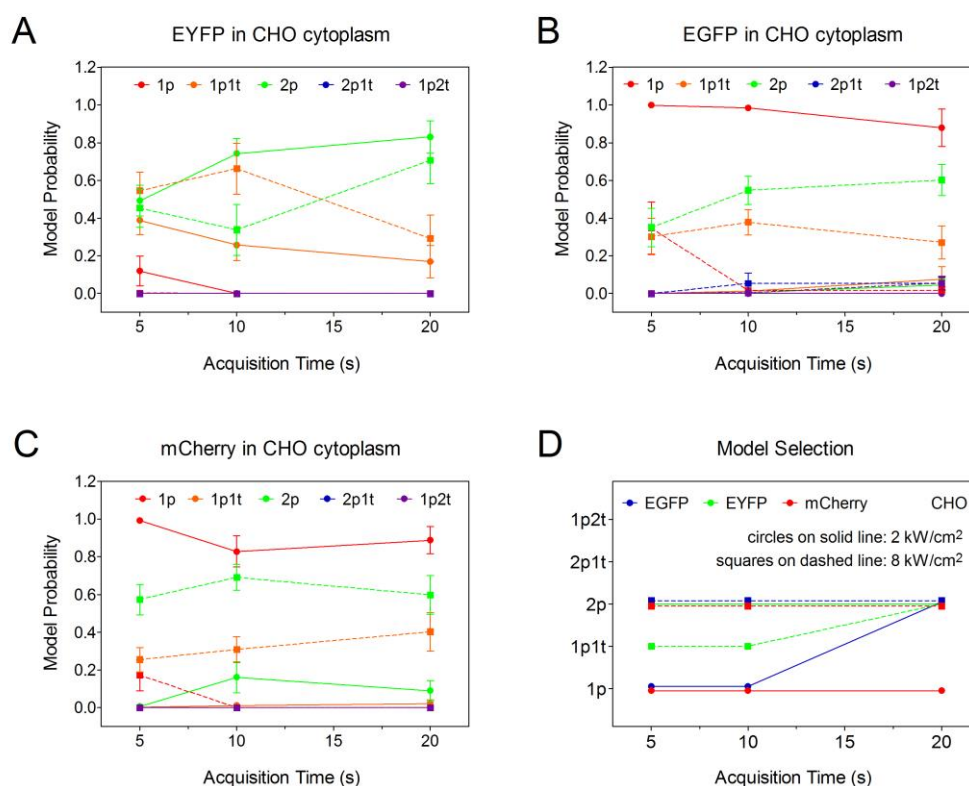


Figure 4.12 Model probabilities and model selection and of fluorescent proteins in CHO cytoplasm with different acquisition times

Model probabilities of (A) EYFP, (B) EGFP and (C) mCherry in CHO cytoplasm, under low and high excitation intensities with different acquisition times and (D) their model selection: EGFP (blue), EYFP (green) and mCherry (red). Evaluated models are 3D one-component diffusion (1p, red), one-component diffusion with one triplet (1p1t, orange), two-component diffusion (2p, green), two-component diffusion with one triplet (2p1t, blue), one-component diffusion with two triplet (1p2t, purple). Error bars: SEM Circles on solid line: 2 kW/cm²; squares on dashed line: 8 kW/cm².

4.2.3.3. Influence of temperature on data fitting

So far, the experimental temperature was kept at room temperature (r.t.), but many experiments in biology are performed at physiological temperature of 37 °C. Hence, model selection of organic dyes and fluorescent proteins in solution as well as fluorescent proteins in CHO cells was examined at 37 °C (Fig. 4.13). Atto488 and EGFP are shown as examples. The results demonstrate that high temperatures have no

influence on model selection; only the diffusion time decreased under such condition (Table 4.4 and 4.5), since it increases the Brownian motion. The triplet / isomerization time and fraction were not affected by the higher temperature but were only changed by the excitation intensity (Table 4.2 and 4.4).

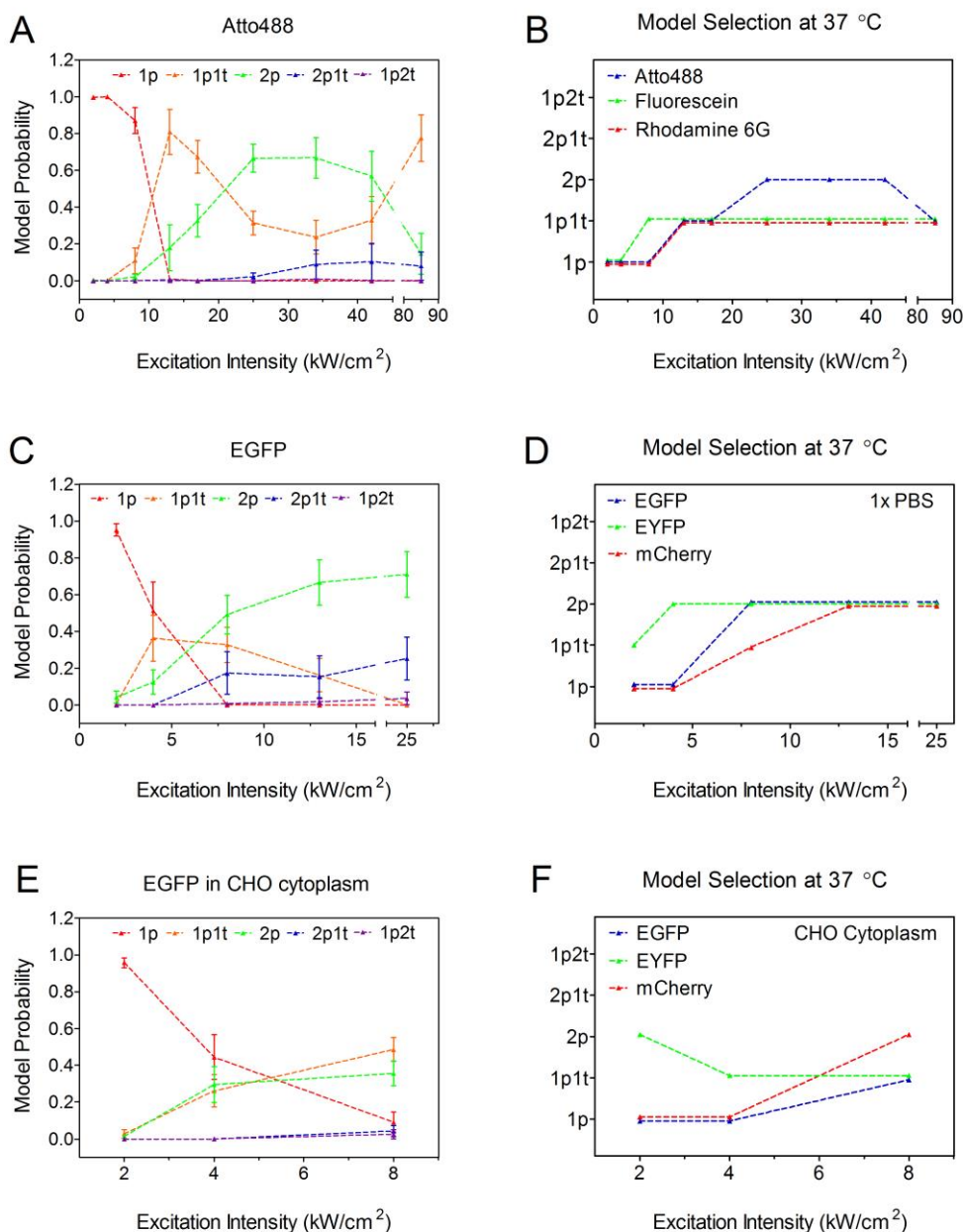


Figure 4.13 Model probabilities and model selection at 37 °C

Model probabilities of (A) Atto488, (C) EGFP in 1x PBS and (E) EGFP in CHO cytoplasm with increasing excitation intensity at 37 °C. Model selection of (B) organic dyes in 1x PBS: Atto488 (blue), Fluorescein (green) and Rhodamine 6G (red); (D) fluorescent proteins in 1x PBS and (F) in CHO cytoplasm: EGFP(blue), EYFP (green) and mCherry (red) with increasing excitation intensity at 37 °C. Evaluated models are 3D one-component diffusion (1p, red), one-component diffusion with one triplet (1p1t, orange), two-component diffusion

(2p, green), two-component diffusion with one triplet (2p1t, blue), one-component diffusion with two triplet (1p2t, purple). Error bars: SEM.

4.2.3.3. Model selection for membrane measurement

In addition to FCS measurements applied to the cytoplasm and nucleus, measurements were also performed on diffusing protein species residing in the membrane. To achieve this goal, a plasmid encoding EGFP fused to the plasma membrane target (PMT) sequence was made (Chapple, Hardcastle et al. 2002; Liu, Sudhakaran et al. 2007) and transfected in CHO cells (Fig. 4.14A). To locate the cell membrane, the pointer was first pinned to the center of the cell and then moved up to find the position with the largest fluorescence intensity fluctuation (Benda, Benes et al. 2003). Evaluated fitting models are 2-dimensional (2D) 1p, 1p1t, 2p, 2p1t, 1p2t (Eq. 2.14, 2.20, 2.16, 2.22, 2.25). The isomerization blinking time was fixed at 20 μ s, which is determined from EGFP measured in cytoplasm under the same experimental conditions (Fig.4.11B). If the blinking time was not fixed, the preferred model was 2p for all the tested excitation intensities. However, more than 80% of the data cannot be well fitted by the 1p1t, 2p1t and 1p2t, in which case the returned fitting parameters (diffusion time, triplet time and fraction) are unreasonable, either larger than thousand or smaller than 10^{-7} . For those fittings that return the reasonable values, generally 2 or 3 out of 15, the isomerization time of 1p1t is close to the fast moving component of 2p and the isomerization fraction of 1p1t is lower than the fraction of fast moving component of 2p; the isomerization time of 2p1t is 10 μ s in average and the diffusion times are close to the fitting with the triplet time fixed.

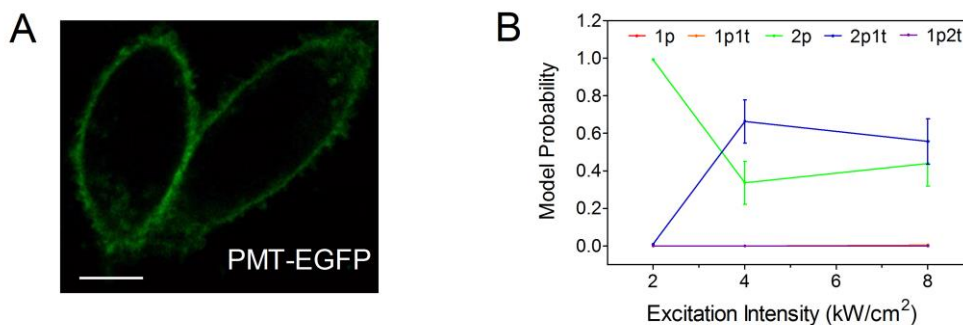


Figure 4.14 PMT-EGFP in CHO cells and its model probabilities

(A) Transient transfection of PMT-EGFP in CHO cell. Scale bar: 20 μm . (B) Model probabilities for PMT-EGFP on the membrane under different excitation intensities. Evaluated models are 2D one-component diffusion (1p, red), one-component diffusion with one triplet (1p1t, orange), two-component diffusion (2p, green), two-component diffusion with one triplet (2p1t, blue), one-component diffusion with two triplet (1p2t, purple) with the triplet blinking time fixed at 20 μs . Error bars: SEM.

Model probabilities are plotted in Fig. 4.14B and the inferred fitting parameters are shown in Fig. 4.15A to C. As a single non-functional protein, one would expect a one-component diffusion fitting preference. However, results showed a preference for the 2p model, with a transition to the 2p1t model as the excitation intensity increases. The dominant component was the slow moving component with diffusion time around 25 ms, typical for a membrane protein, with a fraction that is approximately 60%. Another component diffused much faster with diffusion time on the same order as the free EGFP measured in the cytoplasm, which was 500 to 350 μs (corresponding to 2 to 8 kW/cm^2). As the excitation intensity increased, the apparent diffusion times of the two components decreased due to photobleaching. This is in accordance with the observation of EGFP measured in the cytoplasm. To further test whether the fast component is a data analysis artifact, a series of measurements based on pinhole size was performed (Fig. 4.15D). As the pinhole size increases, the observation volume increases, thereby it will take a longer time for the fluorophore to pass through the volume and result in a longer diffusion time. Both the fast and slow moving components showed a pinhole-dependent change. Therefore, both components are

stemming from particle motion, here diffusion. The fast component could be a result of movement towards the membrane due to the transportation from the endoplasmic reticulum (ER) to the membrane and in the opposite direction due to the dynamic internalization or recycling of the membrane (Steinman, Mellman et al. 1983; Mellman 1996).

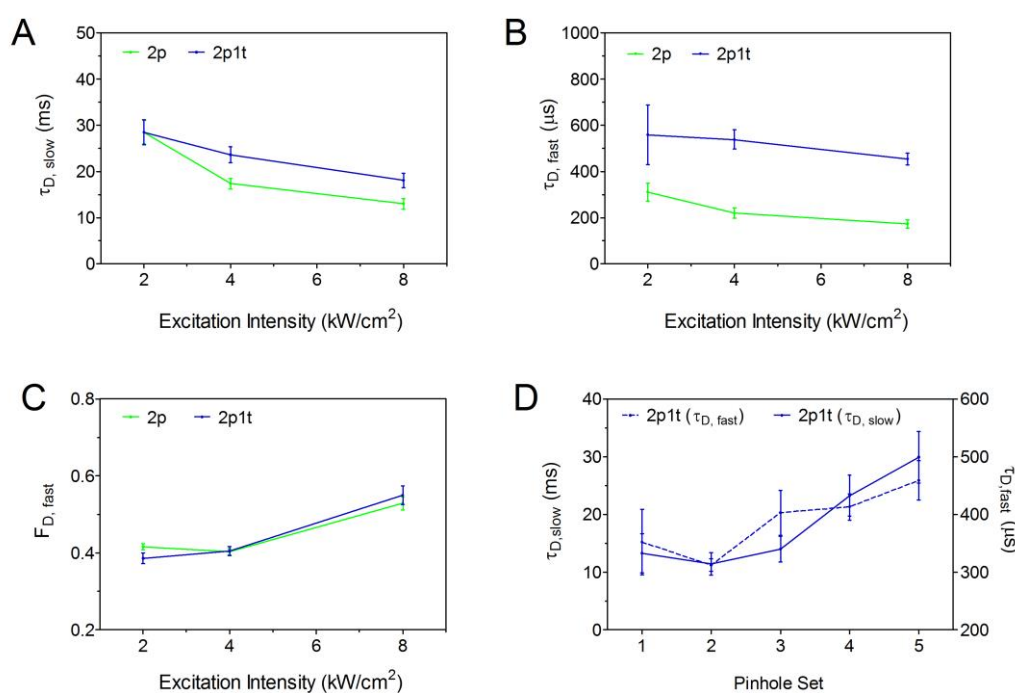


Figure 4.15 Inferred fitting parameters of PMT-EGFP on CHO membrane with different excitation intensities and pinhole sizes

(A) Diffusion time of the slow moving component $\tau_{D,slow}$; (B) Diffusion time of the fast moving component $\tau_{D,fast}$; (C) Fraction of the fast moving component $F_{D,fast}$ with increasing excitation intensity. Evaluated models are 2D two-component diffusion (2p, green) and two-component diffusion with a triplet (2p1t, blue). (D) Diffusion times of both the slow (solid line) and fast (dashed line) moving components with changing pinhole sizes. Error bars: SEM.

In the case of over-expression PMT-EGFP, it can be seen accumulated in the cytoplasm (Fig. 4.16A). FCS was then performed in the cytoplasm under 4 kW/cm² excitation (cross in Fig. 4.16A). The data are normalized and plotted together with membrane measurement in Fig. 4.16B and the inferred fitting parameters are listed in Table 4.1. The diffusion time of PMT-EGFP in the cytoplasm was close to free

cytosol EGFP, 480 μs at 4 kW/cm^2 , but larger than the fast moving component detected from membrane measurement (Table 4.1). It should be noted that the diffusion time difference between PMT-EGFP in the cytoplasm and on the membrane may come from the fitting model difference. In the 2p model, the decay of the fast and slow diffusion components is not independent. With an extra parameter on the right (longer lag time τ), the decay of the fast diffusion component is ‘squeezed’ a little to the left (shorter lag time τ) and thus the diffusion time is underestimated.

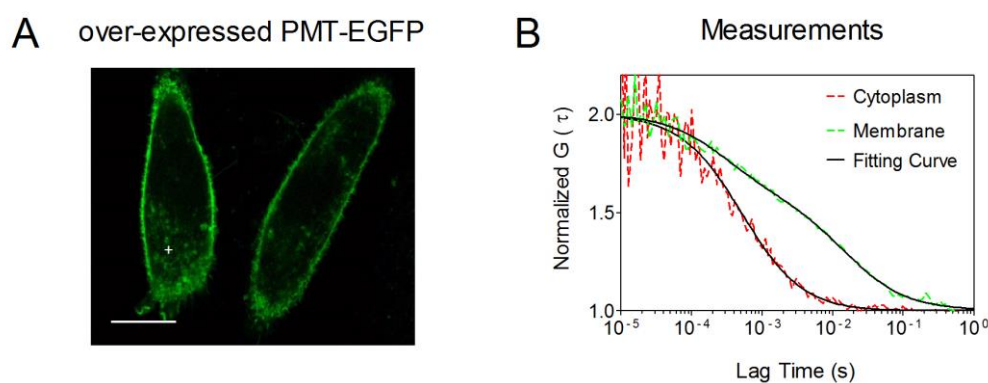


Figure 4.16 Over-expression of PMT-EGFP in CHO cytoplasm

(A) Over-expression of PMT-EGFP in CHO cell. Scale bar: 20 μm . (B) Normalized ACFs of measurement in the cytoplasm (cross in A, red dotted line) and on the membrane (green dotted line) with fits (black line).

Table 4.1 Parameters inferred for PMT-EGFP on the membrane and in the cytoplasm

PMT-EGFP	$\tau_{D,\text{fast}}$ (μs)	$\tau_{D,\text{slow}}$ (ms)	F_{slow} (%)
Membrane	224 \pm 49	21 \pm 6	60 \pm 2
Cytoplasm	586 \pm 30	-	-

Data is mean \pm SEM. Measurements were taken under 4 kW/cm^2 excitation

4.2.3.4. Model selection for measurements in zebrafish

In view of the robustness of this Bayesian model selection approach, this methodology was employed to evaluate transport models for EGFP labeled proteins measured in live zebrafish embryos. Zebrafish Wnt3 is a type of lipid modified signaling protein and is essential in neural development and proliferation. However, its signaling and trafficking process have barely been revealed in terms of molecular dynamics. In the next chapter, FCS will be applied to address these issues. Beforehand, the appropriate fitting models for the EGFP labeled proteins in different cell compartments will be determined using this Bayesian approach.

The construction of the EGFP labeled proteins was introduced in details in Section 2.2.3.1 and 2.2.3.2. Briefly, due to the lipid modification, Wnt3EGFP locates on the membrane. LynEGFP, as a negative control, is a non-functional membrane located protein. Similar to PMT-EGFP, it is on the membrane due to the membrane localization domain of Lyn protein (Haas and Gilmour 2006). EGFP^{F2}, EGFP driven by *wnt3* promoter, is expressed inside the cell and thus used to quantify the protein intracellular mobility. F2 stands for family 2, which is with lower expression level, suitable for FCS measurement. The extracellular protein mobility is represented by the secreted secEGFP, which is EGFP driven by a secretion domain (Yu, Burkhardt et al. 2009). Their expression in the zebrafish brain is shown in Fig. 4.17.

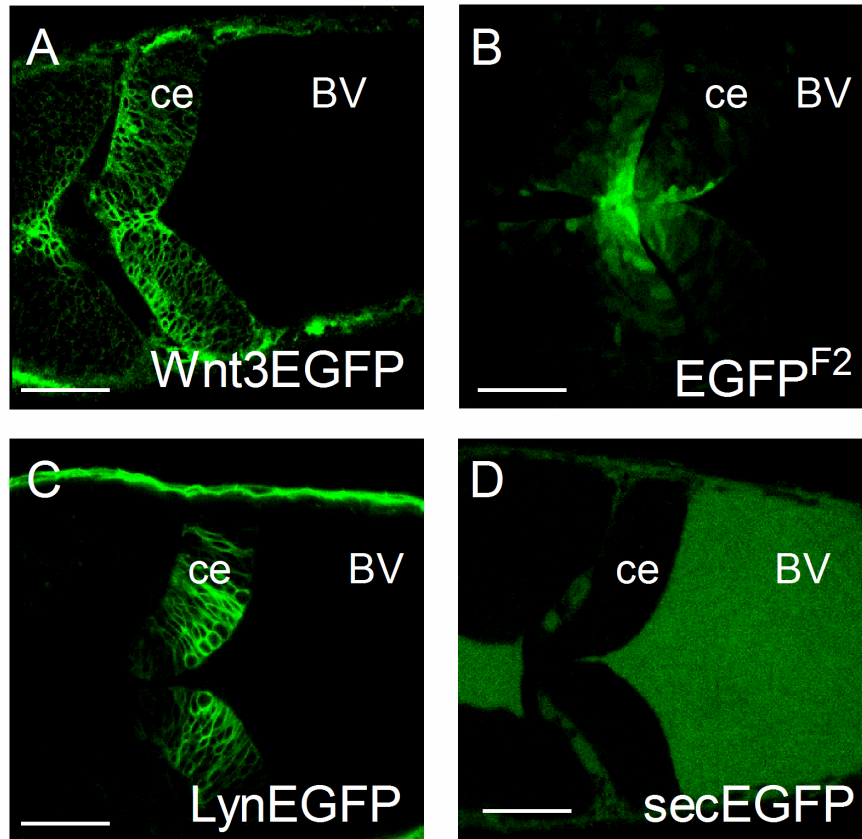


Figure 4.17 Confocal images of zebrafish brain expressing EGFP label proteins

(A) Wnt3EGFP, (B) EGFP^{F2}, (C) LynEGFP and (D) secEGFP at 34 hpf. Scale bar, 50 μm . Images were taken in dorsal view. ce: cerebellum; BV: brain ventricle.

For membrane located Wnt3EGFP and LynEGFP, evaluated fitting models are 2D 1p, 1p1t, 2p, 2p1t, 1p2t. For Wnt3EGFP and secEGFP in the brain ventricle, which is full of fluid, as well as EGFP^{F2} inside the cell, evaluated fitting models are 3D 1p, 1p1t, 2p, 2p1t, 1p2t. The isomerization time was also fixed at 20 μs as for PMT-EGFP. The experimental condition used was 15 μW (corresponding to excitation intensity 6 kW/cm^2) with acquisition time 15 s. The model probabilities are plotted in Fig. 4.18. The model for secEGFP and EGFP^{F2} is 3D-1p1t; Wnt3EGFP and LynEGFP on the membrane is 2D-2p1t. Particularly for Wnt3EGFP in the brain ventricle, 3D-2p1t is preferred. In this case, the mobility of the fast moving component is on the same order of the mobility of secEGFP and the mobility of the slow one is with a relatively large

range from 1 to 50 ms. Detailed discussion on the data will be included in the next Chapter. Hence, the selected models were used for the data fitting.

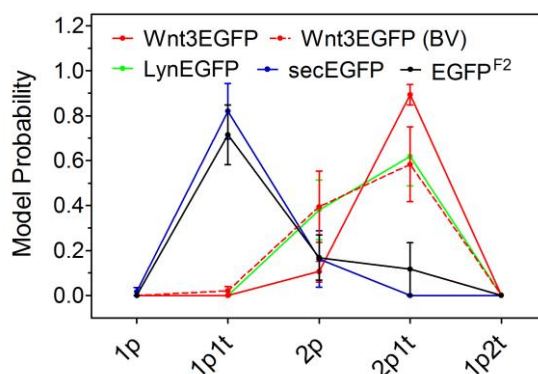


Figure 4.18 Model probabilities of EGFP labeled proteins measured in zebrafish embryos

Model probabilities of Wnt3EGFP on the membrane (red, solid), in the brain ventricle (red, dashed), LynEGFP on the membrane (green), secEGFP in the brain ventricle (blue) and EGFP^{F2} inside the cell (black). Error bars: SEM.

4.3. Discussion

4.3.1. Model selection under various conditions

As the excitation intensity increases, the signal-to-noise ratio improves, and the population of the triplet state for dyes and the blinking for fluorescent proteins also increases. With increasing intensity, saturation and photobleaching start appearing. The apparent diffusion time inferred from fitting is the net result of these two different effects. It is shorter due to photobleaching, since the fluorophore bleaches before it moves out of the observation volume, as shown by the fluorescent proteins. In the case of saturation, it is longer due to the enlarged observation volume, as shown by the organic dyes. Under low excitation intensity, one-component diffusion is enough to describe the ACF of all three fluorescent proteins both in solution and in the cell cytoplasm and nucleus. As the excitation intensity increases but before

saturation, one-component diffusion with a triplet dynamic is appropriate. Even though one-component diffusion with two triplets has been reported to fit fluorescent proteins in solution, it is never preferred under the conditions in this study. The possible reason for this is that the multiple blinking is shown at a higher excitation intensity than the examined level (Widengren, Mets et al. 1999). On the other hand, the two-component diffusion model without triplets dominates at a high level of excitation intensity. Without this model in the list of evaluated models, 1p2t is still never preferred. Beyond the saturation, parameters to adjust the distorted observation volume should be included in the fitting function (Nagy, Wu et al. 2005).

Under low excitation intensity, doubling or tripling the acquisition time does not change the fitting model. However, it does smooth the experiment curve and improves the data quality with better precision of the inferred fitting parameters, indicated by the reduced standard error (Fig. 4.19). At high excitation intensity, reducing the acquisition time can barely recover the expected model. Experimental temperature has no influence on model selection and the blinking process of both, dyes and fluorescent proteins, in all cases. It only increases diffusion. This is expected, since the diffusion is a thermally activated process.

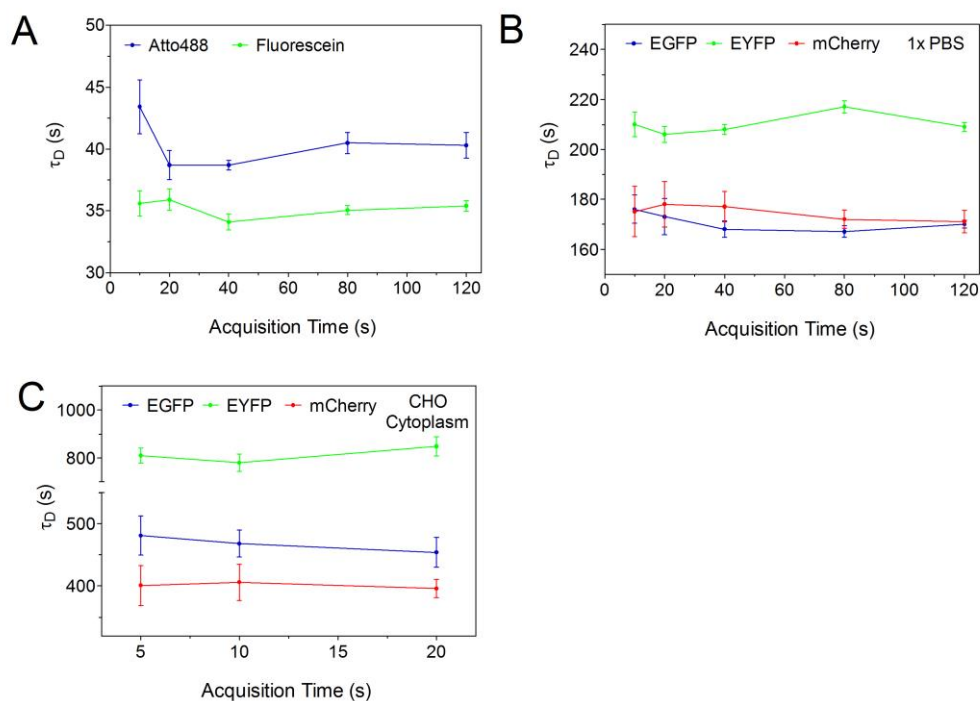


Figure 4.19 Fitting parameters inferred for measurement with different acquisition times under low excitation intensity

Diffusion time τ_D , of (A) Atto488 (blue) and Fluorescein (green), (B) EGFP(blue), EYFP (green) and mCherry (red) in 1x PBS and (C) EGFP(blue), EYFP (green) and mCherry (red) in CHO cytoplasm. Fitting models for EYFP in 1x PBS and CHO cytoplasm are 3D one-component diffusion with one triplet (1p1t) and the others are 3D one-component diffusion (1p). Excitation intensity is 2 kW/cm^2 . Error bars: SEM.

It should be noticed that a fitting model should be consistent for comparison. As shown in Fig. 4.3, 4.7, 4.11 and 4.15, diffusion time inferred from 1p1t is larger than that from 1p. Similar to the difference between 1p and 2p model discussed in Section 4.2.3.3, in the 1p1t model, the decay of the diffusion component and the triplet dynamic is not independent. With an extra parameter on the left (shorter lag time τ), the decay of the diffusion component is ‘squeezed’ a little to the right (longer lag time τ) and thus the diffusion time is overestimated. Similarly, it should be expected that the diffusion time inferred from 1p2t will be even larger. Therefore, the fitting model should be carefully chosen and kept consistent in data analysis.

4.3.2. Anomalous diffusion

Since the anomalous diffusion has been reported in cell measurement, this fitting model is also included in the tested model list at the beginning. However, surprisingly, this model was selected not only for cell measurements but also for organic dyes and fluorescent proteins in solution. It competes with 1p1t under moderate excitation intensity from 8 to 13 kW/cm². It is not preferred at low excitation intensity, below 4 kW/cm², as well as at very high excitation intensity where 2p is still dominant. The parameters inferred from anomalous diffusion fits ($3D_{1p, \text{Ano}}$, Eq. 2.13) are compared with a one-component diffusion model and results are listed in Table 4.2. In the case of Atto488, the fitting returns the anomaly degree of the diffusion α with a value around 0.96 and a diffusion time about 90% of the value inferred from 1p fitting. Since α is close to 1, the shape of the fitting curve of anomalous fitting is quite similar to free diffusion. Similar results are also found for EGFP in 1x PBS and in cytoplasm and nucleus. In EGFP solution, α is further decreased to 0.92. Since the particles are not possible to undergo sub-diffusion in this condition, the results indicate that this parameter is not reliable. The decrease of α may come from the triplet dynamics difference between Atto488 and EGFP. The further decrease of α for EGFP in the cytoplasm should result from the same reason. In the nucleus, this anomalous diffusion model was not preferred (data not shown). Therefore, it is very possible that this fitting model could be just a substitute for 1p1t but does not reflect the diffusion pattern of the fluorophore. Therefore, the anomalous diffusion model is not included in the evaluated models in the rest of the study.

Table 4.2 Parameters inferred from anomalous diffusion fitting

	EI (kW/cm ²)	$\tau_{D, 1P}$ (μ s)	$\tau_{D, 1P_Ano}$ (μ s)	α	mp
Atto488	8	40 \pm 1	36 \pm 1	0.96 \pm 0.003	0.46 \pm 0.11
EGFP in 1x PBS	4	170 \pm 5	146 \pm 3	0.92 \pm 0.01	0.61 \pm 0.12
EGFP in CHO cytoplasm	4	463 \pm 18	367 \pm 18	0.86 \pm 0.01	0.52 \pm 0.11

Data is mean \pm SEM; mp: model probability.

4.3.3. Characteristic parameters inferred from the determined models

Based on the selected model, the characteristic parameters for the tested organic dyes and fluorescent proteins measured in 1x PBS under moderate excitation intensities are listed in the Table 4.3 and those for fluorescent proteins measured in the cell are listed in Table 4.4. The diffusion coefficients are also calculated using Eq. 2.36. It should be noted that the apparent diffusion time measured at different excitation intensity and fitted with different models should not be used for comparison. The results from measurements at 37 °C are also listed in Table 4.5 and 4.6. With increased temperature, the mobility increased approximately 15% compared to the value measured at r.t..

Table 4.3 Characteristic parameters inferred from the determined models of organic dyes and fluorescent proteins in 1x PBS

Species	EI (kW/cm ²)	τ_D (μ s)	D (μ m ² s ⁻¹)	τ_{trip} (μ s)	F _{trip} (%)
Atto488	13	48 \pm 1	400 ^[1]	7 \pm 1	15 \pm 1
Fluorescein		44 \pm 0.4	425 ^[2]	1 \pm 0.2	41 \pm 1
Rhodamine 6G		42 \pm 0.3	414 ^[3]	4 \pm 1	11 \pm 0.4
EYFP	2	209 \pm 2	82 \pm 1	17 \pm 1	14 \pm 0.3
EGFP	4	204 \pm 12	98 \pm 5	25 \pm 7	22 \pm 2
mCherry	8	265 \pm 14	47 \pm 2	75 \pm 5	42 \pm 2

Fitting model is 3D-1p1t. Data is mean \pm SEM

[1] Dertinger and Ewers 2008; [2] Culbertson, Jacobson et al. 2002; [3] Müller, Loman et al. 2008.

Table 4.4 Characteristic parameters inferred from the determined models of fluorescent proteins in CHO cells

Species	EI (kW/cm ²)	Cytoplasm		Nucleus	
		τ_D (μ s)	D (μ m ² s ⁻¹)	τ_D (μ s)	D (μ m ² s ⁻¹)
EYFP	0.4	497 \pm 19	35 \pm 1	479 \pm 27	37 \pm 2
EGFP	4	480 \pm 12	40 \pm 1	420 \pm 14	47 \pm 1
mCherry	4	255 \pm 13	49 \pm 2	282 \pm 13	44 \pm 2

Fitting model is 3D-1p. Data is mean \pm SEM

Table 4.5 Characteristic parameters inferred from the determined models of organic dyes and fluorescent proteins in 1x PBS at 37 °C

Species	EI (kW/cm ²)	τ_D (μ s)	τ_{trip} (μ s)	F _{trip} (%)
Atto488	13	42 \pm 1	7 \pm 1	18 \pm 1
Fluorescein		37 \pm 0.3	1 \pm 0.1	42 \pm 1
Rhodamine 6G		37 \pm 0.5	4 \pm 1	11 \pm 1
EYFP	2	181 \pm 3	18 \pm 3	13 \pm 1
EGFP	4	156 \pm 5	18 \pm 5	17 \pm 1
mCherry	8	233 \pm 20	54 \pm 7	46 \pm 3

Fitting model is 3D-1p1t. Data is mean \pm SEM

Table 4.6 Characteristic parameters inferred from the determined models of fluorescent proteins in CHO cells at 37 °C

Species	EI (kW/cm ²)	Cytoplasm	Nucleus
		τ_D (μ s)	τ_D (μ s)
EYFP	0.4	244 \pm 16	288 \pm 12
EGFP	4	334 \pm 22	299 \pm 12
mCherry	4	208 \pm 11	222 \pm 16

Fitting model is 3D-1p. Data is mean \pm SEM

4.4. Conclusion

Firstly, model selection is sensitive to excitation intensity. The triplet state population or blinking dynamic can be induced by increased excitation intensity and thus this process should be included in describing ACFs. Generally, acquisition time and temperature barely affects the model selection. Secondly, one-component diffusion is enough to fit fluorescent proteins diffusion in cell cytoplasm and nucleus. However, two-component diffusion should be included in membrane locate protein data analysis. Through the discussion, it is demonstrated that anomalous diffusion should be used with great caution. Finally, this approach has been applied in model evaluation for FCS measured in zebrafish embryos. In conclusion, the Bayesian model selection approach is an unbiased and effective way to evaluate FCS data and determine the appropriate fitting model. In view of its robustness, this method should be considered as a preliminary test for the data analysis.

Chapter 5

Wnt3EGFP Intercellular Trafficking Study in Zebrafish

Brain Development by Fluorescence Techniques

5.1. Introduction

The debate on the trafficking mechanisms for secreted lipid modified signaling proteins has been raised decades ago, yet the mechanisms have still not been unambiguously identified. Several mechanisms have been proposed, such as transportation by lipoproteins or exosomes, lateral diffusion aided by HSPG or Wnt related secreted receptors, planar transcytosis and cytonemes (see Section 1.1.3). With the development of genetic labeling strategies and fluorescence techniques, it is possible to take a better look at this issue with higher spatial and temporal resolution. This chapter will introduce fluorescence correlation spectroscopy (FCS) in light of this problem.

In this chapter, zebrafish Wnt3EGFP expression patterns during different brain development stages will first be investigated using confocal microscopy. Its mobility in different cell compartments as well as in the intercellular space and brain ventricle will be determined. Moreover, its intercellular trafficking mechanism will be explored.

5.2. Results and Discussions

5.2.1. Wnt3EGFP expression in the cerebellum

At first, Wnt3EGFP localization and behavior in zebrafish cerebellum development were investigated using confocal microscopy. The EGFP labeled protein constructions are detailed in Section 2.2.3. Briefly, the *wnt3* promoter was used to drive the Wnt3EGFP protein expression to be in a similar pattern as the endogenous Wnt3 protein. As shown in Fig. 2.6, Wnt3EGFP is expressed in the cerebellum (ce), epithalamus (ep), floor plate (fp), caudal hypothalamus (hyp), optic tectum (ot), roof plate (rp), midbrain hindbrain boundary (MHB) and hindbrain (hb) and deep in the zona limitans intrathalamica (zil). The localization is consistent with Clements's work (Clements, Ong et al. 2009). Of all the expression regions, cerebellum is the focus of this research. On the other hand, EGFP^{F1}, which is the EGFP driven by the *wnt3* promoter, was constructed to obtain the information about endogenous Wnt3 expression.

Fig. 5.1 shows the different expression patterns for EGFP^{F1} and Wnt3EGFP in the cerebellum at different development stages. As presented in Fig. 5.1A and B, the primary difference between them is the localization in a cell. EGFP^{F1} is restricted in the cell, whereas Wnt3EGFP shows a clear cell outline. This is expected, since EGFP^{F1} is only driven by the *wnt3* promoter. Without the functional domains, it can neither be secreted from the cell nor transported to the membrane. As for Wnt3EGFP, it locates to the membrane and the extracellular matrix due to the lipid modifications. At these developmental stages, most of the intracellular space is occupied by the large nuclei, indicated by the Histone H2A-EGFP expression (Fig. 5.1C). It is worth noting that the distribution in the cerebellum changes with the developmental stages.

Generally, the Wnt3EGFP amount decreases from the dorsal midline (DM) to the lateral side (LS), while EGFP^{F1} shows similar patterns but with far larger amounts along the edge of the cerebellum structure (Fig. 5.1D-F and G-I). As the cerebellum grows, the amount of Wnt3EGFP in the DM starts to decrease after 34 hpf. To 48 hpf, only cells in the LS can be detected (Fig. 5.1D-F). However, no significant drop is observed for EGFP^{F1} during these stages (Fig. 5.1G-I). Since the EGFP^{F1} only mimics the Wnt3EGFP expression pattern, the difference between them should be an indication of Wnt3EGFP secretion and transportation. Even though it is shown that Wnt3EGFP has been transported to the membrane, its mobility cannot be characterized by confocal images. Moreover, it cannot be distinguished whether there are free moving Wnt3EGFP inside or outside the cell. Therefore, FCS was performed on the membrane to resolve these issues.

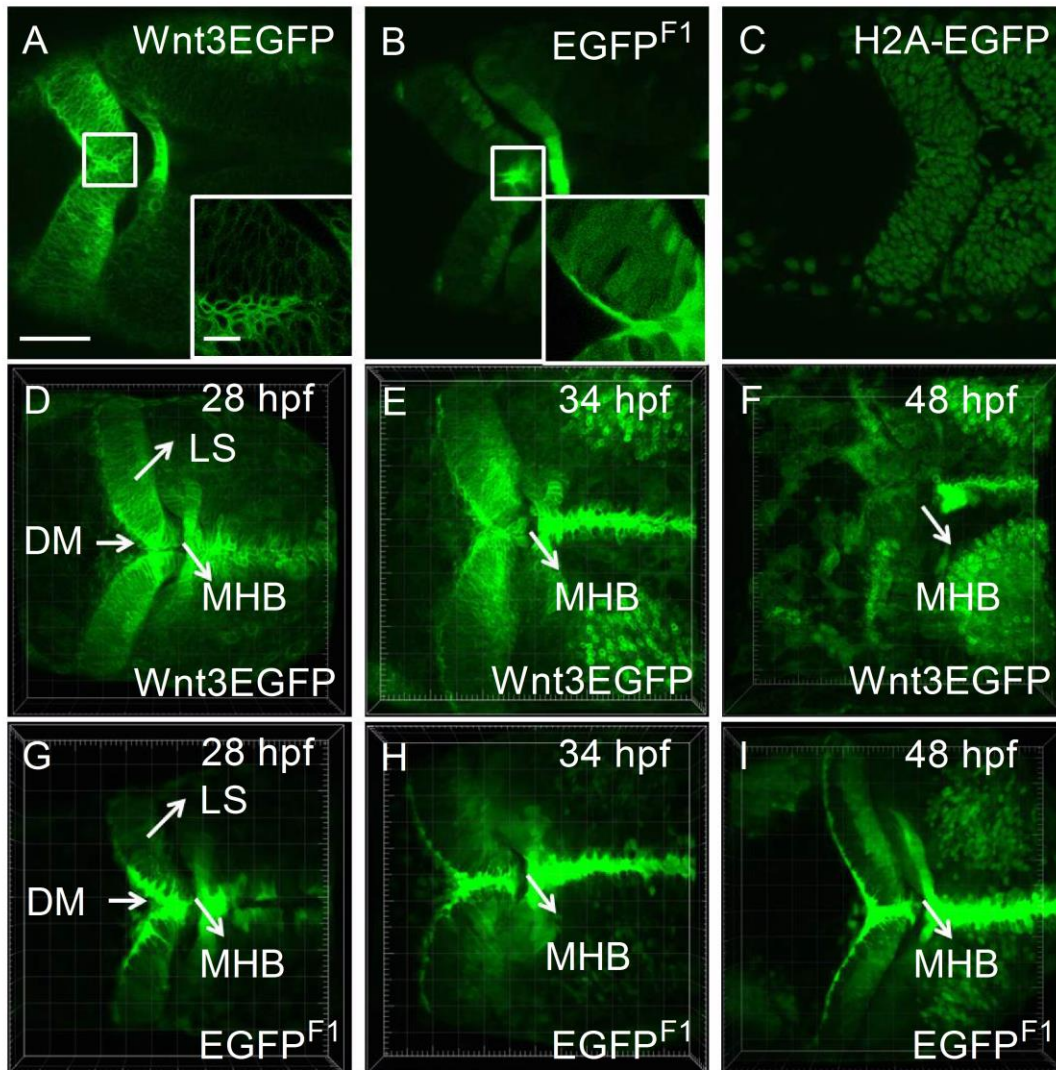


Figure 5.1 Wnt3EGFP and EGFP^{F1} expressions in the cerebellum

Single confocal images showing different localizations in the cell for (A) Wnt3EGFP, (B) EGFP^{F1} reporter and (C) Histone H2A-EGFP. Inserted figures are 4 times zoom in images in the white box in A and B. The illustrated images were taken at 34 hpf. 3D projections of confocal images of (D-F) Wnt3EGFP and (G-I) EGFP^{F1} reporter expressing in the cerebellum (together with the optic tectum on the right) at different development stages. Scale bar is 100 μm. All the images are in the same scale. Scale bar in the magnified images is 10 μm. ce: cerebellum; ot: optic tectum; MHB: midbrain hindbrain boundary; DM: dorsal midline; LS: lateral side.

5.2.2. Wnt3EGFP membrane dynamics and distribution

To perform cell to cell communication, it is important for signaling proteins to pass through the membrane. Parameters including membrane distribution and protein mobility can be determined from FCS. Fig. 5.2A shows a typical autocorrelation

curve measured on the membrane, the experimental data was fitted with 2D-2p1t (Eq. 2.22), as determined by Bayesian model selection in Section 4.2.3.4.. The dominant state detected was a membrane anchored component with a diffusion coefficient (D_2) of around $1 \mu\text{m}^2/\text{s}$ and its fraction (F_2) was approximately 60%. Its membrane localization could be on the side of secreting cells due to membrane insertion or on the side of the signal receiving cells due to Wnt3-receptor binding. Another component diffused much faster with a diffusion coefficient (D_1) of around $30 \mu\text{m}^2/\text{s}$. To quantify the protein intracellular mobility, a weaker expressing EGFP reporters, EGFP^{F2}, was used as a substitute of EGFP^{F1} for FCS measurement (see Section 2.2.3.1). It was found that the fast moving component of Wnt3EGFP has a similar behavior as the EGFP^{F2} but diffuses slower due to their molecular size difference (Table 5.1). This indicates the existence of free moving Wnt3EGFP, but possibly together with other component(s) in a soluble complex considering its lipid modification. However, whether this component is in or out of the cell remains unclear.

Since the Wnt3EGFP distribution changes in both the DM and the LS of the cerebellum as the embryos grow, measurements were performed in these two regions at different development stages - 28, 34 and 48 hpf. As shown in Fig. 5.2B-D, the Wnt3EGFP mobility of both the fast and slow components (D_1 and D_2) as well as its membrane fraction (F_2) keeps almost constant in the whole cerebellum as the embryo grows. The data was also analyzed for cells with different expression levels which were indicated by the intensity count rates (Fig. 5.2). No significant difference in terms of Wnt3EGFP membrane fraction (F_2) due to the expressing amount is observed. These data suggest that this cerebellum model is in a stable dynamic equilibrium.

As a negative control, LynEGFP, a non-functional membrane protein, was also analyzed (see Section 2.2.3.1). To locate EGFP on the membrane, a short membrane localization domain of Lyn, was genetically added to EGFP. Its expression in zebrafish was driven by promoter *ClaudinB*. Compared to Wnt3EGFP, the mobility of the fast moving components of LynEGFP was on the same order but with increase in diffusion coefficient due to their different molecular size (Fig. 5.2B). The difference of the slow moving component comes from their different properties, since Wnt3EGFP is lipid modified, whereas LynEGFP is only anchored on the membrane by the membrane locate domain (Fig. 5.2C). Moreover, LynEGFP has approximately 5% more in membrane distribution. Similar to Wnt3EGFP, the expression level does not influence the membrane fraction (Fig. 5.2E). Since LynEGFP is not functional, it cannot be secreted from the cell and therefore its fast component can only be inside the cell. But where is the 5% more free moving component of Wnt3EGFP? They can be either more inside the cell or more out of the cell. To figure out whether there are free Wnt3EGFP secreted out of the cell, the focus is then moved to the brain ventricle.

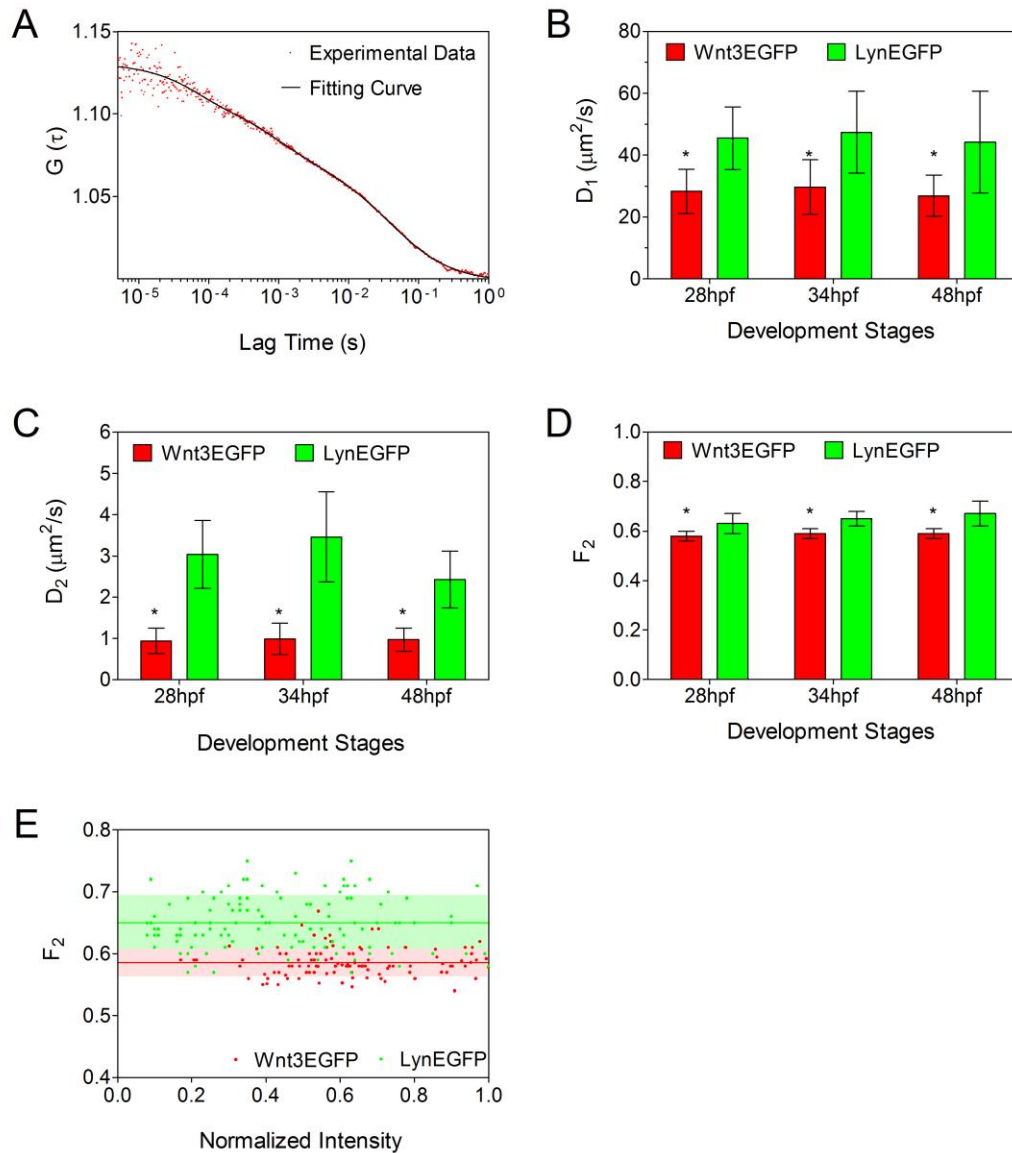


Figure 5.2 Wnt3EGFP and LynEGFP membrane dynamics in the cerebellum investigated by FCS

(A) Autocorrelation curve of Wnt3EGFP on the membrane of cells in the cerebellum. The curve is fitted to a 2-dimensional two component model including a blinking process (2D-2p1t, Eq. 2.21). Dotted line is the experimental data. Solid line is the fit curve. (B and C) Diffusion coefficients (D_1 , D_2) inferred from fit at different development stages. (D) Fraction of slow moving component (F_2) inferred from fit at different development stages. Data are mean \pm SD. Red bar, Wnt3EGFP. Green bar, LynEGFP. Significance level, two-way t-test, $*P < 0.001$. See also Table 5.1. (E) The membrane fraction did not change with the expressing amount which was indicated by normalized intensity count rate, for both Wnt3EGFP (red) and LynEGFP (green). Lines represent average and shade areas represent its SD.

Table 5.1 Measurement on membrane for Wnt3EGFP and LynEGFP at different development stages

Species	Development Stages (hpf)	D ₁ (μm ² s ⁻¹)	D ₂ (μm ² s ⁻¹)	F ₂ (%)	Total Embryo No.	Total Cell No.
Wnt3EGFP	28	28.36 ± 7.17	0.94 ± 0.31	58 ± 2	5	24
	*28	29.82 ± 7.88	0.81 ± 0.33	59 ± 2	4	30
	34	29.70 ± 8.81	0.99 ± 0.38	59 ± 2	5	22
	*34	31.93 ± 9.06	0.85 ± 0.28	60 ± 2	6	28
	48	26.88 ± 6.68	0.97 ± 0.28	59 ± 2	5	26
LynEGFP	28	45.48 ± 10.10	3.04 ± 0.82	63 ± 4	6	35
	34	47.42 ± 13.19	3.46 ± 1.09	65 ± 3	6	35
	48	44.19 ± 16.39	2.43 ± 0.69	67 ± 5	5	33
EGFP ^{F2}	28	38.74 ± 8.54	-	-	3	30

Data are mean ± SD of number of cells measured. Measurements were performed in the lateral side (LS) region for comparison between Wnt3EGFP and LynEGFP. *Measurements performed in the dorsal midline (DM) region.

5.2.3. Wnt3EGFP extracellular and intercellular diffusion

5.2.3.1. Wnt3EGFP in the brain ventricle

To further investigate the existence of extracellular Wnt3EGFP, the focus was moved to the cerebellum boundary and flanking brain ventricle (Fig. 5.3A-C). Based on confocal imaging, a simple way to see whether there is Wnt3EGFP secreted from the cell is by analyzing its intensity profile. Therefore, X-scanning was performed for Wnt3EGFP, LynEGFP and the secreted protein secEGFP (see Section 2.2.3.2) positive control from the cerebellum boundary cell to the brain ventricle along the white arrows in Fig. 5.3A1-C1. The intensities were normalized to the highest intensity, which was the membrane in Wnt3EGFP and LynEGFP. To show the

secretion protein distribution, the profile of secreted secEGFP was also analyzed. Its intensity was firstly normalized to the average intensity in the brain ventricle and then aligned to the membrane with Wnt3EGFP and LynEGFP using the red membrane marker KillerRed by co-expressing. The intensity profile of Wnt3EGFP in the brain ventricle was only a slightly elevated compared to LynEGFP, indicating Wnt3EGFP can be secreted and transported to the brain ventricle (Fig. 5.3D). The small gap is consistent with the small extracellular amount inferred from the membrane fraction F_2 difference in Fig. 5.2D and E. FCS was then performed at 100 μm away from the cerebellum boundary in the brain ventricle to further confirm Wnt3EGFP existence. The autocorrelation curves showed Wnt3EGFP free diffusion as the secEGFP, whereas neither LynEGFP nor wild type (WT) can be detected (Fig. 5.3E). These results confirm the existence of secreted Wnt3EGFP in the extracellular space.

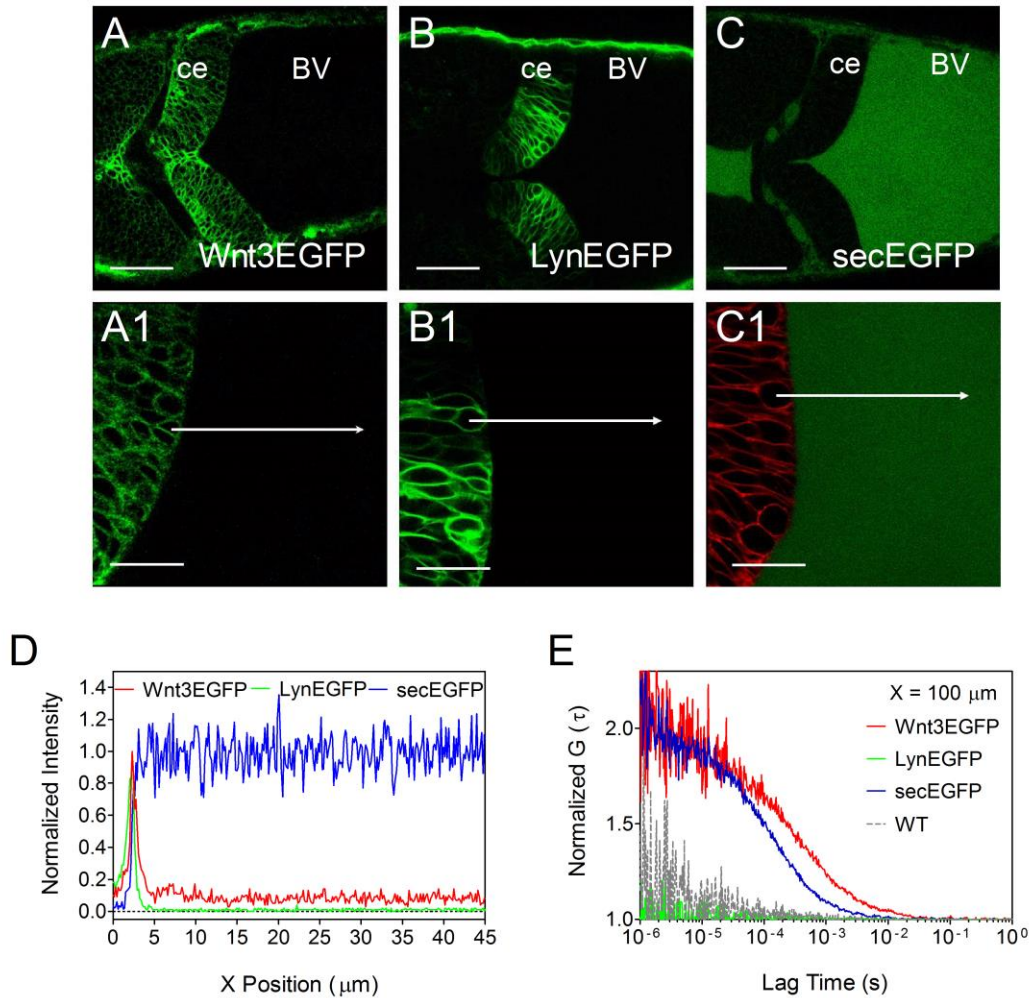


Figure 5.3 Secretion of Wnt3EGFP, LynEGFP and secEGFP to the brain ventricle

(A, B, C) Confocal images of zebrafish cerebellum expressing Wnt3EGFP, LynEGFP and secEGFP at 34 hpf. Scale bar, 50 μm. Images were taken in dorsal view. Ce: cerebellum; BV: brain ventricle. (A1, B1, C1) Three times zoom in of A, B and C, respectively, with focus on the boundary of the cerebellum and flanking brain ventricle. Scale bar, 20 μm. X-scanning was performed along the white arrow. Membrane in secEGFP was recognized by the red membrane marker KillerRed in the red channel (red in C1). Data were analyzed using ImageJ and Microsoft Excel. (D) Normalized intensity from the cerebellum boundary cell to the brain ventricle along the white arrows in A1, B1 and C1 for Wnt3EGFP (red), LynEGFP (green) and secEGFP (blue). Data are the average of three scans of three embryos for each type. (E) Normalized FCS of Wnt3EGFP (red), LynEGFP (green), secEGFP (blue) and wild type (WT, grey). Data were measured 100 μm away from the cerebellum cell boundary in the brain ventricle.

5.2.3.2. Wnt3EGFP extracellular and intercellular mobility

Next, the protein mobility in different environments was analyzed (Fig. 5.4).

Intercellular protein mobility was represented by secEGFP measured in the

cerebellum. This mobility is half of its extracellular mobility measured in the brain ventricle. EGFP^{F2} and fast moving component of LynEGFP represent the intracellular protein mobility, which is quite close to the intercellular mobility. The protein mobility difference indicates an environmental change, most likely viscosity. This means that the intracellular and intercellular viscosities are quite similar, but are higher than the viscosity in the brain ventricle. Accordingly, it is reasonable to have quite similar Wnt3EGFP free diffusion in and out of the cell in the cerebellum, accounting for the fast moving component. Due to the viscosity change, the secreted Wnt3EGFP in the brain ventricle diffuses twice as fast as in the cerebellum, which is in accord with secEGFP.

However, an extra slow moving component with diffusion coefficients $0.5 - 15 \mu\text{m}^2/\text{s}$ was observed for Wnt3EGFP in the brain ventricle (Fig. 5.4B-D). The fraction of this component also varied in a large range, 3 – 30%. This high heterogeneity may be due to the aggregation of lipid modified Wnt3EGFP or its binding to some extracellular matrix component, such as HSPG (Baeg, Selva et al. 2004; Han, Yan et al. 2005; Yan and Lin 2009) or lipoprotein (Pan ákov á Sprong et al. 2005; Neumann, Coudreuse et al. 2009; Mulligan, Fuerer et al. 2012), or transportation complexes after secretion (Gross, Chaudhary et al. 2012).

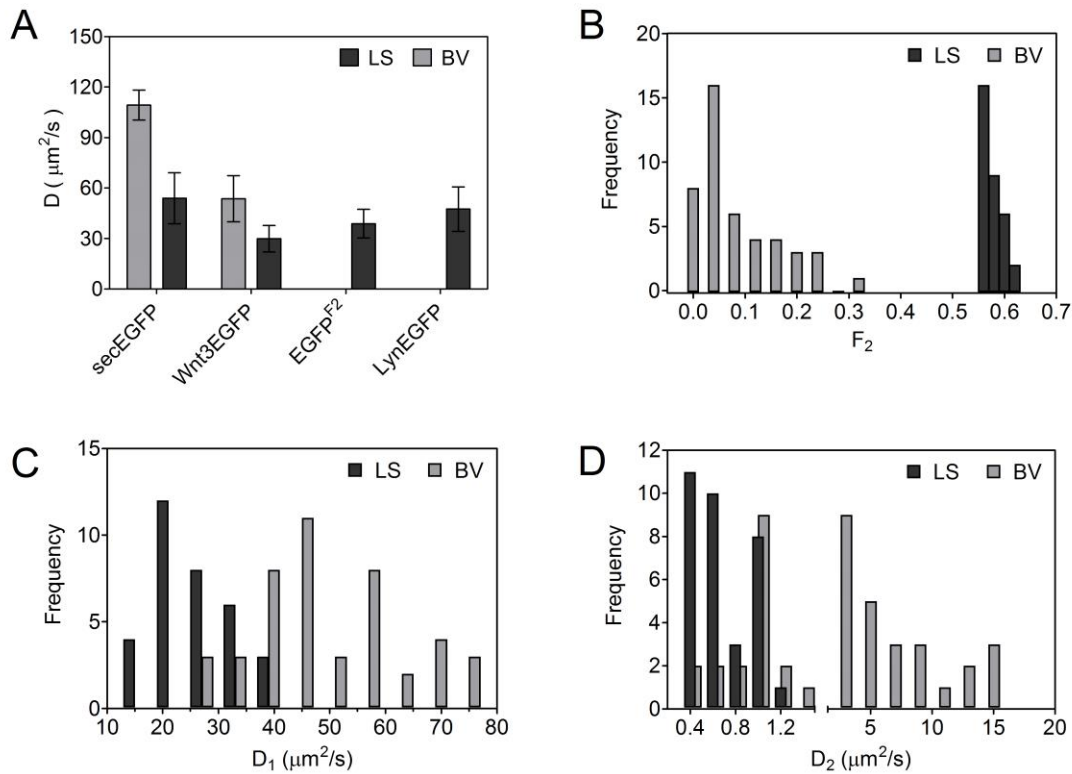


Figure 5.4 Wnt3EGFP extracellular and intercellular dynamics

(A) Protein mobility intercellularly (LS) and extracellularly (BV). secEGFP as an indicator of protein mobility intercellularly in multicellular tissue and extracellularly in the brain ventricle; EGFP^{F2} as an indicator of protein mobility intracellularly. (B) Fraction of slow moving component F_2 and (C and D) distribution of Wnt3EGFP diffusion coefficients D_1 and D_2 in the cerebellum lateral side (dark grey bars) and in the brain ventricle (light grey bars), showing the mobility / size heterogeneity of the slow moving Wnt3EGFP in the brain ventricle. LS: lateral side in the cerebellum; BV: brain ventricle. See also Table 5.2.

Table 5.2 Protein intracellular, intercellular and extracellular mobility

	34hpf	D or D_1 ($\mu\text{m}^2\text{s}^{-1}$)	Embryo No.	Total Point No.
Ce	Wnt3EGFP	29.70 ± 8.81	5	22
	secEGFP	53.97 ± 15.18	2	11
	EGFP ^{F2}	38.74 ± 8.54	3	30
	LynEGFP	47.42 ± 13.19	6	35
BV	Wnt3EGFP	53.62 ± 13.69	6	45
	secEGFP	125.82 ± 8.85	3	22

Data are mean \pm SD of the number of points measured. Ce: cerebellum; BV: brain ventricle.

5.2.4. C59 blocks Wnt3EGFP secretion

Next, a loss-of-function study is performed to see how Wnt3EGFP will be influenced when its secretion is blocked. To achieve this aim, the Porcupine (Porc) inhibitor Wnt-C59 (C59) was used (Proffitt, Madan et al. 2013). Porc, a membrane-bound O-acyl transferase, is necessary for Wnt lipid modification, correct anchoring in the cell membrane and signaling in Wnt-producing cell (details in Section 1.1.1, van den Heuvel, Harryman-Samos et al. 1993; Kadowaki, Wilder et al. 1996; Hofmann 2000). Porc is a highly conserved component of the Wnt pathway and is active only in Wnt producing cells (Clevers and Nusse 2012).

Experiments were performed on both Wnt3EGFP and LynEGFP. Zebrafish embryos were soaked with 5 μ M C59 1% DMSO solution for eight hours before the measurement (details see Section 2.2.3.4). A morphologically distinct cerebellum is absent in embryos treated with 5 μ M C59 (Fig. 5.5). This is consistent with the reported defective cerebellar fusion caused by decreased Wnt activity (Lancaster, Gopal et al. 2011). As shown by the confocal images in Fig. 5.5A and B, LynEGFP can still be expressed in the whole tissue, whereas Wnt3EGFP expression was seriously reduced.

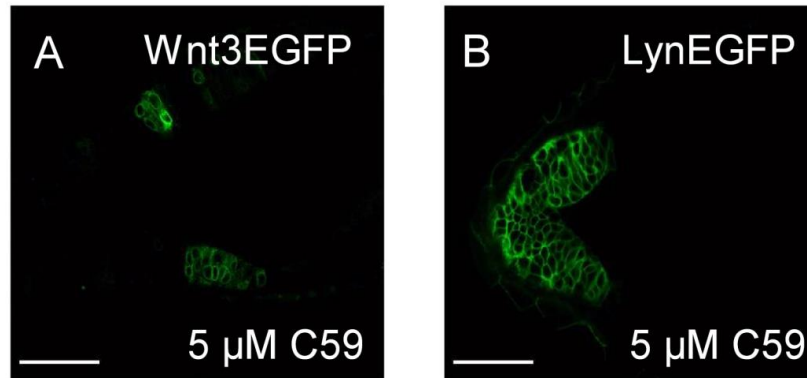


Figure 5.5 C59 treatment on Wnt3EGFP and LynEGFP

(A and B) Confocal images of zebrafish cerebellum expressing Wnt3EGFP and LynEGFP after C59 treatment. The embryos were treated with 5 μ M C59 for 8 h. The samples were then washed up using 1x egg water before taking images and FCS measurements. Images were taken in dorsal view. Scale bar, 50 μ m.

The X-scanning analysis confirmed that Wnt3EGFP secretion was reduced or blocked by C59. It can barely be secreted and transported to the brain ventricle under 5 μ M C59, indicated by its overlap with LynEGFP (Fig. 5.6A). In accordance with this, it can barely be detected by FCS in the brain ventricle. However, some large aggregation clusters were observed in the brain ventricle, shown as the peaks in the intensity profile (black solid line in Fig. 5.6A). FCS was then performed in the treated embryos. The results were plotted and compared with embryos under normal condition (non-treated) and 1% DMSO soaking condition (Fig. 5.6B-D). It was shown that neither LynEGFP nor Wnt3EGFP was affected in any way under 1% DMSO soaking. Especially for LynEGFP, mobility of both the fast and slow moving components (D_1 and D_2 , Fig. 5.6B and C) as well as its membrane fraction (F_2 , Fig. 5.6D) remained unchanged by the treatment. These results indicate that the plasma membrane property is not influenced by the treating procedure or the drug function. Therefore, the Wnt3EGFP response to this Porc inhibition C59 is specific. Its mobility on the membrane (D_2) increased 2 times compared to the non-treated one

and its membrane fraction dropped approximately by 15% (Fig. 5.6B and C). These results are consistent with the previous report on its decreasing hydrophobicity in the absence of Porc (Zhai, Chaturvedi et al. 2004). This is due to the missing lipid modification from the Porc blocking. With less lipid modifications, the anchored protein loses part of its lipid affinity to the membrane and thereby increases its mobility. On the other hand, such modification is necessary for Wnt to be recognized and transported by Wntless (Wls) from the Golgi to the membrane (Coombs, Yu et al. 2010; Herr and Basler 2012). Therefore, Porc inhibition causes the accumulation of Wnt3EGFP inside cells and thus less of the protein is localized on the membrane. But this phenomenon is not clear from the confocal imaging, since the nuclei occupies the most space in a cell and thus the accumulation in such limited space is not easily distinguished (Fig. 5.1C). It was also found out that no Wnt3EGFP can be detected in the brain ventricle (data not shown). This suggests that Porc is crucial in its secretion. It is worth noting that both the mobility (D_2) and the fraction (F_2) of membrane Wnt3EGFP vary over a large range, indicated by the larger standard deviations and histogram in Fig. 5.6E and F. A possible reason for this might be a differential uptake of Porc by different cells. However, the mobility of the fast moving component was not affected. This happens possibly because the transportation of Wnt3EGFP from ER to membrane is not entirely blocked under this concentration.

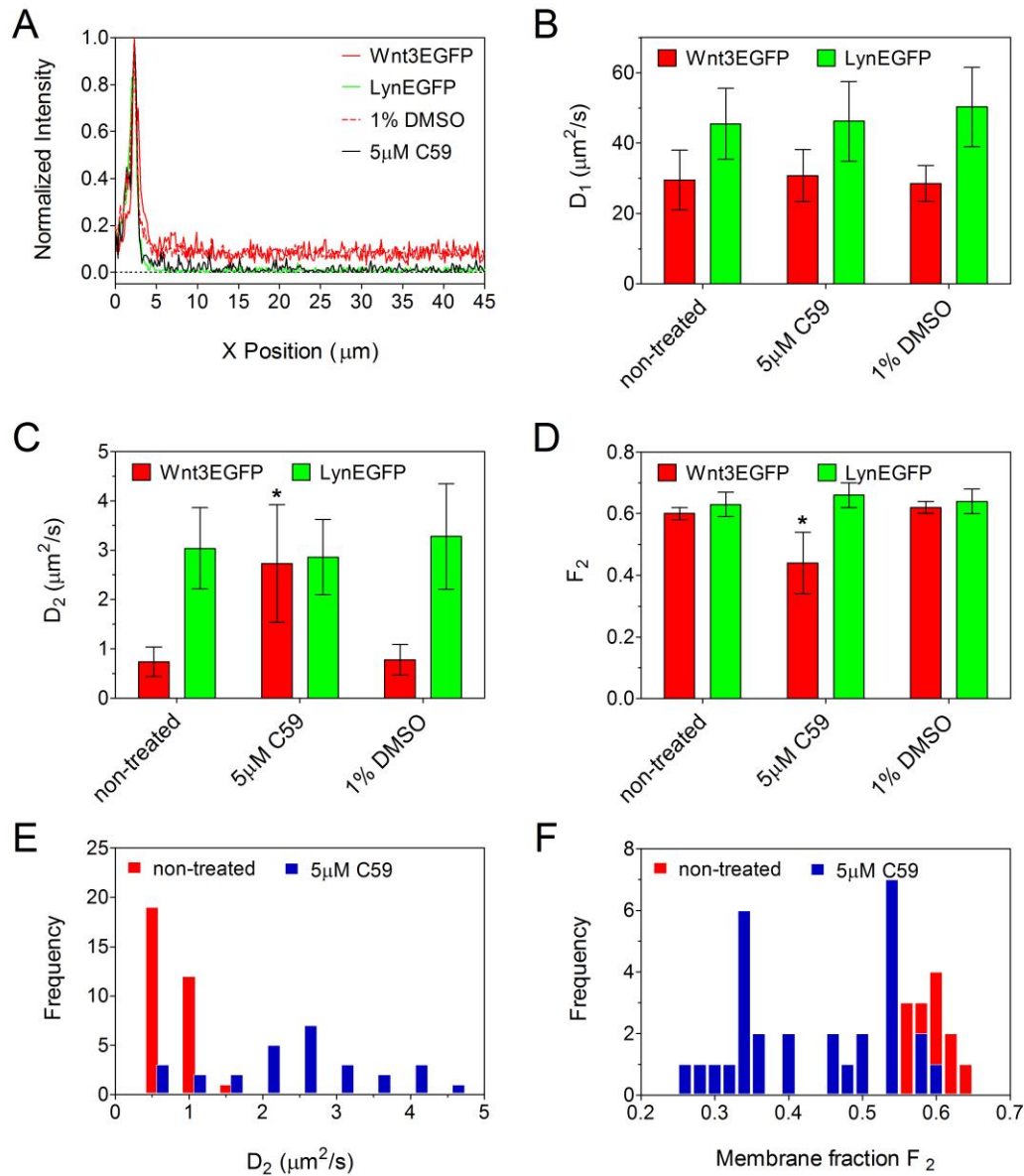


Figure 5.6 C59 treatment influences Wnt3EGFP but not LynEGFP

(A) Normalized intensity of Wnt3EGFP from the cerebellum boundary to the brain ventricle under 5 μM C59 treatment. Data for Wnt3EGFP are shown in red, LynEGFP in green, 1% DMSO control in blue, 5 μM C59 treatment in black. (B, C and D) Diffusion coefficients (D_1 , D_2) and protein membrane fraction (F_2) inferred from fit under different conditions for both Wnt3EGFP and LynEGFP. Data are mean \pm SD. Red bar, Wnt3EGFP. Green bar, LynEGFP. Significance level, two-way t-test, * $P < 0.001$. (E) Membrane mobility and (F) fraction histogram of Wnt3EGFP under different treatment conditions. Red bar, normal condition (non-treated); Blue bar, 5 μM C59 treatment. See also Table 5.3.

Table 5.3 Measurements on membrane for Wnt3EGFP and LynEGFP under 5 μ M C59 treatment

Species	Conditions	D_1 ($\mu\text{m}^2\text{s}^{-1}$)	D_2 ($\mu\text{m}^2\text{s}^{-1}$)	F_2 (%)	Total Embryo No.	Total Cell No.
Wnt3EGFP	5 μ M C59	30.80 ± 7.38	2.73 ± 1.19	44 ± 10	4	29
	1% DMSO	28.60 ± 5.01	0.78 ± 0.31	62 ± 2	1	8
LynEGFP	5 μ M C59	46.19 ± 11.34	2.86 ± 0.76	66 ± 4	3	24
	1% DMSO	50.26 ± 11.31	3.28 ± 1.07	64 ± 4	2	11

Data are mean \pm SD of number of cells measured.

5.3. Conclusion

In this chapter, FCS was employed to investigate Wnt3EGFP mobility in zebrafish brain development. It was found that Wnt3EGFP is located on the membrane and inside the cell, and it could be secreted from the cell and travel to the brain ventricle. The Wnt3EGFP membrane fraction and mobility did not change at different developmental stages, different regions or expression levels. The smaller membrane fraction of Wnt3EGFP compared to the non-functional LynEGFP indicates that only a small amount (about 5%) of Wnt3EGFP is in the intercellular space in the cerebellum to perform cell-to-cell communication by free diffusion. This is consistent with recent work on Decapentaplegic (Dpp) transportation in *Drosophila* larval wing disc, where it was shown that Dpp acted by a free transportation in the extracellular space with little Dpp needed (Zhou, Lo et al. 2012). In the case of Porc inhibition, Wnt3EGFP cannot be secreted and its mobility on the membrane increased.

Chapter 6

Conclusion and Outlook

6.1. Conclusion

In this study, Bayesian model selection was employed to determine the appropriate fitting model for commonly used fluorescent proteins under various experimental conditions. The basic principles of this approach were introduced in Chapter 3. The procedures from blocking transformation, noise estimation to model probabilities calculation were illustrated. In the experimental system, this Bayesian approach was able to distinguish the fast photo dynamic process and multiple diffusing components. This method provided an objective and effective evaluation of multiple competing models by ranking their probabilities.

The Bayesian analysis of organic dyes and fluorescent proteins data were then discussed in Chapter 4. The experiments were first performed in solution. It was shown that the model selection was sensitive to the excitation intensity. But models can be unambiguously identified under fixed and low excitation intensity conditions. With an increase in the excitation intensity, the triplet state population or blinking dynamics can be induced and thereby this process should be included in describing ACFs. Besides, the influence on model selection from acquisition time and experiment temperature was also examined. However, they barely affected the model selection.

This approach was then extended to its application in fluorescent proteins data *in vivo*. It was found that one-component free diffusion model was sufficient to describe their diffusion in cytoplasm and nucleus of CHO cells. The anomalous diffusion model was also examined. However, it was shown that this model was likely to be a substitute of one component with a triplet dynamic model but not reflected the diffusion pattern. For a membrane located protein, two-component diffusion model was selected, in which the slow moving component described the membrane-tethered protein movement and the fast moving component were free molecules attributed to the membrane dynamic internalization and endocytosis. Finally, this methodology was employed in the data evaluation for FCS measured in zebrafish embryos. All EGFP labeled proteins, in different cell compartments, were examined. The appropriate fitting models were then determined and used in the data analysis and interpretation. It was found that 2D-2p1t was appropriate for membrane located Wnt3EGFP and LynEGFP, whereas 3D-1p1t was selected for intracellular EGFP^{F2} and extracellular secreted secEGFP. In the case of secreted Wnt3EGFP in the brain ventricle, 3D-2p1t was selected.

Upon establishing the correct fitting protocol in the aforementioned chapters, the secretion of zebrafish Wnt3EGFP was investigated in Chapter 5. It was found that Wnt3EGFP located not only on the membrane but also inside the cell. Its membrane fraction and mobility were relatively stable as they did not change at different development stages, different regions or expression levels. It was also shown that a small amount of Wnt3EGFP could be secreted and transported to the brain ventricle. This transport process was observed to be a free diffusion from the Bayesian analysis of FCS data. Overall, the results indicate its ability to traverse a significant distance in intercellular space before reaching its target cells. Moreover, when Wnt family

conserved Porcupine (Porc) expression was inhibited by Wnt-C59 (C59), the secretion of Wnt3EGFP was blocked and thus it was accumulated inside the cell and could not be detected in the brain ventricle. At the same time, its mobility on the membrane increased due to the loss of palmitation. Moreover, the cerebellum growth was seriously affected due to reduced Wnt3EGFP secretion.

In summary, Bayesian analysis approach of FCS data was applied for the fluorescent proteins both *in vitro* and *in vivo* in the first part of the thesis. It has demonstrated a novel methodology to determine fitting models considering the correlated noise in the FCS data. This method therefore is able to resolve decade-long controversy of fitting FCS data in various kinds of complex situations. In view of its robustness, this method should be considered as a preliminary test for the data analysis. On the other hand, these *in vivo* results presented in this thesis demonstrate Wnt protein trafficking mechanism in zebrafish model. This study has provided valuable insight to understand the intercellular trafficking mechanism of zebrafish Wnt3 in brain development more clearly. These findings are significant since it could provide guidelines for the investigation of lipid modified secreted signaling proteins. In terms of the technique, this study extends the applications of FCS to address biological issues *in vivo*. Such *in vivo* applications of FCS are very sparsely reported in literature despite FCS is used very routinely *in vitro*.

6.2. Outlook

6.2.1. Bayesian model selection

The Bayesian model selection approach has been shown as an objective and convenient method in FCS data analysis. However, only data obtained from confocal FCS has been evaluated here. Recently, this methodology was adopted in imaging total internal reflection FCS (ITIR-FCS) to understand microdomain spatial

organization on the plasma membrane induced by human islet amyloid polypeptide (hIAPP) (Guo, Bag et al. 2014). Therefore, an extension of this work is to apply this approach on the FCS data obtained from different optical configurations, such as single-plane illumination FCS (SPIM-FCS, Wohland, Shi et al. 2010), spinning disk confocal FCS (Sisan, Arevalo et al. 2006; Needleman, Xu et al. 2009) and two-photon FCS (Berland, So et al. 1995), or even image correlation spectroscopy (ICS, Kolin and Wiseman 2007).

Besides the commonly used EGFP, EYFP and mCherry, various fluorescent proteins with improved properties have been introduced (Chudakov, Matz et al. 2010), such as super folder GFP (sfGFP) with increased thermal stability (Cotlet, Goodwin et al. 2006), Venus, a variant of yellow fluorescent protein with reduced chloride sensitivity and fast maturation (Nagai, Ibata et al. 2002), and mKate2 with fast maturation, high pH-stability and photostability (Shcherbo, Murphy et al. 2009). This Bayesian approach should be used in the FCS data analysis of these newly developed fluorescent proteins. Meanwhile, it is still uncertain whether different cell lines or animal models would show different results, since only CHO cell line and zebrafish cerebellum were investigated in this study. It is necessary to determine the appropriate fitting models for the chosen fluorescent proteins using Bayesian approach under experimental conditions.

6.2.2. Zebrafish Wnt3EGFP

First of all, this well-characterized zebrafish Wnt3EGFP in the cerebellum can be employed as an inhibition test platform. The aberrant expression of Wnt is generally related to degenerative diseases and cancer (Clevers and Nusse 2012; Anastas and Moon 2013). Two classes of compounds disrupting Wnt response have been identified. One class inhibits the activity of Porcupine, represented by Wnt-C59 (C59,

Proffitt, Madan et al. 2013; Wend, Runke et al. 2013; Stewart, Gomez et al. 2014). Another is the inhibitor of Wnt response (IWR), which suppresses Wnt/ β -catenin pathway activity (Lu, Ma et al. 2009; Chen, Dodge et al. 2009; Willems, Spiering et al. 2011; Bao, Christova et al. 2012). These small molecules are of great interest in molecular biology for their role in studying protein functions and regulations in biological processes. One advantage of small molecules is their ability to rapidly diffuse across cell membranes and reach intracellular sites of action. Some can inhibit or disrupt a specific function of a functional protein and thus lead to the development of new therapeutic agents.

The representatives of the two types, C59 and IWR1 were examined in the system. To examine the inhibition efficiency, various treatment concentrations were tested. Firstly, the confocal images showed the morphology change. At the lowest dose, 0.1 μ M C59, defective optic tectal closure indicated by the absence of the medial roof plate cells was observed in the treated embryos (Fig. 6.1B). A morphologically distinct cerebellum is absent in embryos treated with 0.5 μ M and 5 μ M C59 (Fig. 6.1C-D). The effect of IWR1 mediated Wnt inhibition on neural tube morphogenesis was milder than C59. Midline fusion defect in the optic tectum and cerebellum occurs at 50 μ M (Fig. 6.1H), the aqueous solubility limit of IWR1. Lower concentrations barely have an influence on the cerebellum morphology (Fig. 6.1F and G). Secondly, X-scanning analysis showed that Wnt3EGFP secretion was reduced by C59. Under lower treatment concentrations (dashed dark grey for 0.5 μ M and dotted light grey for 0.1 μ M in Fig. 6.2A), the intensity in the brain ventricle was slightly elevated but still reduced compared to the non-treated Wnt3EGFP and 1% DMSO control, but the reduction of these two is not distinguishable. This is due to the small amount of Wnt3EGFP secreted and consequently this small reduction cannot be shown by bulk

intensity analysis. On the contrary, the expression and secretion of Wnt3EGFP under IWR1 treatment was the same as that of the non-treated embryos (Figure 6.2B). The reason for this is that IWR1 only blocks the Wnt/ β -catenin pathway, which is either in Wnt3-receiving cells after secretion or in Wnt3-producing cells before secretion. Therefore, the secretion process was not hindered in any way up to 50 μ M IWR1. Thirdly, FCS demonstrated that Wnt3EGFP membrane mobility (D_2) increased and fraction (F_2) decreased in a concentration dependent manner as C59 concentration increased (Fig. 6.2C and D). The decreasing F_2 is consistent with the X-scanning analysis, indicating more Wnt3EGFP was prevented from being secreted from the cell. Consistent with the unaffected morphological change from confocal imaging and X-scanning analysis, Wnt3EGFP mobility and membrane fraction was not affected by IWR1 (Fig. 6.2C-F). In all the cases, the mobility of the fast moving component was not affected under various concentrations (Fig. 6.2E). Besides 5 μ M C59 treatment, Wnt3EGFP can be detected in the brain ventricle and keep the mobility unaffected (Fig. 6.2F). Data are also listed in Tables 6.1 and 6.2. In the future, this methodology combining both X-scanning imaging analysis and FCS signatures can be further applied in inhibitor test using this zebrafish Wnt3EGFP model.

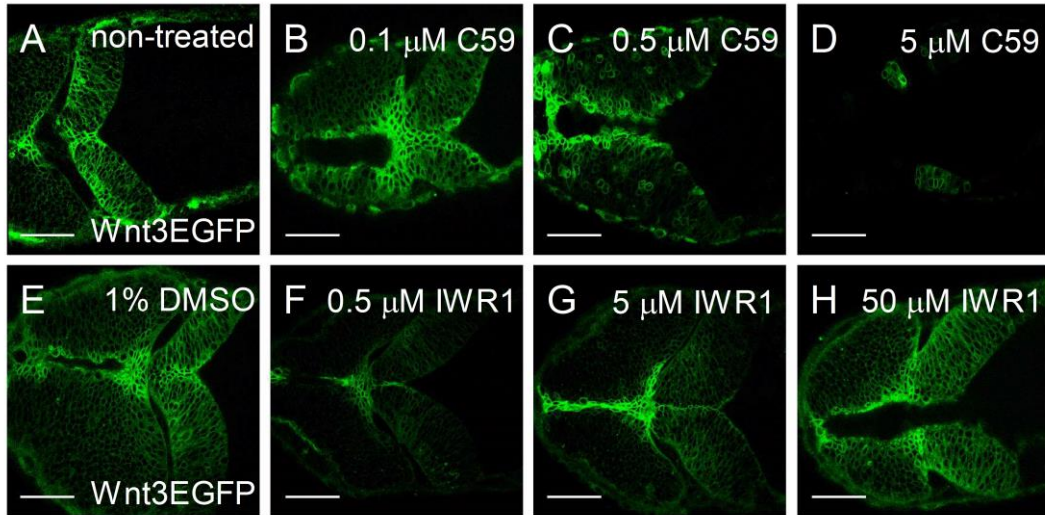


Figure 6.1 Dose dependent response of Wnt inhibitors

Confocal images of zebrafish cerebellum expressing Wnt3EGFP treated with C59 and IWR at various concentrations. (A) Non-treated embryo. This is illustrated in section 5.2.3 as figure 5.3A. (B - D) Embryos treated with different C59 soaking concentrations. Figure D is illustrated in Section 5.2.4 as figure 5.5A. (E) Embryo soaking in 1% DMSO as an experiment control. (F - H) Embryos treated with different IWR1 soaking concentrations. The results show the dose dependent morphological response of the cerebellum to C59 treatment. On the contrary, IWR shows almost no influence to the cerebellum development. Images were taken in dorsal view. Scale bar, 50 μm .

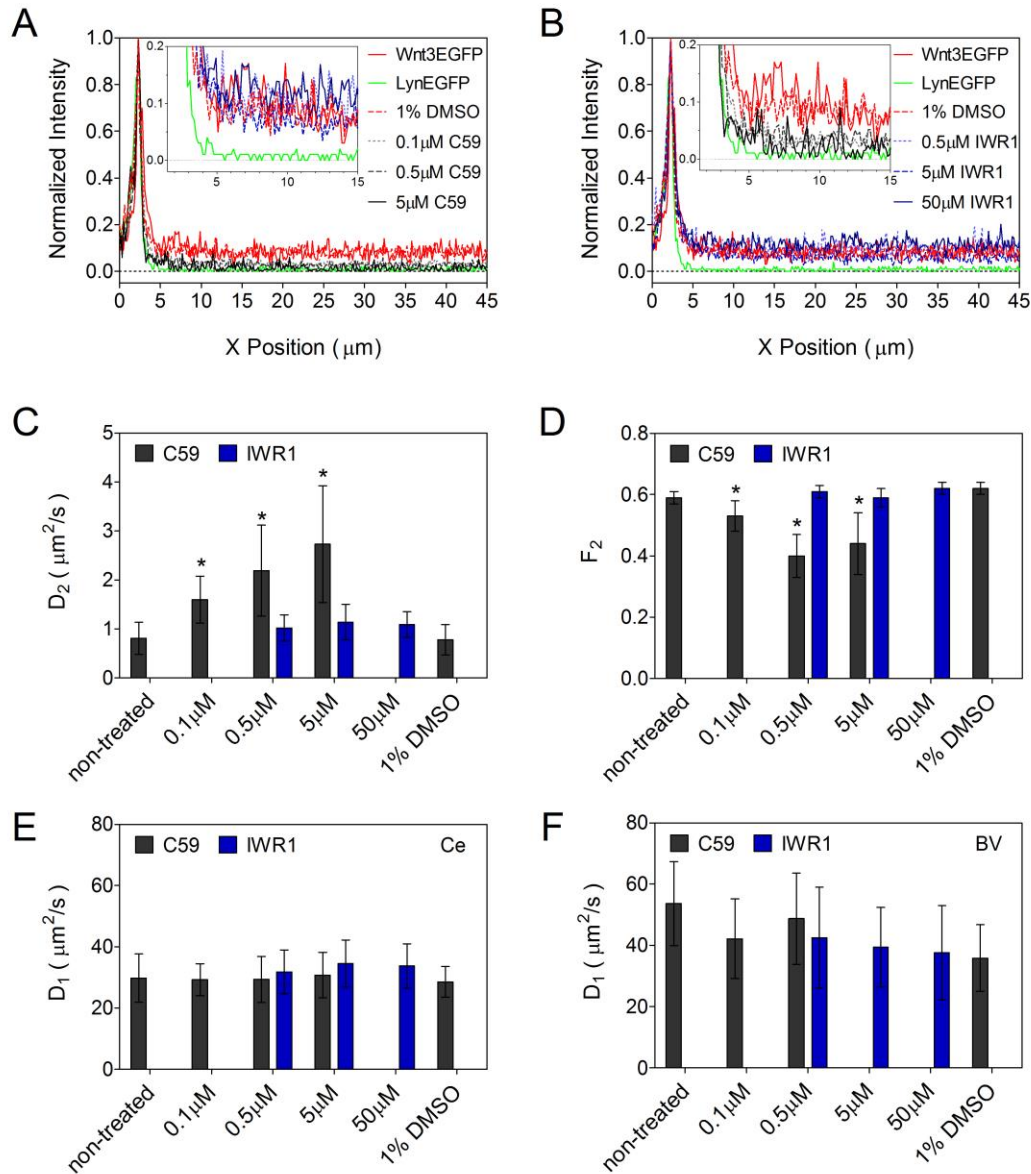


Figure 6.2 Effect of different doses of C59 and IWR1 on Wnt3EGFP secretion, membrane mobility and fraction

(A and B) Normalized intensity of Wnt3EGFP from the cerebellum boundary to the brain ventricle under (A) C59 treatment and (B) IWR1 treatment with various tested concentrations. Data for Wnt3EGFP are shown in red, LynEGFP in green, 1% DMSO control in blue, C59 treatment with concentrations from high to low in black, dashed dark grey and dotted light grey, IWR treatment with concentrations from high to low in dark blue, dashed blue and dotted light blue. Data are the average of three scans of three embryos for each condition. Insets show same profile but on different scale. (C and D) FCS signatures of Wnt3EGFP dynamics: (C) membrane mobility D_2 and (D) membrane fraction F_2 show a dose dependent change for the effective drug C59. (E and F) Mobility of the fast moving component in the (E) cerebellum and (F) brain ventricle. Data are mean \pm SD. Dark grey bar, C59. Dark blue bar, IWR1. Significance level, two-way t-test, * $P < 0.001$. See also Tables 6.1 and 6.2.

Table 6.1 Measurements on membrane for Wnt3EGFP at different treatment conditions

Wnt3EGFP in the Cerebellum		$D_1 (\mu\text{m}^2\text{s}^{-1})$	$D_2 (\mu\text{m}^2\text{s}^{-1})$	$F_2 (\%)$	Total Embryo No.	Total Cell No.
C59 treatment	0.1 μM	29.29 ± 5.24	1.60 ± 0.48	53 ± 5	3	24
	0.5 μM	29.36 ± 7.49	2.19 ± 0.93	40 ± 7	3	24
	5 μM	30.80 ± 7.38	2.73 ± 1.19	44 ± 10	4	29
IWR1 treatment	0.5 μM	31.87 ± 7.10	1.02 ± 0.27	61 ± 2	3	25
	5 μM	34.62 ± 7.66	1.14 ± 0.36	59 ± 3	3	18
	50 μM	33.79 ± 7.20	1.09 ± 0.26	62 ± 2	2	17

Data are mean \pm SD of number of cells measured.

Table 6.2 Measurements in the brain ventricle for Wnt3EGFP at different treatment conditions

Wnt3EGFP in the BV		$D_1 (\mu\text{m}^2\text{s}^{-1})$	Total Embryo No.	Total Cell No.
Non treated		53.62 ± 13.69	6	45
C59 treatment	0.1 μM	42.25 ± 12.98	5	37
	0.5 μM	48.76 ± 14.85	3	18
	5 μM	-	-	-
IWR1 treatment	0.5 μM	42.60 ± 16.43	3	29
	5 μM	39.50 ± 12.94	3	28
	50 μM	37.63 ± 15.42	3	28
1% DMSO		35.91 ± 10.81	3	24

Data are mean \pm SD of number of points measured. BV: brain ventricle.

Moreover, it is acknowledged that this study did only a preliminary analysis on the Wnt3 trafficking mechanism in zebrafish. Firstly, the interactions of Wnt3 with its receptors or proteins in the extracellular matrix have not been investigated. For example, the Frizzled (Fz) family has been reported to be a specific membrane receptor for the Wnt family (Piddini, Marshall et al. 2005). When blocking the receptors, the Wnt3 membrane fraction of the signaling receiving cells should

decrease. From previous study, heparan sulphate proteoglycan (HSPG), an extracellular matrix component, has been reported to interact with some signaling proteins and be required for their transportation (Baeg, Selva et al. 2004). With the decrease of HSPG in the extracellular matrix, it may increase the Wnt3 membrane fraction by blocking its transportation. Therefore, future research should attempt to address how these factors would affect the Wnt3 membrane fraction and its mobility. On the other hand, the interaction between Wnt3 and the receptors and the transporters should be investigated to further confirm the possible transportation mechanism described in Section 1.1.3. These studies can be achieved by an extension of FCS, fluorescence cross correlation spectroscopy (FCCS). In FCCS, the interacted two species are labeled with two spectrally distinct fluorophores, usually green and red, which can be excited either by different lasers (Schwille, MeyerAlmes et al. 1997) or by a single laser (Hwang and Wohland 2005). Signals are collected in two separated detection channels for each label. Then the correlation between green and red channel signal are correlated instead of the time shifted replica in ACF. In the case of interaction, the two differently labeled molecules will move through the observation volume together, leading to simultaneous fluctuations of the fluorescence signals in the two channels. The information about the complexes formed between two species can be inferred from the analysis of cross-correlation function (CCF) of the signals. The dissociation constant can then be calculated from the fitting parameters.

Another promising area for future research is to use SPIM-FCS to directly monitor cell-to-cell communication to achieve the information on transportation direction or the cargo exchange dynamics. In SPIM, a thin light sheet is created in the focal plane for optically sectioned imaging with high resolution and reduced photo-toxicity

(Huisken, Swoger et al. 2004; Verveer, Swoger et al. 2007). It is of great help in 3D sample illumination. SPIM-FCS provides diffusion coefficients, concentrations, flow velocities in an imaging mode. Compared to the point measurement in confocal FCS, many more measurements are simultaneously taken in the whole illumination plane, which not only greatly reduces the measurement time but also provides a comprehensive view of the area of interest. This method has been reported to measure the diffusion of injected microspheres in the blood circulation system in living zebrafish embryos (Wohland, Shi et al. 2010). Therefore, it is worthwhile to employ this method in Wnt3 signaling study in the future.

Bibliography

- Abu-Arish A, Porcher A, Czerwonka A, Dostatni N, Fradin C: **High Mobility of Bicoid Captured by Fluorescence Correlation Spectroscopy: Implication for the Rapid Establishment of Its Gradient.** *Biophys J* 2010, **99**(4):L33-L35.
- Anastas JN, Moon RT: **WNT signalling pathways as therapeutic targets in cancer.** *Nature Reviews Cancer* 2013, **13**(1):11-26.
- Anne SL, Govek EE, Ayrault O, Kim JH, Zhu XD, Murphy DA, Van Aelst L, Roussel MF, Hatten ME: **WNT3 Inhibits Cerebellar Granule Neuron Progenitor Proliferation and Medulloblastoma Formation via MAPK Activation.** *PLoS One* 2013, **8**(11).
- Aragón SR, Pecora R: **Fluorescence correlation spectroscopy as a probe of molecular dynamics.** *J Chem Phys* 1976, **64**(4):1791-1803.
- Arrese EL, Canavoso LE, Jouni ZE, Pennington JE, Tsuchida K, Wells MA: **Lipid storage and mobilization in insects: current status and future directions.** *Insect Biochem Mol Biol* 2001, **31**(1):7-17.
- Baeg GH, Selva EM, Goodman RM, Dasgupta R, Perrimon N: **The wingless morphogen gradient is established by the cooperative action of Frizzled and Heparan Sulfate Proteoglycan receptors.** *Dev Biol* 2004, **276**(1):89-100.
- Banziger C, Soldini D, Schutt C, Zipperlen P, Hausmann G, Basler K: **Wntless, a conserved membrane protein dedicated to the secretion of Wnt proteins from signaling cells.** *Cell* 2006, **125**(3):509-522.
- Bao RY, Christova T, Song SY, Angers S, Yan XJ, Attisano L: **Inhibition of Tankyrases Induces Axin Stabilization and Blocks Wnt Signalling in Breast Cancer Cells.** *PLoS One* 2012, **7**(11).
- Bartscherer K, Pelte N, Ingelfinger D, Boutros M: **Secretion of Wnt Ligands requires Evi, a conserved transmembrane protein.** *Cell* 2006, **125**(3):523-533.
- Bejsovec A, Wieschaus E: **Signaling Activities of the Drosophila Wingless Gene Are Separately Mutable and Appear to Be Transduced at the Cell Surface.** *Genetics* 1995, **139**(1):309-320.
- Belenkaya TY, Wu YH, Tang XF, Zhou B, Cheng LQ, Sharma YV, Yan D, Selva EM, Lin XH: **The retromer complex influences Wnt secretion by recycling Wntless from endosomes to the trans-Golgi network.** *Dev Cell* 2008, **14**(1):120-131.
- Benda A, Benes M, Marecek V, Lhotsky A, Hermens WT, Hof M: **How to determine diffusion coefficients in planar phospholipid systems by confocal fluorescence correlation spectroscopy.** *Langmuir* 2003, **19**(10):4120-4126.
- Berland KM, So PTC, Gratton E: **Two-photon fluorescence correlation spectroscopy: method and application to the intracellular environment.** *Biophys J* 1995, **68**(2):694-701.
- Bhanot P, Brink M, Samos CH, Hsieh JC, Wang YS, Macke JP, Andrew D, Nathans J, Nusse R: **A new member of the frizzled family from Drosophila functions as a Wingless receptor.** *Nature* 1996, **382**(6588):225-230.
- Bischoff M, Gradilla A-C, Seijo I, Andrés G, Rodríguez-Navas C, González-Méndez L, Guerrero I: **Cytonemes are required for the establishment of a normal Hedgehog morphogen gradient in Drosophila epithelia.** *Nat Cell Biol* 2013, **15**(11):1269-1281.

- Blader P, Strähle U, Ingham PW: **Three Wnt genes expressed in a wide variety of tissues during development of the zebrafish, *Danio rerio*: developmental and evolutionary perspectives.** *Development genes and evolution* 1996, **206**(1):3-13.
- Bouchaud JP, Georges A: **Anomalous diffusion in disordered media: Statistical mechanisms, models and physical applications.** *Physics Reports-Review Section of Physics Letters* 1990, **195**(4-5):127-293.
- Braun K, Peschke P, Pipkorn R, Lampel S, Wachsmuth M, Waldeck W, Friedrich E, Debus J: **A biological transporter for the delivery of peptide nucleic acids (PNAs) to the nuclear compartment of living cells.** *J Mol Biol* 2002, **318**(2):237-243.
- Briddon SJ, Middleton RJ, Yates AS, George MW, Kellam B, Hill SJ: **Application of fluorescence correlation spectroscopy to the measurement of agonist binding to a G-protein coupled receptor at the single cell level.** *Faraday Discuss* 2004, **126**:197-207.
- Brock R, Hink MA, Jovin TM: **Fluorescence correlation microscopy of cells in the presence of autofluorescence.** *Biophys J* 1998, **75**(5):2547-2557.
- Bronson JE, Fei JY, Hofman JM, Gonzalez RL, Wiggins CH: **Learning Rates and States from Biophysical Time Series: A Bayesian Approach to Model Selection and Single-Molecule FRET Data.** *Biophys J* 2009, **97**(12):3196-3205.
- Buechling T, Boutros M: **Wnt Signaling: at and above the Receptor Level.** In: *Growth Factors in Development. Volume 97*, edn. Edited by Birchmeier C. San Diego: Elsevier Academic Press Inc; 2011: 21-53.
- Burns AR, Frankel DJ, Buranda T: **Local mobility in lipid domains of supported bilayers characterized by atomic force microscopy and fluorescence correlation spectroscopy.** *Biophys J* 2005, **89**(2):1081-1093.
- Chalfie M, Tu Y, Euskirchen G, Ward WW, Prasher DC: **Green fluorescent protein as a marker for gene expression.** *Science* 1994, **263**(5148):802-805.
- Chapple JP, Hardcastle AJ, Grayson C, Willison KR, Cheetham ME: **Delineation of the plasma membrane targeting domain of the X-linked retinitis pigmentosa protein RP2.** *Invest Ophthalmol Vis Sci* 2002, **43**(6):2015-2020.
- Chen BZ, Dodge ME, Tang W, Lu JM, Ma ZQ, Fan CW, Wei SG, Hao WN, Kilgore J, Williams NS *et al*: **Small molecule-mediated disruption of Wnt-dependent signaling in tissue regeneration and cancer.** *Nat Chem Biol* 2009, **5**(2):100-107.
- Chen HM, Rhoades E, Butler JS, Loh SN, Webb WW: **Dynamics of equilibrium structural fluctuations of apomyoglobin measured by fluorescence correlation spectroscopy.** *Proc Natl Acad Sci U S A* 2007, **104**(25):10459-10464.
- Chen MH, Li YJ, Kawakami T, Xu SM, Chuang PT: **Palmitoylation is required for the production of a soluble multimeric Hedgehog protein complex and long-range signaling in vertebrates.** *Genes Dev* 2004, **18**(6):641-659.
- Chen Y, Muller JD, Ruan QQ, Gratton E: **Molecular brightness characterization of EGFP in vivo by fluorescence fluctuation spectroscopy.** *Biophys J* 2002, **82**(1):133-144.
- Ching W, Hang HC, Nusse R: **Lipid-independent secretion of a *Drosophila* Wnt protein.** *J Biol Chem* 2008, **283**(25):17092-17098.
- Chudakov DM, Matz MV, Lukyanov S, Lukyanov KA: **Fluorescent Proteins and Their Applications in Imaging Living Cells and Tissues.** *Physiol Rev* 2010, **90**(3):1103-1163.
- Clements WK, Ong KG, Traver D: **Zebrafish *wnt3* Is Expressed in Developing Neural Tissue.** *Dev Dyn* 2009, **238**(7):1788-1795.

- Clevers H: **Wnt/beta-catenin signaling in development and disease.** *Cell* 2006, **127**(3):469-480.
- Clevers H, Nusse R: **Wnt/beta-Catenin Signaling and Disease.** *Cell* 2012, **149**(6):1192-1205.
- Coombs GS, Yu J, Canning CA, Veltri CA, Covey TM, Cheong JK, Utomo V, Banerjee N, Zhang ZH, Jadulco RC *et al*: **WLS-dependent secretion of WNT3A requires Ser209 acylation and vacuolar acidification.** *Journal of Cell Science* 2010, **123**(19):3357-3367.
- Cotlet M, Goodwin PM, Waldo GS, Werner JH: **A comparison of the fluorescence dynamics of single molecules of a green fluorescent protein: One- versus two-photon excitation.** *Chemphyschem* 2006, **7**(1):250-260.
- Coudreuse DYM, Roel G, Betist MC, Destree O, Korswagen HC: **Wnt gradient formation requires retromer function in Wnt-producing cells.** *Science* 2006, **312**(5775):921-924.
- Cox S, Rosten E, Monypenny J, Jovanovic-Talisman T, Burnette DT, Lippincott-Schwartz J, Jones GE, Heintzmann R: **Bayesian localization microscopy reveals nanoscale podosome dynamics.** *Nat Methods* 2012, **9**(2):195-200.
- Coyle DE, Li J, Baccei M: **Regional Differentiation of Retinoic Acid-Induced Human Pluripotent Embryonic Carcinoma Stem Cell Neurons.** *PLoS One* 2011, **6**(1).
- Culbertson CT, Jacobson SC, Ramsey JM: **Diffusion coefficient measurements in microfluidic devices.** *Talanta* 2002, **56**(2):365-373.
- Daniel DC, Thompson M, Woodbury NW: **DNA-binding interactions and conformational fluctuations of Tc3 transposase DNA binding domain examined with single molecule fluorescence spectroscopy.** *Biophys J* 2002, **82**(3):1654-1666.
- Delon A, Usson Y, Derouard J, Biben T, Souchier C: **Continuous photobleaching in vesicles and living cells: A measure of diffusion and compartmentation.** *Biophys J* 2006, **90**(7):2548-2562.
- Dempster AP: **A Generalization of Bayesian Inference.** *Journal of the Royal Statistical Society Series B-Statistical Methodology* 1968, **30**(2):205-&.
- Dertinger T, Ewers B: *Unpublished results* 2008:PicoQuant GmbH.
- Dross N, Spriet C, Zwerger M, Muller G, Waldeck W, Langowski J: **Mapping eGFP Oligomer Mobility in Living Cell Nuclei.** *PLoS One* 2009, **4**(4).
- Eggeling C, Berger S, Brand L, Fries JR, Schaffer J, Volkmer A, Seidel CAM: **Data registration and selective single-molecule analysis using multi-parameter fluorescence detection.** *J Biotechnol* 2001, **86**(3):163-180.
- Eigen M, Rigler R: **Sorting single molecules: application to diagnostics and evolutionary biotechnology.** *Proc Natl Acad Sci U S A* 1994, **91**(13):5740-5747.
- Elson EL, Magde D: **Fluorescence correlation spectroscopy. I. Conceptual basis and theory.** *Biopolymers* 1974, **13**(1):1-27.
- Enderlein J, Gregor I, Patra D, Fitter J: **Art and artefacts of fluorescence correlation spectroscopy.** *Curr Pharm Biotechnol* 2004, **5**(2):155-161.
- Enderlein J, Gregor I, Patra D, Fitter J: **Statistical analysis of diffusion coefficient determination by fluorescence correlation spectroscopy.** *J Fluoresc* 2005, **15**(3):415-422.
- Esteve P, Sandonis A, Ibanez C, Shimono A, Guerrero I, Bovolenta P: **Secreted frizzled-related proteins are required for Wnt/beta-catenin signalling activation in the vertebrate optic cup.** *Development* 2011, **138**(19):4179-4184.

- Feder TJ, Brust-Mascher I, Slattery JP, Baird B, Webb WW: **Constrained diffusion or immobile fraction on cell surfaces: A new interpretation.** *Biophys J* 1996, **70**(6):2767-2773.
- Flyvbjerg H, Petersen HG: **Error estimates on averages of correlated data** *J Chem Phys* 1989, **91**(1):461-466.
- Foo YH, Naredi-Rainer N, Lamb DC, Ahmed S, Wohland T: **Factors Affecting the Quantification of Biomolecular Interactions by Fluorescence Cross-Correlation Spectroscopy.** *Biophys J* 2012, **102**(5):1174-1183.
- Franch-Marro X, Wendler F, Griffith J, Maurice MM, Vincent JP: **In vivo role of lipid adducts on Wingless.** *Journal of Cell Science* 2008, **121**(10):1587-1592.
- Franch-Marro X, Wendler F, Guidato S, Griffith J, Baena-Lopez A, Itasaki N, Maurice MM, Vincent JP: **Wingless secretion requires endosome-to-Golgi retrieval of Wntless/Evi/Sprinter by the retromer complex.** *Nat Cell Biol* 2008, **10**(2):170-U140.
- Galli LM, Barnes TL, Secret SS, Kadowaki T, Burrus LW: **Porcupine-mediated lipid-modification regulates the activity and distribution of Wnt proteins in the chick neural tube.** *Development* 2007, **134**(18):3339-3348.
- Garriock RJ, Warkman AS, Meadows SM, D'Agostino S, Krieg PA: **Census of vertebrate Wnt genes: Isolation and developmental expression of Xenopus Wnt2, Wnt3, Wnt9a, Wnt9b, Wnt10a, and Wnt16.** *Dev Dyn* 2007, **236**(5):1249-1258.
- Gennerich A, Schild D: **Fluorescence correlation spectroscopy in small cytosolic compartments depends critically on the diffusion model used.** *Biophys J* 2000, **79**(6):3294-3306.
- Goetz JA, Singh S, Suber LM, Kull FJ, Robbins DJ: **A highly conserved amino-terminal region of sonic hedgehog is required for the formation of its freely diffusible multimeric form.** *J Biol Chem* 2006, **281**(7):4087-4093.
- Goodman RM, Thombre S, Firtina Z, Gray D, Betts D, Roebuck J, Spana EP, Selva EM: **Sprinter: a novel transmembrane protein required for Wg secretion and signaling.** *Development* 2006, **133**(24):4901-4911.
- Gregory PC: **Bayesian Logical Data Analysis for the Physical Sciences: A Comparative Approach with Mathematica Support.** New York: Cambridge University Press; 2005.
- Gross JC, Chaudhary V, Bartscherer K, Boutros M: **Active Wnt proteins are secreted on exosomes.** *Nat Cell Biol* 2012, **14**(10):1036-1045.
- Guo SM, He J, Monnier N, Sun GY, Wohland T, Bathe M: **Bayesian Approach to the Analysis of Fluorescence Correlation Spectroscopy Data II: Application to Simulated and In Vitro Data.** *Anal Chem* 2012, **84**(9):3880-3888.
- Guo SM, Bag N, Mishra A, Wohland T, Bathe M: **Bayesian Total Internal Reflection Fluorescence Correlation Spectroscopy Reveals hIAPP-Induced Plasma Membrane Domain Organization in Live Cells.** *Biophys J* 2014, **106**(1):190-200.
- Haas P, Gilmour D: **Chemokine signaling mediates self-organizing tissue migration in the zebrafish lateral line.** *Dev Cell* 2006, **10**(5):673-680.
- Hac AE, Seeger HM, Fidorra M, Heimburg T: **Diffusion in two-component lipid membranes - A fluorescence correlation spectroscopy and Monte Carlo simulation study.** *Biophys J* 2005, **88**(1):317-333.
- Han C, Yan D, Belenkaya TY, Lin XJ: **Drosophila glypicans Dally and Dally-like shape the extracellular Wingless morphogen gradient in the wing disc.** *Development* 2005, **132**(4):667-679.

- Haupts U, Maiti S, Schwille P, Webb WW: **Dynamics of fluorescence fluctuations in green fluorescent protein observed by fluorescence correlation spectroscopy.** *Proc Natl Acad Sci U S A* 1998, **95**(23):13573-13578.
- He J, Guo SM, Bathe M: **Bayesian Approach to the Analysis of Fluorescence Correlation Spectroscopy Data I: Theory.** *Anal Chem* 2012, **84**(9):3871-3879.
- Heikal AA, Hess ST, Baird GS, Tsien RY, Webb WW: **Molecular spectroscopy and dynamics of intrinsically fluorescent proteins: Coral red (dsRed) and yellow (Citrine).** *Proc Natl Acad Sci U S A* 2000, **97**(22):11996-12001.
- Hendrix J, Flors C, Dedecker P, Hofkens J, Engelborghs Y: **Dark states in monomeric red fluorescent proteins studied by fluorescence correlation and single molecule spectroscopy.** *Biophys J* 2008, **94**(10):4103-4113.
- Herr P, Basler K: **Porcupine-mediated lipidation is required for Wnt recognition by Wls.** *Dev Biol* 2012, **361**(2):392-402.
- Hess ST, Webb WW: **Focal volume optics and experimental artifacts in confocal fluorescence correlation spectroscopy.** *Biophys J* 2002, **83**(4):2300-2317.
- Hillesheim LN, Chen Y, Muller JD: **Dual-color photon counting histogram analysis of mRFP1 and EGFP in living cells.** *Biophys J* 2006, **91**(11):4273-4284.
- Hofmann K: **A superfamily of membrane-bound O-acyltransferases with implications for Wnt signaling.** *Trends Biochem Sci* 2000, **25**(3):111-112.
- Hsieh JC, Rattner A, Smallwood PM, Nathans J: **Biochemical characterization of Wnt-Frizzled interactions using a soluble, biologically active vertebrate Wnt protein.** *Proc Natl Acad Sci U S A* 1999, **96**(7):3546-3551.
- Hsiung F, Ramirez-Weber FA, Iwaki DD, Kornberg TB: **Dependence of Drosophila wing imaginal disc cytonemes on decapentaplegic.** *Nature* 2005, **437**(7058):560-563.
- Huisken J, Swoger J, Del Bene F, Wittbrodt J, Stelzer EHK: **Optical sectioning deep inside live embryos by selective plane illumination microscopy.** *Science* 2004, **305**(5686):1007-1009.
- Hwang LC, Wohland T: **Single wavelength excitation fluorescence cross-correlation spectroscopy with spectrally similar fluorophores: Resolution for binding studies.** *J Chem Phys* 2005, **122**(11).
- Ishikawa-Ankerhold HC, Ankerhold R, Drummen GPC: **Advanced Fluorescence Microscopy Techniques-FRAP, FLIP, FLAP, FRET and FLIM.** *Molecules* 2012, **17**(4):4047-4132.
- Kadowaki T, Wilder E, Klingensmith J, Zachary K, Perrimon N: **The segment polarity gene porcupine encodes a putative multitransmembrane protein involved in Wingless processing.** *Genes Dev* 1996, **10**(24):3116-3128.
- Kahya N, Scherfeld D, Bacia K, Poolman B, Schwille P: **Probing lipid mobility of raft-exhibiting model membranes by fluorescence correlation spectroscopy.** *J Biol Chem* 2003, **278**(30):28109-28115.
- Kask P, Gunther R, Axhausen P: **Statistical accuracy in fluorescence fluctuation experiments.** *European Biophysics Journal with Biophysics Letters* 1997, **25**(3):163-169.
- Katoh M: **Regulation of WNT3 and WNT3A mRNAs in human cancer cell lines NT2, MCF-7, and MKN45.** *Int J Oncol* 2002, **20**(2):373-377.
- Katoh M: **WNT signaling pathway and stem cell signaling network.** *Clin Cancer Res* 2007, **13**(14):4042-4045.
- Kaur G, Costa MW, Nefzger CM, Silva J, Fierro-Gonzalez JC, Polo JM, Bell TDM, Plachta N: **Probing transcription factor diffusion dynamics in the living mammalian**

- embryo with photoactivatable fluorescence correlation spectroscopy. *Nature Communications* 2013, **4**.**
- Kawakami K: **Tol2: a versatile gene transfer vector in vertebrates.** *Genome Biol* 2007, **8**.
- Kestler HA, Kuhl M: **From individual Wnt pathways towards a Wnt signalling network.** *Philosophical Transactions of the Royal Society B-Biological Sciences* 2008, **363**(1495):1333-1347.
- Kimmel CB, Ballard WW, Kimmel SR, Ullmann B, Schilling TF: **Stages of embryonic development of the zebrafish.** *Dev Dyn* 1995, **203**(3):253-310.
- Kinjo M, Rigler R: **Ultrasensitive hybridization analysis using fluorescence correlation spectroscopy.** *Nucleic Acids Res* 1995, **23**(10):1795-1799.
- Kolin DL, Wiseman PW: **Advances in image correlation spectroscopy: Measuring number densities, aggregation states, and dynamics of fluorescently labeled macromolecules in cells.** *Cell Biochem Biophys* 2007, **49**(3):141-164.
- Komekado H, Yamamoto H, Chiba T, Kikuchi A: **Glycosylation and palmitoylation of Wnt-3a are coupled to produce an active form of Wnt-3a.** *Genes Cells* 2007, **12**(4):521-534.
- Kondrychyn I, Teh C, Garcia-Lecea M, Guan YX, Kang A, Korzh V: **Zebrafish Enhancer TRAP Transgenic Line Database ZETRAP 2.0.** *Zebrafish* 2011, **8**(4):181-182.
- Koppel DE: **Statistical accuracy in fluorescence correlation spectroscopy.** *Phys Rev A* 1974, **10**(6):1938-1945.
- Koppel DE, Axelrod D, Schlessinger J, Elson EL, Webb WW: **Dynamics of fluorescence marker concentration as a probe of mobility.** *Biophys J* 1976, **16**(11):1315-1329.
- Korlach J, Schwille P, Webb WW, Feigensohn GW: **Characterization of lipid bilayer phases by confocal microscopy and fluorescence correlation spectroscopy.** *Proc Natl Acad Sci U S A* 1999, **96**(15):8461-8466.
- Kral T, Langner M, Benes M, Baczynska D, Ugorski M, Hof M: **The application of fluorescence correlation spectroscopy in detecting DNA condensation.** *Biophys Chem* 2002, **95**(2):135-144.
- Krauss S, Korzh V, Fjose A, Johansen T: **Expression of four zebrafish wnt-related genes during embryogenesis.** *Development* 1992, **116**(1):249-259.
- Kurayoshi M, Yamamoto H, Izumi S, Kikuchi A: **Post-translational palmitoylation and glycosylation of Wnt-5a are necessary for its signalling.** *Biochem J* 2007, **402**:515-523.
- Lancaster MA, Gopal DJ, Kim J, Saleem SN, Silhavy JL, Louie CM, Thacker BE, Williams Y, Zaki MS, Gleeson JG: **Defective Wnt-dependent cerebellar midline fusion in a mouse model of Joubert syndrome.** *Nat Med* 2011, **17**(6):726-U119.
- Lieschke GJ, Currie PD: **Animal models of human disease: zebrafish swim into view.** *Nature Reviews Genetics* 2007, **8**(5):353-367.
- Liu P, Sudhakaran T, Koh RML, Hwang LC, Ahmed S, Maruyama IN, Wohland T: **Investigation of the dimerization of proteins from the epidermal growth factor receptor family by single wavelength fluorescence cross-correlation spectroscopy.** *Biophys J* 2007, **93**(2):684-698.
- Liu PT, Wakamiya M, Shea MJ, Albrecht U, Behringer RR, Bradley A: **Requirement for Wnt3 in vertebrate axis formation.** *Nat Genet* 1999, **22**(4):361-365.
- Logan CY, Nusse R: **The Wnt signaling pathway in development and disease.** *Annu Rev Cell Dev Biol* 2004, **20**:781-810.

- Lu JM, Ma ZQ, Hsieh JC, Fan CW, Chen BZ, Longgood JC, Williams NS, Amatruda JF, Lum L, Chen C: **Structure-activity relationship studies of small-molecule inhibitors of Wnt response.** *Bioorg Med Chem Lett* 2009, **19**(14):3825-3827.
- Machan R, Hof M: **Recent Developments in Fluorescence Correlation Spectroscopy for Diffusion Measurements in Planar Lipid Membranes.** *International Journal of Molecular Sciences* 2010, **11**(2):427-457.
- Magde D, Webb WW, Elson E: **Thermodynamic Fluctuations in a Reacting System - Measurement by Fluorescence Correlation Spectroscopy.** *Phys Rev Lett* 1972, **29**(11):705-708.
- Magde D, Elson EL, Webb WW: **Fluorescence correlation spectroscopy. II. An experimental realization.** *Biopolymers* 1974, **13**(1):29-61.
- Magde D, Webb WW, Elson EL: **Fluorescence correlation spectroscopy. III. Uniform translation and laminar flow.** *Biopolymers* 1978, **17**(2):361-376.
- Malchus N, Weiss M: **Elucidating Anomalous Protein Diffusion in Living Cells with Fluorescence Correlation Spectroscopy-Facts and Pitfalls.** *J Fluoresc* 2010, **20**(1):19-26.
- Marois E, Mahmoud A, Eaton S: **The endocytic pathway and formation of the Wingless morphogen gradient.** *Development* 2006, **133**(2):307-317.
- McHale K, Berglund AJ, Mabuchi H: **Bayesian estimation for species identification in single-molecule fluorescence microscopy.** *Biophys J* 2004, **86**(6):3409-3422.
- Meacci G, Ries J, Fischer-Friedrich E, Kahya N, Schwille P, Kruse K: **Mobility of Min-proteins in Escherichia coli measured by fluorescence correlation spectroscopy.** *Phys Biol* 2006, **3**(4):255-263.
- Mellman I: **Endocytosis and molecular sorting.** *Annu Rev Cell Dev Biol* 1996, **12**:575-625.
- Meseth U, Wohland T, Rigler R, Vogel H: **Resolution of fluorescence correlation measurements.** *Biophys J* 1999, **76**(3):1619-1631.
- Mii Y, Taira M: **Secreted Frizzled-related proteins enhance the diffusion of Wnt ligands and expand their signalling range.** *Development* 2009, **136**(24):4083-4088.
- Mikels AJ, Nusse R: **Purified Wnt5a protein activates or inhibits beta-catenin-TCF signaling depending on receptor context.** *PLoS Biol* 2006, **4**(4):570-582.
- Miller JR: **The Wnts.** *Genome Biol* 2002, **3**(1):reviews3001.3001-3001.3015.
- Milon S, Hovius R, Vogel H, Wohland T: **Factors influencing fluorescence correlation spectroscopy measurements on membranes: simulations and experiments.** *Chem Phys* 2003, **288**(2-3):171-186.
- Miyawaki A: **Proteins on the move: insights gained from fluorescent protein technologies.** *Nature Reviews Molecular Cell Biology* 2011, **12**(10):656-668.
- Molven A, Njåstad P, Fjose A: **Genomic structure and restricted neural expression of the zebrafish wnt-1 (int-1) gene.** *The EMBO journal* 1991, **10**(4):799.
- Monnier N, Guo S-M, Mori M, He J, Lénárt P, Bathe M: **Bayesian approach to MSD-based analysis of particle motion in live cells.** *Biophys J* 2012, **103**(3):616-626.
- Müller CB, Loman A, Pacheco V, Koberling F, Willbold D, Richtering W, Enderlein J: **Precise measurement of diffusion by multi-color dual-focus fluorescence correlation spectroscopy.** *Epl* 2008, **83**(4).
- Mulligan KA, Fuerer C, Ching W, Fish M, Willert K, Nusse R: **Secreted Wingless-interacting molecule (Swim) promotes long-range signaling by maintaining Wingless solubility.** *Proc Natl Acad Sci U S A* 2012, **109**(2):370-377.
- Mütze J, Ohrt T, Schwille P: **Fluorescence correlation spectroscopy in vivo.** *Laser Photonics Rev* 2011, **5**(1):52-67.

- Nagai T, Ibata K, Park ES, Kubota M, Mikoshiba K, Miyawaki A: **A variant of yellow fluorescent protein with fast and efficient maturation for cell-biological applications.** *Nat Biotechnol* 2002, **20**(1):87-90.
- Nagy A, Wu JR, Berland KM: **Characterizing observation volumes and the role of excitation saturation in one-photon fluorescence fluctuation spectroscopy.** *J Biomed Opt* 2005, **10**(4).
- Nakashima N, Liu D, Huang CL, Ueno M, Zhang X, Yokomise H: **Wnt3 gene expression promotes tumor progression in non-small cell lung cancer.** *Lung Cancer* 2012, **76**(2):228-234.
- Nambotin SB, Tomimaru Y, Merle P, Wands JR, Kim M: **Functional consequences of WNT3/Frizzled7-mediated signaling in non-transformed hepatic cells.** *Oncogenesis* 2012, **1**(e31):1-9.
- Needleman DJ, Xu YQ, Mitchison TJ: **Pin-Hole Array Correlation Imaging: Highly Parallel Fluorescence Correlation Spectroscopy.** *Biophys J* 2009, **96**(12):5050-5059.
- Neumann CJ, Cohen SM: **Long-range action of Wingless organizes the dorsal-ventral axis of the Drosophila wing.** *Development* 1997, **124**(4):871-880.
- Neumann S, Coudreuse DYM, van der Westhuyzen DR, Eckhardt ERM, Korswagen HC, Schmitz G, Sprong H: **Mammalian Wnt3a is Released on Lipoprotein Particles.** *Traffic* 2009, **10**(3):334-343.
- Niemann S, Zhao CF, Pascu F, Stahl U, Aulepp U, Niswander L, Weber JL, Muller U: **Homozygous WNT3 mutation causes tetra-amelia in a large consanguineous family.** *Am J Hum Genet* 2004, **74**(3):558-563.
- Nusse R, Varmus HE: **Many tumors induced by the mouse mammary tumor virus contain a provirus integrated in the same region of the host genome.** *Cell* 1982, **31**(1):99-109.
- Ohr T, Muetze J, Staroske W, Weinmann L, Hock J, Crell K, Meister G, Schwille P: **Fluorescence correlation spectroscopy and fluorescence cross-correlation spectroscopy reveal the cytoplasmic origination of loaded nuclear RISC in vivo in human cells.** *Nucleic Acids Res* 2008, **36**(20):6439-6449.
- Ormo M, Cubitt AB, Kallio K, Gross LA, Tsien RY, Remington SJ: **Crystal structure of the Aequorea victoria green fluorescent protein.** *Science* 1996, **273**(5280):1392-1395.
- Pan CL, Baum PD, Gu MY, Jorgensen EM, Clark SG, Garriga G: **C-elegans AP-2 and retromer control Wnt signaling by regulating MIG-14/Wntless.** *Dev Cell* 2008, **14**(1):132-139.
- Pan X, Aw C, Du Y, Yu H, Wohland T: **Characterization of poly(acrylic acid) diffusion dynamics on the grafted surface of poly(ethylene terephthalate) films by fluorescence correlation spectroscopy.** *Biophysical Reviews and Letters* 2006, **1**(4):1-9.
- Pan XT, Foo W, Lim W, Fok MHY, Liu P, Yu H, Maruyama I, Wohland T: **Multifunctional fluorescence correlation microscope for intracellular and microfluidic measurements.** *Rev Sci Instrum* 2007, **78**(5).
- Pan ákov áD, Sprong H, Marois E, Thiele C, Eaton S: **Lipoprotein particles are required for Hedgehog and Wingless signalling.** *Nature* 2005, **435**(7038):58-65.
- Pauls S, Geldmacher-Voss B, Campos-Ortega JA: **A zebrafish histone variant H2A.F/Z and a transgenic H2A.F/Z : GFP fusion protein for in vivo studies of embryonic development.** *Development Genes and Evolution* 2001, **211**(12):603-610.

- Pei YX, Brun SN, Markant SL, Lento W, Gibson P, Taketo MM, Giovannini M, Gilbertson RJ, Wechsler-Reya RJ: **WNT signaling increases proliferation and impairs differentiation of stem cells in the developing cerebellum.** *Development* 2012, **139**(10):1724-1733.
- Petrasek Z, Hoegge C, Mashaghi A, Ohrt T, Hyman AA, Schwille P: **Characterization of Protein Dynamics in Asymmetric Cell Division by Scanning Fluorescence Correlation Spectroscopy.** *Biophys J* 2008, **95**(11):5476-5486.
- Pfeiffer S, Ricardo S, Manneville JB, Alexandre C, Vincent JP: **Producing cells retain and recycle wingless in Drosophila embryos.** *Curr Biol* 2002, **12**(11):957-962.
- Piddini E, Marshall F, Dubois L, Hirst E, Vincent JP: **Arrow (LRP6) and Frizzled2 cooperate to degrade Wingless in Drosophila imaginal discs.** *Development* 2005, **132**(24):5479-5489.
- Pitschke M, Prior R, Haupt M, Riesner D: **Detection of single amyloid beta-protein aggregates in the cerebrospinal fluid of Alzheimer's patients by fluorescence correlation spectroscopy.** *Nat Med* 1998, **4**(7):832-834.
- Port F, Basler K: **Wnt Trafficking: New Insights into Wnt Maturation, Secretion and Spreading.** *Traffic* 2010, **11**(10):1265-1271.
- Posada D, Buckley TR: **Model selection and model averaging in phylogenetics: Advantages of akaike information criterion and Bayesian approaches over likelihood ratio tests.** *Syst Biol* 2004, **53**(5):793-808.
- Prasad BC, Clark SG: **Wnt signaling establishes anteroposterior neuronal polarity and requires retromer in C-elegans.** *Development* 2006, **133**(9):1757-1766.
- Proffitt KD, Madan B, Ke ZY, Pendharkar V, Ding LJ, Lee MA, Hannoush RN, Virshup DM: **Pharmacological Inhibition of the Wnt Acyltransferase PORCN Prevents Growth of WNT-Driven Mammary Cancer.** *Cancer Res* 2013, **73**(2):502-507.
- Qian H, Elson EL: **On the analysis of high order moments of fluorescence fluctuations.** *Biophys J* 1990, **57**(2):375-380.
- Raftery AE: **Bayesian model selection in social research.** In: *Soc Method. Volume 25*, edn. Edited by Marsden PV. Malden: Blackwell Publ; 1995: 111-163.
- Ramírez-Weber F-A, Kornberg TB: **Cytosomes: cellular processes that project to the principal signaling center in Drosophila imaginal discs.** *Cell* 1999, **97**(5):599-607.
- Reya T, Clevers H: **Wnt signalling in stem cells and cancer.** *Nature* 2005, **434**(7035):843-850.
- Ries J, Schwille P: **New concepts for fluorescence correlation spectroscopy on membranes.** *PCCP* 2008, **10**(24):3487-3497.
- Ries J, Yu SR, Burkhardt M, Brand M, Schwille P: **Modular scanning FCS quantifies receptor-ligand interactions in living multicellular organisms.** *Nat Methods* 2009, **6**(9):643-U631.
- Ries J, Schwille P: **Fluorescence correlation spectroscopy.** *Bioessays* 2012, **34**(5):361-368.
- Rigler R, Mets U, Widengren J, Kask P: **Fluorescence correlation spectroscopy with high count rate and low background: analysis of translational diffusion.** *European Biophysics Journal with Biophysics Letters* 1993, **22**(3):169-175.
- Rives AF, Rochlin KM, Wehrli M, Schwartz SL, DiNardo S: **Endocytic trafficking of Wingless and its receptors, Arrow and DFrizzled-2, in the Drosophila wing.** *Dev Biol* 2006, **293**(1):268-283.
- Robertson CP, Braun MM, Roelink H: **Sonic hedgehog patterning in chick neural plate is antagonized by a Wnt3-like signal.** *Dev Dyn* 2004, **229**(3):510-519.

- Roy S, Hsiung F, Kornberg TB: **Specificity of Drosophila Cytonemes for Distinct Signaling Pathways.** *Science* 2011, **332**(6027):354-358.
- Roy S, Huang H, Liu S, Kornberg TB: **Cytoneme-mediated contact-dependent transport of the Drosophila decapentaplegic signaling protein.** *Science* 2014, **343**(6173):1244624.
- Saffarian S, Elson EL: **Statistical analysis of fluorescence correlation spectroscopy: The standard deviation and bias.** *Biophys J* 2003, **84**(3):2030-2042.
- Salinas PC, Nusse R: **Regional expression of the Wnt-3 gene in the developing mouse forebrain in relationship to diencephalic neuromeres.** *Mech Dev* 1992, **39**(3):151-160.
- Sanders TA, Llagostera E, Barna M: **Specialized filopodia direct long-range transport of SHH during vertebrate tissue patterning.** *Nature* 2013, **497**(7451):628-632.
- Sato M, Kornberg TB: **FGF is an essential mitogen and chemoattractant for the air sacs of the Drosophila tracheal system.** *Dev Cell* 2002, **3**(2):195-207.
- Saxton MJ: **A biological interpretation of transient anomalous subdiffusion. I. Qualitative model.** *Biophys J* 2007, **92**(4):1178-1191.
- Schäzel K, Peters R: **Noise on Multiple-Tau Photon Correlation Data.** *SPIE—International Society for Optical Engineering: Bellingham, WA*, 1991.
- Schenk A, Ivanchenko S, Rucker C, Wiedenmann JR, Nienhaus GU: **Photodynamics of red fluorescent proteins studied by fluorescence correlation spectroscopy.** *Biophys J* 2004, **86**(1):384-394.
- Schneider A, Simons M: **Exosomes: vesicular carriers for intercellular communication in neurodegenerative disorders.** *Cell Tissue Res* 2013, **352**(1):33-47.
- Schwille P, MeyerAlmes FJ, Rigler R: **Dual-color fluorescence cross-correlation spectroscopy for multicomponent diffusional analysis in solution.** *Biophys J* 1997, **72**(4):1878-1886.
- Schwille P, Korlach J, Webb WW: **Fluorescence correlation spectroscopy with single-molecule sensitivity on cell and model membranes.** *Cytometry* 1999, **36**(3):176-182.
- Schwille P, Kummer S, Heikal AA, Moerner WE, Webb WW: **Fluorescence correlation spectroscopy reveals fast optical excitation-driven intramolecular dynamics of yellow fluorescent proteins.** *Proc Natl Acad Sci U S A* 2000, **97**(1):151-156.
- Schwille P: **Fluorescence correlation spectroscopy and its potential for intracellular applications.** *Cell Biochem Biophys* 2001, **34**(3):383-408.
- Seber GAF, Wild CJ: **Nonlinear Regression.** *Wiley: New York* 1989.
- Shaner NC, Campbell RE, Steinbach PA, Giepmans BNG, Palmer AE, Tsien RY: **Improved monomeric red, orange and yellow fluorescent proteins derived from Discosoma sp red fluorescent protein.** *Nat Biotechnol* 2004, **22**(12):1567-1572.
- Shaner NC, Steinbach PA, Tsien RY: **A guide to choosing fluorescent proteins.** *Nat Methods* 2005, **2**(12):905-909.
- Shcherbo D, Murphy CS, Ermakova GV, Solovieva EA, Chepurnykh TV, Shcheglov AS, Verkhusha VV, Pletnev VZ, Hazelwood KL, Roche PM *et al*: **Far-red fluorescent tags for protein imaging in living tissues.** *Biochem J* 2009, **418**:567-574.
- Shi X, Wohland T: **Fluorescence correlation spectroscopy.** *Nanoscopy and Multidimensional Optical Fluorescence Microscopy, A Diaspro, Editor* 2009:Taylor & Francis: Boca Raton.
- Shi XK, Foo YH, Sudhaharan T, Chong SW, Korzh V, Ahmed S, Wohland T: **Determination of Dissociation Constants in Living Zebrafish Embryos with**

- Single Wavelength Fluorescence Cross-Correlation Spectroscopy.** *Biophys J* 2009, **97**(2):678-686.
- Shi XK, Teo LS, Pan XT, Chong SW, Kraut R, Korzh V, Wohland T: **Probing Events with Single Molecule Sensitivity in Zebrafish and Drosophila Embryos by Fluorescence Correlation Spectroscopy.** *Dev Dyn* 2009, **238**(12):3156-3167.
- Shimomura O, Johnson FH, Saiga Y: **Extraction, purification and properties of Aequorin, a bioluminescent protein from the luminous hydromedusa, Aequorea.** *J Cell Comp Physiol* 1962, **59**(3):223-&.
- Simons M, Raposo G: **Exosomes - vesicular carriers for intercellular communication.** *Curr Opin Cell Biol* 2009, **21**(4):575-581.
- Sisan DR, Arevalo R, Graves C, McAllister R, Urbach JS: **Spatially resolved fluorescence correlation spectroscopy using a spinning disk confocal microscope.** *Biophys J* 2006, **91**(11):4241-4252.
- Sivia DS, Skilling J: **Data Analysis: A Bayesian Tutorial**, 2nd edn. Oxford, U.K.: Oxford University Press; 2006.
- Stanganello E, Hagemann AI, Mattes B, Sinner C, Meyen D, Weber S, Schug A, Raz E, Scholpp S: **Filopodia-based Wnt transport during vertebrate tissue patterning.** *Nature communications* 2015, **6**.
- Starchev K, Ricka J, Buffle J: **Noise on fluorescence correlation spectroscopy.** *J Colloid Interface Sci* 2001, **233**(1):50-55.
- Steinman RM, Mellman IS, Muller WA, Cohn ZA: **Endocytosis and the Recycling of Plasma Membrane** *J Cell Biol* 1983, **96**(1):1-27.
- Stewart S, Gomez AW, Armstrong BE, Henner A, Stankunas K: **Sequential and Opposing Activities of Wnt and BMP Coordinate Zebrafish Bone Regeneration.** *Cell Reports* 2014, **6**(3):482-498.
- Strigini M, Cohen SM: **Wingless gradient formation in the Drosophila wing.** *Curr Biol* 2000, **10**(6):293-300.
- Takada R, Satomi Y, Kurata T, Ueno N, Norioka S, Kondoh H, Takao T, Takada S: **Monounsaturated fatty acid modification of Wnt protein: Its role in Wnt secretion.** *Dev Cell* 2006, **11**(6):791-801.
- Takahashi Y, Okamoto Y, Popiel HA, Fujikake N, Toda T, Kinjo M, Nagai Y: **Detection of polyglutamine protein oligomers in cells by fluorescence correlation spectroscopy.** *J Biol Chem* 2007, **282**(33):24039-24048.
- Tanaka K, Okabayashi K, Asashima M, Perrimon N, Kadowaki T: **The evolutionarily conserved porcupine gene family is involved in the processing of the Wnt family.** *Eur J Biochem* 2000, **267**(13):4300-4311.
- Tang XF, Wu YH, Belenkaya TY, Huang QZ, Ray L, Qu J, Lin XH: **Roles of N-glycosylation and lipidation in Wg secretion and signaling.** *Dev Biol* 2012, **364**(1):32-41.
- Tcherniak A, Reznik C, Link S, Landes CF: **Fluorescence Correlation Spectroscopy: Criteria for Analysis in Complex Systems.** *Anal Chem* 2009, **81**(2):746-754.
- Terada S, Kinjo M, Hirokawa N: **Oligomeric tubulin in large transporting complex is transported via kinesin in squid giant axone.** *Cell* 2000, **103**(1):141-155.
- Thompson N: **Fluorescence correlation spectroscopy.** In: *Lakowicz, JR, ed, Topics in Fluorescence Spectroscopy New York: Plenum Press* 1991, **1**(Techniques):337-378.
- van den Heuvel M, Harryman-Samos C, Klingensmith J, Perrimon N, Nusse R: **Mutations in the segment polarity genes wingless and porcupine impair secretion of the wingless protein.** *EMBO J* 1993, **12**(13):5293-5302.

- van der Horst DJ, van Hoof D, van Marrewijk WJA, Rodenburg KW: **Alternative lipid mobilization: The insect shuttle system.** *Mol Cell Biochem* 2002, **239**(1-2):113-119.
- Verveer PJ, Swoger J, Pampaloni F, Greger K, Marcello M, Stelzer EHK: **High-resolution three-dimensional imaging of large specimens with light sheet-based microscopy.** *Nat Methods* 2007, **4**(4):311-313.
- Vyas N, Goswami D, Manonmani A, Sharma P, Ranganath HA, VijayRaghavan K, Shashidhara LS, Sowdhamini R, Mayor S: **Nanoscale organization of Hedgehog is essential for long-range signaling.** *Cell* 2008, **133**(7):1214-1227.
- Wachsmuth M, Waldeck W, Langowski J: **Anomalous diffusion of fluorescent probes inside living cell nuclei investigated by spatially-resolved fluorescence correlation spectroscopy.** *J Mol Biol* 2000, **298**(4):677-689.
- Wang SX, Hazelrigg T: **Implications for bcd mRNA localization from spatial distribution of exu protein in Drosophila oogenesis.** *Nature* 1994, **369**(6479):400-403.
- Wend P, Runke S, Wend K, Anchondo B, Yesayan M, Jardon M, Hardie N, Loddenkemper C, Ulasov I, Lesniak MS *et al*: **WNT10B/-catenin signalling induces HMGA2 and proliferation in metastatic triple-negative breast cancer.** *EMBO Mol Med* 2013, **5**(2):264-279.
- Widengren J, Rigler R, Mets Ü: **Triplet-State Monitoring by Fluorescence Correlation Spectroscopy.** *J Fluoresc* 1994, **4**(3):255-258.
- Widengren J, Mets U, Rigler R: **Fluorescence correlation spectroscopy of triplet states in solution: a theoretical and experimental study.** *J Phys Chem* 1995, **99**(36):13368-13379.
- Widengren J, Mets U, Rigler R: **Photodynamic properties of green fluorescent proteins investigated by fluorescence correlation spectroscopy.** *Chem Phys* 1999, **250**(2):171-186.
- Widengren J, Terry B, Rigler R: **Protonation kinetics of GFP and FITC investigated by FCS - aspects of the use of fluorescent indicators for measuring pH.** *Chem Phys* 1999, **249**(2-3):259-271.
- Widengren J, Schwille P: **Characterization of photoinduced isomerization and back-isomerization of the cyanine dye Cy5 by fluorescence correlation spectroscopy.** *J Phys Chem A* 2000, **104**(27):6416-6428.
- Widengren J, Seidel CAM: **Manipulation and characterization of photo-induced transient states of Merocyanine 540 by fluorescence correlation spectroscopy.** *PCCP* 2000, **2**(15):3435-3441.
- Willems E, Spiering S, Davidovics H, Lanier M, Xia ZB, Dawson M, Cashman J, Mercola M: **Small-Molecule Inhibitors of the Wnt Pathway Potently Promote Cardiomyocytes From Human Embryonic Stem Cell-Derived Mesoderm.** *Circul Res* 2011, **109**(4):360-U338.
- Willert K, Brown JD, Danenberg E, Duncan AW, Weissman IL, Reya T, Yates JR, Nusse R: **Wnt proteins are lipid-modified and can act as stem cell growth factors.** *Nature* 2003, **423**(6938):448-452.
- Wohland T, Rigler R, Vogel H: **The standard deviation in fluorescence correlation spectroscopy.** *Biophys J* 2001, **80**(6):2987-2999.
- Wohland T, Shi XK, Sankaran J, Stelzer EHK: **Single Plane Illumination Fluorescence Correlation Spectroscopy (SPIM-FCS) probes inhomogeneous three-dimensional environments.** *Opt Express* 2010, **18**(10):10627-10641.
- Wu B, Chen Y, Muller JD: **Fluorescence Fluctuation Spectroscopy of mCherry in Living Cells.** *Biophys J* 2009, **96**(6):2391-2404.

- Wu CH, Nusse R: **Ligand receptor interactions in the Wnt signaling pathway in *Drosophila*.** *J Biol Chem* 2002, **277**(44):41762-41769.
- Yan D, Lin XH: **Shaping Morphogen Gradients by Proteoglycans.** *Cold Spring Harb Perspect Biol* 2009, **1**(3).
- Yan D, Wu YH, Feng Y, Lin SC, Lin XH: **The Core Protein of Glypican Daily-Like Determines Its Biphasic Activity in Wingless Morphogen Signaling.** *Dev Cell* 2009, **17**(4):470-481.
- Yang PT, Lorenowicz MJ, Silhankova M, Coudreuse DYM, Betist MC, Korswagen HC: **Wnt signaling requires retromer-dependent recycling of MIG-14/Wntless in Wnt-producing cells.** *Dev Cell* 2008, **14**(1):140-147.
- Yao J, Munson KM, Webb WW, Lis JT: **Dynamics of heat shock factor association with native gene loci in living cells.** *Nature* 2006, **442**(7106):1050-1053.
- Yu SR, Burkhardt M, Nowak M, Ries J, Petrasek Z, Scholpp S, Schwille P, Brand M: **Fgf8 morphogen gradient forms by a source-sink mechanism with freely diffusing molecules.** *Nature* 2009, **461**(7263):533-U100.
- Zecca M, Basler K, Struhl G: **Direct and long-range action of a wingless morphogen gradient.** *Cell* 1996, **87**(5):833-844.
- Zhai L, Chaturvedi D, Cumberledge S: ***Drosophila* Wnt-1 undergoes a hydrophobic modification and is targeted to lipid rafts, a process that requires porcupine.** *J Biol Chem* 2004, **279**(32):33220-33227.
- Zhao M, Jin L, Chen B, Ding Y, Ma H, Chen DY: **Afterpulsing and its correction in fluorescence correlation spectroscopy experiments.** *Appl Opt* 2003, **42**(19):4031-4036.
- Zhou SH, Lo WC, Suhalim JL, Digman MA, Gratton E, Nie Q, Lander AD: **Free Extracellular Diffusion Creates the Dpp Morphogen Gradient of the *Drosophila* Wing Disc.** *Curr Biol* 2012, **22**(8):668-675.

Appendices

JOHN WILEY AND SONS LICENSE TERMS AND CONDITIONS

Mar 25, 2015

This Agreement between Guangyu SUN ("You") and John Wiley and Sons ("John Wiley and Sons") consists of your license details and the terms and conditions provided by John Wiley and Sons and Copyright Clearance Center.

License Number	3595101391982
License date	Mar 23, 2015
Licensed Content Publisher	John Wiley and Sons
Licensed Content Publication	Traffic
Licensed Content Title	Wnt Trafficking: New Insights into Wnt Maturation, Secretion and Spreading
Licensed Content Author	Fillip Port,Konrad Basler
Licensed Content Date	May 3, 2010
Pages	7
Type of use	Dissertation/Thesis
Requestor type	University/Academic
Format	Print and electronic
Portion	Figure/table
Number of figures/tables	1
Original Wiley figure/table number(s)	Figure 1
Will you be translating?	No
Title of your thesis / dissertation	Application of Bayesian Model Selection in Fluorescence Correlation Spectroscopy (FCS) to Wnt3EGFP Secretion and Diffusion in Zebrafish Embryos
Expected completion date	Mar 2015
Expected size (number of pages)	160
Requestor Location	Guangyu SUN Blk S1A, Level 2, DBS, NUS Singapore, Singapore 117557 Attn: Guangyu SUN
Billing Type	Invoice
Billing Address	Guangyu SUN Blk S1A, Level 2, DBS, NUS Singapore, Singapore 117557 Attn: Guangyu SUN
Total	0.00 USD

**AMERICAN ASSOCIATION FOR CANCER RESEARCH LICENSE
TERMS AND CONDITIONS**

Mar 25, 2015

This is a License Agreement between Guangyu SUN ("You") and American Association for Cancer Research ("American Association for Cancer Research") provided by Copyright Clearance Center ("CCC"). The license consists of your order details, the terms and conditions provided by American Association for Cancer Research, and the payment terms and conditions.

All payments must be made in full to CCC. For payment instructions, please see information listed at the bottom of this form.

License Number	3595110170594
License date	Mar 23, 2015
Licensed content publisher	American Association for Cancer Research
Licensed content publication	Clinical Cancer Research
Licensed content title	WNT Signaling Pathway and Stem Cell Signaling Network
Licensed content author	Masuko Katoh, Masaru Katoh
Licensed content date	July 15, 2007
Volume number	13
Issue number	14
Type of Use	Thesis/Dissertation
Requestor type	academic/educational
Format	print and electronic
Portion	figures/tables/illustrations
Number of figures/tables /illustrations	1
Will you be translating?	no
Circulation	5
Territory of distribution	Worldwide
Title of your thesis / dissertation	Application of Bayesian Model Selection in Fluorescence Correlation Spectroscopy (FCS) to Wnt3EGFP Secretion and Diffusion in Zebrafish Embryos
Expected completion date	Mar 2015
Estimated size (number of pages)	160
Total	0.00 USD